Τμήμα Ιατρικής, Πανεπιστήμιο Κρήτης

Δ/ντής Καθηγητής: Ιωάννης Δαμηλάκης

Συγγραφέας: *Αγγελική Ντούλη*

Επιβλέποντες: *Θωμάς Μαρής*

Μιχάλης Μαζωνάκης

Συγκριτική μελέτη διαφορετικών υλικών σε εφαρμογές δοσιμετρίας γέλης πολυμερισμού: Βέλτιστη ευαισθησία σε μετρήσεις δόσης ακτινοβολίας

Μια διπλωματική εργασία για την κατάκτηση του Μεταπτυχιακού Διπλώματος Ειδίκευσης (ΜΔΕ) στην Ιατρική Φυσική – Ακτινοφυσική σε συνεργασία με το:

Τμήμα Φυσικής και το Τμήμα Ιατρικής, του Εθνικού και Καποδιστριακού Πανεπιστημίου Αθηνών
Τμήμα Μαγνητικού Τομογράφου και τμήμα Ακτινοθεραπείας, του Πανεπιστημιακού Νοσοκομείου Ηρακλείου ΠΑΓΝΗ
Εργαστήριο Ιατρικής Φυσικής, της Ιατρικής Σχολής Ηρακλείου

Ηράκλειο 2020

Medical School, University of Crete

Head of Department: Prof. Ioannis Damilakis

Author: *Aggeliki Ntouli*

Supervisors: *Prof. Thomas Maris*

Prof. Michalis Mazonakis

Comparative study of different materials in gel dosimetry applications: Optimal sensitivity in radiation dose measurements

A thesis submitted for the Postgraduate Specialization Diploma in Medical Physics – Radiophysics in collaboration with the:

Department of Physics and Medicine, of National and Kapodistrian University of Athens
Magnetic Resonance Imaging (MRI) and Radiation Therapy Departments, of Heraklion University Hospital PAGNI
Medical Physics Laboratory, of Heraklion Medical School

Heraklion 2020

Acknowledgements

Undertaking this MSc program would not have been possible to do without the support and guidance that I received from many people.

Firstly, I would like to thank my supervisor Professor Michalis Mazonakis for his guidance and kind advice for my MSc research studies. Thank you for your interest in improving my work with your insights.

In particular, I also thank my supervisor Professor Thomas G. Maris. His ability to share his enthusiasm and deep knowledge on all aspects of physics and especially in MR Imaging encouraged me to continue working. I really appreciate all the discussions we held, with a background sound of MR sequences.

Moreover, I appreciate the trust of the Professor and Chairman of the Medical Physics Department of University of Crete, Mr. Ioannis Damilakis, has shown during my thesis.

I am grateful to have shared time with Themis Boursianis in the lab. He has been very patient explaining to me the fundamental chemical and physical phenomena that occur in polymer gel dosimeters used for detection and verification of dose distributions used in cancer radiotherapy, as well as their manufacture in the lab. I also want to thank George Kalaitzakis, for his support and his interest on improving my work with his insights. They both have been very generous to me and I thank them for provoking my interest in their fields of expertise.

Away from work, I thank my friends who supported me and were by my side throughout the completion of my thesis and my stay in Heraklion.

Last but not least, I would like to thank my family for always inspiring me and for their never-ending love and support.

Abstract

Magnetic resonance imaging (MRI) is a method based on the phenomenon of nuclear magnetic resonance (NMR) and its optimization is achieved by combining settings of many parameters. Especially in quantitative MRI, where magnetic relaxation times (T1, T2) and other physical properties are measured, the parameters of the imaging system play a very important role in the results of the measurements. Thus, it is considered necessary to use phantoms in order to calibrate the unit system and evaluate the measurement methods.

These phantoms should simulate the relaxation times, but also the physical properties of the biological tissues. In addition, they must be physically and chemically stable over time and easy to manufacture. These phantoms are made of radiation-sensitive chemicals which, upon irradiation, polymerize as a function of the absorbed radiation dose, with the ability to uniquely record the radiation dose distribution in three dimensions (3D).

Dosimetry has been a main factor for the development of radiotherapy techniques and there are already various dosimetric systems and methods for estimating the dose administered to tissues and other means. Polymer gel dosimeters offer a wide range of potential applications in the three-dimensional verification of complex dose distribution such as in intensity modulated radiotherapy (IMRT). Today, complex algorithms are used to determine the dose distributions required in a treatment plan, and of course the rapid development of technology enables the development of modern radiotherapy techniques.

In the context of this work, two different polymer gel dosimeters (VIPET and VIPASCU) were compared, in terms of their basic properties in MRI. These dosimeters were studied, at various concentrations, to investigate the effect, of the changes in the concentration of specific monomers, on the magnetic recovery times T1 and T2.

The main goal was to manufacture a new polymerization gel dosimeter which is less toxic, economical but at the same time easy to make and efficient with high dose sensitivity. It was also important to optimize the quality of the results from the radiotherapy experiments performed, with the parallel support of magnetic resonance imaging techniques.

Finally, we additionally compared the two methods which was used to measure magnetic relaxation times, as the first, *Multi Spin Echo*, is widely used in clinical practice, while *HASTE* is not.

Σύνοψη

Η απεικόνιση μαγνητικού συντονισμού (ΑΜΣ) είναι μέθοδος που βασίζεται στο φαινόμενο του πυρηνικού μαγνητικού συντονισμού (ΠΜΣ) και η βελτιστοποίησή της επιτυγχάνεται με το συνδυασμό ρυθμίσεων πολλών παραμέτρων. Ειδικά στην ποσοτική MRI, όπου μετρούμε χρόνους μαγνητικής αποκατάστασης και άλλες φυσικές ιδιότητες, οι ρυθμίσεις των παραμέτρων του συστήματος απεικόνισης παίζουν σημαντικότατο ρόλο στα αποτελέσματα των μετρήσεων. Έτσι κρίνεται απαραίτητη η χρήση ομοιωμάτων για τη βαθμονόμηση των συστημάτων και την αξιολόγηση των μεθόδων μέτρησης.

Τα εν λόγω ομοιώματα θα πρέπει να προσομοιάζουν τους χρόνους αποκατάστασης, αλλά και φυσικές ιδιότητες των βιολογικών ιστών. Επιπλέον θα πρέπει να είναι φυσικά και χημικά σταθερά στο χρόνο και εύκολα στην κατασκευή τους. Τα ομοιώματα αυτά κατασκευάζονται από χημικά ευαίσθητα στην ακτινοβολία τα οποία, κατά την ακτινοβόληση, πολυμερίζονται ως συνάρτηση της απορροφούμενης δόσης ακτινοβολίας, με την ικανότητα να καταγράφουν μοναδικά την κατανομή της δόσης ακτινοβολίας σε τρεις διαστάσεις (3D).

Η δοσιμετρία έχει αποτελέσει το κέντρο για την ανάπτυξη των τεχνικών ακτινοθεραπείας και ήδη υπάρχουν διάφορα δοσιμετρικά συστήματα και μέθοδοι για την εκτίμηση της χορηγούμενης δόσης στους ιστούς και σε άλλα μέσα. Τα δοσίμετρα γέλης πολυμερισμού προσφέρουν ένα ευρύ φάσμα πιθανών εφαρμογών στην τρισδιάστατη επαλήθευση της σύνθετης κατανομής δόσεων, όπως στην ακτινοθεραπεία διαμορφούμενης έντασης της δέσμης (IMRT). Σήμερα, χρησιμοποιούνται πολύπλοκοι αλγόριθμοι για τον προσδιορισμό των κατανομών δόσης που απαιτούνται σε ένα πλάνο θεραπείας και φυσικά η ραγδαία εξέλιξη της τεχνολογίας, δίνει τη δυνατότητα ανάπτυξης υπερσύγχρονων τεχνικών ακτινοθεραπείας.

Στα πλαίσια της εργασίας αυτής, έγινε σύγκριση δύο διαφορετικών δοσιμέτρων γέλης πολυμερισμού (*VIPET* και *VIPASCU*), ως προς τις βασικές τους ιδιότητες στην ΑΜΣ. Μελετήθηκαν τα δοσίμετρα αυτά, σε διάφορες συγκεντρώσεις, για να διερευνηθεί η επίδραση των μεταβολών της συγκέντρωσης τους στους χρόνους μαγνητικής αποκατάστασης T1 και T2.

Βασικός στόχος ήταν η κατασκευή ενός νέου δοσιμέτρου γέλης πολυμερισμού το οποία είναι λιγότερο τοξικό, οικονομικό αλλά παράλληλα εύκολο στην κατασκευή και αποδοτικό με υψηλή ευαισθησία στη δόση. Σημαντική ήταν επίσης η βελτιστοποίηση της ποιότητας των αποτελεσμάτων από τα πειράματα ακτινοθεραπείας που πραγματοποιήθηκαν, με την παράλληλη υποστήριξη τεχνικών μαγνητικής τομογραφίας σε ομοιώματα. Επίσης, η διασφάλιση της ποιότητας των δοσιμετρικών αποτελεσμάτων, από τα πειράματα ακτινοθεραπείας που πραγματοποιήθηκαν.

Τέλος, συμπληρωματικά συγκρίναμε και τις δύο μεθόδους που χρησιμοποιήσαμε για την μέτρηση των χρόνων μαγνητικής αποκατάστασης, καθώς η πρώτη, *Spin Echo (SE)* ακολουθία, χρησιμοποιείται κατά κόρον στην κλινική πράξη, ενώ η ακολουθία *HASTE* όχι.

Table of Contents

Acronyms

ADC: Apparent Diffusion Coefficient

BIS: Bisacrylamide Crosslinker

BR: Background Magnetic Field

CI: Confidence Interval

CP: Carr Purcell technique

CPMG: Carr -Purcell- Meiboom- Gill technique

CRT: Conformal Radiation Therapy

EBRT: External Beam Radiation therapy

EMR: Electromagnetic Radiation

EMS: Electromagnetic Spectrum

FT: Fourier Transform

FOV: Field Of View

GE: Gradient Echo

GFE or G_F : Frequency Encoding Gradient

GPE or G_P : Phase Encoding Gradient

GSS or G_S : Slice Selection Gradient

HASTE: Half Fourier Acquisition Single Shot TSE

IGRT: Image Guided Radiotherapy

IMRT: Intensity Modulated Radiotherapy

LINAC: Linear Accelerator

LoA: Limit of Agreement

MEGRE: Multi Echo Gradient Echo

MESE: Multi Echo Spin Echo

MLC: Multileaf Collimator

NMR: Nuclear Magnetic Resonance

MRI: Magnetic Resonance Imaging

MU: Monitor Units

PE: Phase Encoding

PHAPS: Alternating Phase-Shift

R1: MRI Longitudinal Relaxation Rate (measured in s^{-1})

R2: MRI Transverse Relaxation Rate (measured in s^{-1})

RIT: Radioimmunotherapy

SE: Spin Echo

SNR: Signal to Noise

SRS: Stereotactic Radiosurgery

SSTSE: Single Shot Turbo Spin Echo

SSD: Source to Surface Distance

T1: MRI Longitudinal Relaxation Rate (measured in *s*)

T2: MRI Transverse Relaxation Rate (measured in *s*)

TE: MRI Echo Time

TR: MRI Relaxation Time

THPC: Tetrakis (Hydroxymethyl) Phosphonium Chloride

Theoretical Part

1. Radiotherapy

Cancer remains a leading cause of death globally. It was estimated that 18.1 million new cancer cases and 9.6 million cancer deaths occurred in 2018 worldwide, and, on average, there is about a 20% risk of getting a cancer before age 75, and 10% of dying from it. [1]

The past decade has witnessed a considerable progress towards the treatment and understanding of the earlier proposed hallmarks of cancer [2] and together with advances in early detection and in the various treatment modalities, many cancers have become curable [3]. After the discovery of X-rays in 1895, by Wilhelm Conrad Röntgen from Germany its clinical usefulness, as a means of cancer treatment was first appreciated.

It is also one hundred years ago that Marie Curie won a second Nobel Prize for her research into radium, establishing her position as a pioneer in the field of radiation therapy. To mark this, 2011 has been designated the Year of Radiation therapy in the UK, celebrating a century of advances. Since that time, radiation therapy has developed into a recognized medical specialty with Radiation Oncology being a discipline in which various health and science professionals from numerous disciplines work together.

Along with surgery and chemotherapy, *radiation therapy* or *radiotherapy* remains an important modality used in cancer treatment being a highly cost effective single modality treatment accounting about only 5% of the total cost of cancer care [4].

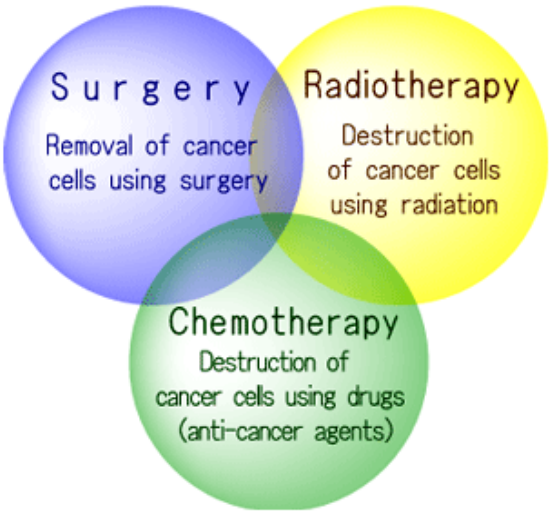

Figure 1.1 Combined action of surgery, radiotherapy and chemotherapy for cancer treatment.

Radiation can be given with the intent of cure as well as being used as a very effective modality of palliative treatment to relieve patients from symptoms caused by the cancer. Further indications of radiation therapy include combination strategies with other treatment modalities such as surgery, chemotherapy or immunotherapy. If used before surgery (neoadjuvant therapy), radiation will aim to shrink the tumor. If used after surgery (adjuvant therapy), radiation will destroy microscopic tumor cells that may have been left behind. It is well known that tumors differ in their sensitivity to radiation treatment. Furthermore, approximately 50% of all cancer patients will receive

radiation therapy during their course of illness [5, 6] with an estimation that radiation therapy contributes to around 40% towards curative treatment [7].

The radiation is usually in the form of focused x-ray beams, also known as photons. It can also be in other forms such as electron beams, proton beams or gamma rays from radioactive sources. It is a localised treatment, which means it generally affects only the part of the body where the radiation is targeted. The rapid progress in this field continues to be enhanced by the development of imaging techniques, computer treatment planning systems, X-ray production systems as well as by understanding the radiobiology of radiotherapy [8]. Although the radiation can also damage healthy cells, these tend to be less sensitive than the cancer cells and can usually repair themselves.

Rapid progress in this field continues to be boosted by advances in imaging techniques, computerized treatment planning systems, radiation treatment machines (with improved X-ray production and treatment delivery) as well as improved understanding of the radiobiology of radiation therapy [8].

1.2 Principles of Radiation Therapy

Radiation is a physical agent, which is used to destroy cancer cells. The radiation used is called ionizing radiation because it forms ions (electrically charged particles) and deposits energy in the cells of the tissues it passes through. This deposited energy can kill cancer cells or cause genetic changes resulting in cancer cell death.

Biological effectiveness (cell killing) of radiation depends on the *linear energy transfer (LET)*, total dose, fractionation rate and radio-sensitivity of the targeted cells or tissues [9, 10]. Low *LET* radiation deposits relatively a small quantity of energy whilst high *LET* radiation deposits higher energy on the targeted areas. Though radiation is directed to kill the tumor cell, it is inevitable that the non-cancerous normal tissues surrounding the tumor also damaged by radiation. However, the goal of radiation therapy is to maximize the dose to tumor cells while minimizing exposure to normal healthy cells [11]. Fractionation is beneficial when the response of the tumor occurs at a total cumulative dose that does not result in severe normal-tissue complications, it is detrimental when there is no separation between the total cumulative doses required to control the tumor and induce normal- tissue complications.

Normal cells can repair themselves faster than cancer cells by regaining normal function. In contrast, cancer cells are generally not as effective at repairing their radiation damage as normal cells. The difference described above, in the radiobiological properties of normal and cancer cells is utilized in radiotherapy. In particular, radiotherapy is applied in fractions for a few weeks and not just once. The implementation of the sessions utilizes and enhances the survival advantage of normal tissues compared to cancer cells, which is based on the different speed of recovery of fatal damage caused by tissue exposure to radiation.

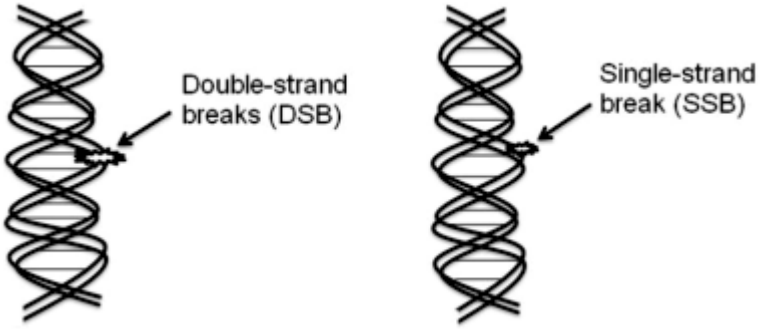

Figure 1.2 Radiation act directly or indirectly on the cellular DNA.

The biological target of radiation in the cell is DNA (*Figure 1.2*). Radiation can directly interact with cellular DNA and cause damage *(Figure 1.3A)*. The indirect DNA damage (radiolysis), caused by the free radicals, is derived from the ionization or excitation of the water component of the cells *(Figure 1.3B)*. Double strand DNA breaks are irreparable and more responsible than the single strand DNA breaks for most of cell killing in cancer as well as surrounding normal cells.

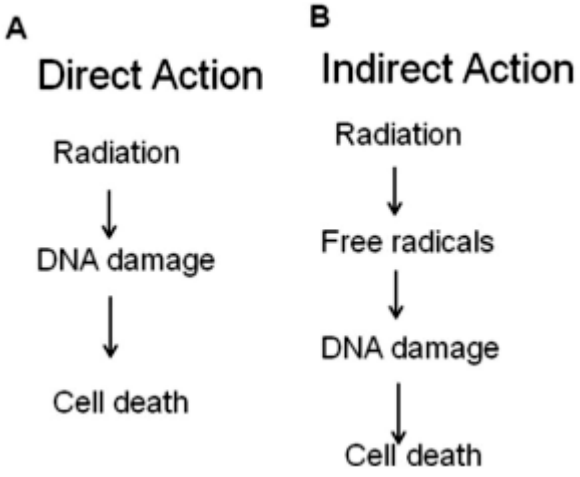

Figure 1.3 Radiation act directly or indirectly on the cellular DNA.

This response of tissues to radiation is called *radiosensitivity*. The more radiosensitive a tumor is, the faster it is destroyed and the less the damage on healthy adjacent tissues (*Figure 1.4a*), while on the contrary, the less radiosensitive a tumor is, the greater the damage on healthy adjacent tissues (*Figure 1.4b*). In addition, normal cells proliferate more slowly compared to the rapid proliferation of cancers, so they have more time to repair their damage before the next session.

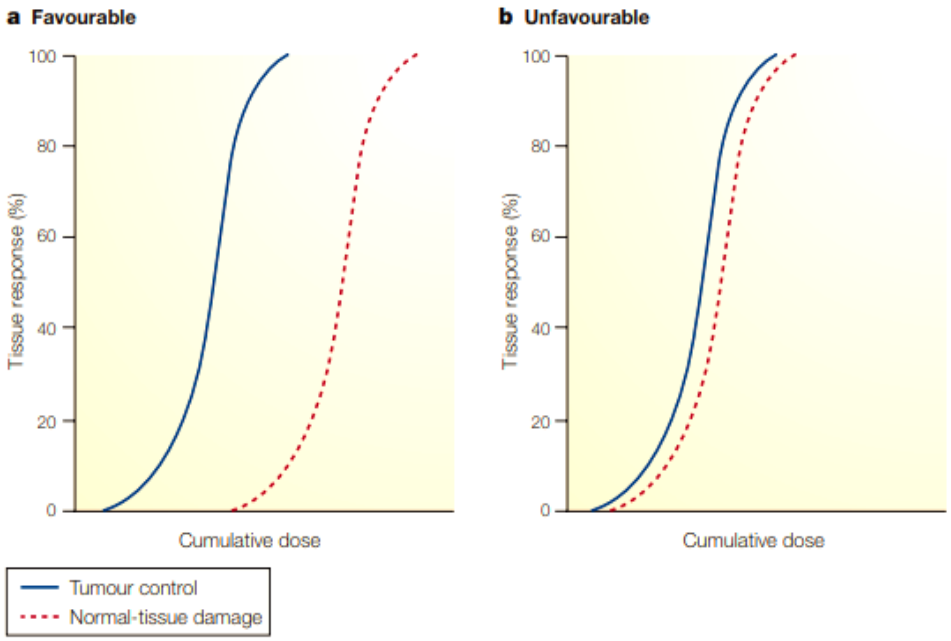

Figure 1.4 Graph to show the therapeutic index with respect to cumulative dose.
a) A favorable outcome would mean that the response of tumor tissue is greater than that of normal tissue to the same dose — the therapeutic index is large.
b) An unfavorable outcome would mean that the response of tumor tissue and normal tissue is similar for the same dose — the therapeutic index is small.

In radiotherapy, the administration of radiation can be either for the radical treatment of a cancerous tumor (therapeutic radiotherapy), or to enhance or supplement the therapeutic effect of a surgery (adjuvant radiotherapy, or the annoying symptoms due to malignancy (palliative radiotherapy). Radiation therapy is applied in combination with other therapeutic techniques (such as surgery, chemotherapy) depending on the desired result.

1.3 Types of Radiotherapy

Radiation is a type of energy that can travel through space. Sometimes it travels in the form of a wave. That's called *electromagnetic radiation*. Sometimes, it travels as a beam of fast-moving particles. That's called *particle radiation*. Radiation is all around you! And it's been there all your life.

Electromagnetic radiation (EMR) consists of waves. The waves contain electric and magnetic energy. The electromagnetic spectrum (EMS) includes different types of energy waves. At one end of the spectrum, there are very low energy waves. Radio waves are an example of low energy waves. At the other end of the spectrum, there are very high energy waves. Gamma rays are an example of high energy waves (*Figure 1.5*). [12]

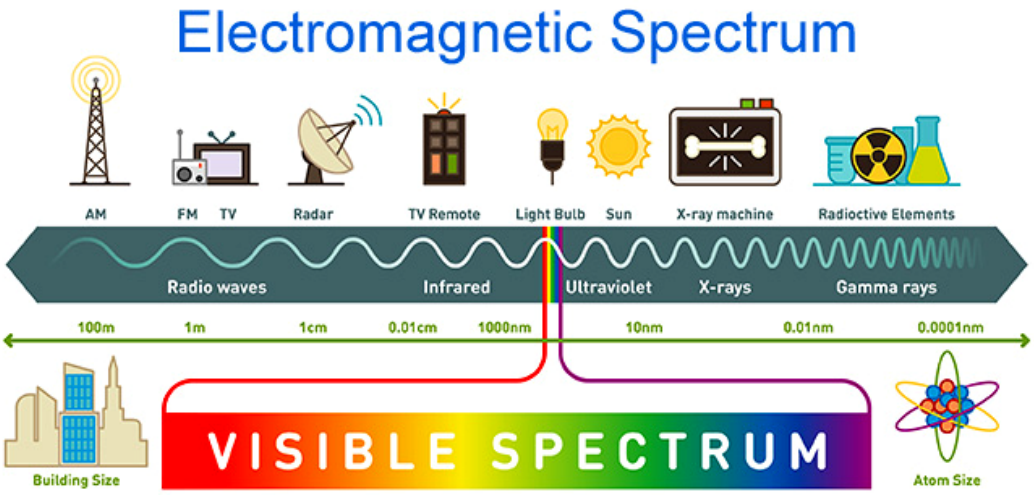

Figure 1.5 The electromagnetic spectrum encompasses wavelengths from radio waves to gamma rays, both selectively emitted and absorbed by various objects

Frequency and wavelength are used to describe EMR. Frequency refers to the number of waves per second. Wavelength refers to the distance between two adjacent wave peaks. The higher a wave's frequency, the shorter its wavelength. For example, gamma rays have a very small wavelength and very high frequency. They also have a lot of energy!

There are seven natural forms of EMR. Gamma rays have the highest energy and shortest wavelength. Then come X-rays, ultraviolet light, visible light, infrared radiation and microwave radiation. Finally, radio waves have the lowest energy and longest wavelength. You can only sense two parts of the EMS. You can feel infrared radiation and you can see visible light. Radio waves, X-rays and gamma rays can pass through your body. But you can't see them or feel them.

Electromagnetic radiation travels in little packets (quanta) of energy. These charge-less bundles of energy are called photons. They travel at the speed of light ($2.998 \times 108\ m/s$) in a vacuum.

Radiation therapy can be delivered two ways – *externally* and *internally*.

- ***External radiation therapy*** delivers radiation using a linear accelerator.
- ***Internal radiation therapy***, called *Brachytherapy or seed implants*, involves placing radioactive sources inside the patient.

The type of therapy used will depend on the location, size and type of cancer.

External Beam Radiotherapy (EBRT)

External beam radiation therapy is radiation of either photons or particles, delivered from a distant source, from outside the body and directed at the patient's cancer site. Systems which produce different types of radiation for *external beam therapy* include orthovoltage *X-ray machines*, *Cobalt-60 machines*, *linear accelerators*, *proton beam machines*, and *neutron beam machines*.

A radiation oncologist makes decisions regarding the type of system that is best suited to treat a specific cancer patient. External beam therapy is the radiation therapy treatment option used for most cancer patients. It is used to treat many types of tumors including cancers of the head and neck area, breast, lung, colon, and prostate.

Depending upon tumor location, different levels of radiation are used for external beam therapy. Low-energy radiation does not penetrate very deeply into the body and is used mainly to treat surface tumors such as skin cancer. High-energy radiation is used to treat other deeper cancers.

External radiotherapy techniques are divided into two major categories:

A. Teletherapy techniques
B. Stereotactic techniques

A. Teletherapy techniques *consist of:*

i. 2D Conventional Radiotherapy

This technique is the oldest and simplest method of radiotherapy. Treatment planning is done in two dimensions, from two vertical images taken by the patient. Its main disadvantage is that healthy tissues are irradiated with the same intensity as cancer cells.

ii. 3D Conformal Radiotherapy, 3D CRT

In this technique, the treatment is designed in three dimensions, taking into account the three-dimensional shape of the target tumor, irradiating the tumor with the greatest possible accuracy and at the same time protecting the adjacent healthy tissues.

The main features of the method are the three-dimensional (3D) determination of the target tumor, the three-dimensional (3D) treatment plan system and the three-dimensional (3D) radiation production system. Accurate determination of the target tumor is achieved through anatomical and functional imaging techniques. The treatment planning is achieved: a) either by the regular planning method (*forward planning*), where the beams of uniform intensity are produced that produce a radiation field of the same shape as that of the target tumor, b) or by the *reverse treatment planning*, where the beams are formed using multiple modulated tension beams to maximize dose to target volume and minimize burden on adjacent healthy tissues [17]. The radiation generating system can produce level beams of uniform intensity up to non-level beams of modulated intensity using *Multi Leaf Collimators* (*MLC*).

iii. Intensity Modulated Radiation Therapy, IMRT

A basic principle of this method is that the administered radiation dose is adjusted in three dimensions depending on the shape of the tumor by modulating the intensity of the radiation beam.

This technique is an advanced form of 3D Conformal Radiation Therapy (3D CRT). Compared to 3D CRT, the same procedure is followed but It has two key additional features compared to conformal radiotherapy [18]:

1. Non-uniform intensity of the radiation beams.
2. Computerized inverse planning.

iv. Volumetric Modulated Arc Therapy (VMAT)

Arc-shaped intensity radiotherapy is the most advanced radiotherapy technique. In this technique the machine performs a complete rotation of 360 degrees around the patient, always irradiating the target

tumor but each time approaching through different healthy tissues, minimizing the dose received by each of them.
During the rotation it is possible to change the gantry velocity and the dose rate. At the same time the multi-leaf linear accelerator constantly changes the shape of the field without interrupting the irradiation. Obviously, the VMAT technique has the advantage of optimal irradiation in the shortest possible time with maximum dose accuracy [24].

v. Tomotherapy

This technique is a combination of IGRT and IMRT. Its innovation is based on the fact that the radiation is delivered per section to the patient.

B. Stereotactic techniques

A feature of *Stereotactic Radiotherapy* or *Radiosurgery (SRS)* is the administration of a high dose of radiation to a high-precision target. It is not surgery in the traditional sense because there's no incision. Instead, stereotactic radiosurgery uses 3D imaging to target high doses of radiation to the affected area with minimal impact on the surrounding healthy tissue.

Like other forms of radiation, stereotactic radiosurgery works by damaging the DNA of the targeted cells. The affected cells then lose the ability to reproduce, which causes tumors to shrink. Its name is based on two reasons: ***a)*** the radiation that is directed to a stereotactically determined target tumor, destroying it as if it were operating without bloodshed, and ***b)*** the immobilization of the part of the body that will be irradiated, while shielding the neighboring tissues.

Stereotactic techniques consist of:

i. Gamma Knife

Gamma Knife is the first radiation production machine in Stereotactic Radiotherapy. This system includes *201 cobalt-60 sources*, integrated in the system head. The sources are located on a hemispherical surface with a radius of 40 cm, which consists of five concentric circles (Figure 1.7). Each source consists of 20 cylindrical capsules, which are placed one on top of the other, forming a cylinder (height = 20mm, radius = 1mm) that has a stainless steel casing. Depending on the size of the beam needed for treatment, the appropriate collimator is used. The beams, depending on the size of the collimator bore have diameters of 4, 8, 14 and 18 mm. The final radiation field is created by the use of the appropriate concentric cycle, whose Cobalt-60 sources will produce the beams. Finally, based on the information in the treatment plan, the treatment time and the guide or guides to be used are determined so that the radiation field that will be created will provide the coverage of the target tumor [17].

Figure 1.7 Gamma Knife Unit

ii. Cyber Knife

Cyber Knife is a revolutionary new technique in Stereotactic Radiosurgery using a linear accelerator, which combines both precise positioning of the target tumor and stereotactic radiation dose administration. This technique provides non-invasive precision tumor positioning in combination with a small linear accelerator mounted on the robotic head of a machine, which can rotate around the patient's body and radiate in any desired direction. This technology allows the Cyber Knife to provide additional refinements to the stereotaxing technique. In particular, this technique allows the non-use of a stereotactic framework, the destruction of inaccessible tumors non-invasively only with the use of radiation, the continuous imaging and monitoring of the patient's position during treatment, determining the position of the target tumor relative to the treatment room coordinate system and allows the radiation dose to be delivered with high accuracy (in the order of millimeters) through an imaging-guided dose delivery system [17].

iii. X Knife

Megavoltage X-rays from medical linear accelerators are used to perform a high-precision technique using external photon beams. Medical linear accelerator-based radiosurgery system (X-Knife) uses either narrow circular cones or micro multileaf collimators (MLC) to shape the treatment fields. These machines can perform stereotactic radiosurgery (SRS) in a single session or over three to five sessions for larger tumors, which is called fractionated stereotactic radiotherapy.

Internal Radiation Therapy (Brachytherapy)

Brachytherapy involves placing radiation sources as close as possible to the tumor site. Sometimes, they may be inserted directly into the tumor. The radioactive sources or isotopes are in the form of wires, seeds (or molds), or rods. This technique is particularly effective in treating cancers of the cervix, uterus, vagina, rectum, eye, and certain head and neck cancers. It is also occasionally used to treat cancers of the breast, brain, skin, anus, esophagus, lung, bladder, and prostate.

In some instances, brachytherapy may be used in conjunction with external beam therapy. When both forms are employed, the external beam radiation is intended to destroy cancerous cells in a large area surrounding the tumor, while the brachytherapy delivers a boost, or higher dose of radiation, to help destroy the main concentrated mass of tumor cells. [19]

Brachytherapy can be subdivided into *categories* depending on the position of the sources to the tumor, the duration of the therapy and the way the radioactive sources are charged [20, 21]. These categories are divided:

1. *Depending on the position of the sources in relation to the volume*

    - *Intracavity brachytherapy*, in which the radiation source is placed within the tumor. This technique is used for prostate cancer, for instance.
    - *Interstitial brachytherapy*, in which the radioactive sources are close to the tumor and remain in place for as long as it takes to deliver the desired dose. Then, they are removed and the patient can return to his environment without fear.

2. *Depending on the dose rate of radiation per hour*

The dose rate therefore reflects the duration of brachytherapy [22, 23]:

- ***Low-dose rate (LDR) :*** *0.4 - 2Gy / hr* or *10 Gy* per *day*
- ***Medium-dose rate (MDR) :*** *2 - 12 Gy / hr* or *10 Gy* per *hour*
- ***High-dose rate (HDR):*** *> 12Gy / hr* or *10 Gy* per *minute*
- ***Pulsed dose rate (PDR):*** It combines the *HDR brachytherapy* and the duration of *LDR brachytherapy*.

Monitor unit calculations for photon and electron beams

The International Commission on Radiation Units and Measurement *(ICRU)* states that dosimetry systems must be capable of delivering dose to an accuracy of 5%. Furthermore, improvements in this level of accuracy are warranted to improve the modeling and prediction of dose-volume effects in radiation therapy. Many factors contribute to both random and systematic deviations in dose delivery, including daily patient setup, target delineation, and dose calculation. The accurate determination of dose per monitor unit (*MU*) at a single calculation point is an essential part of this process. For photons, MU calculations for fields with and without beam modifiers for both isocentric and source-surface distance (*SSD*) setups were made.

Factors influencing calculation of Monitor Units

A monitor unit is based on a certain set of beam setup parameters, and beams different to this setup need to be corrected to ensure correct dose is delivered. The factors influencing this correction are:

- ***Beam Energy***. Typically each beam energy on a linac will have its own monitor unit calculation for a standard field.
- ***Source Surface Distance***. An increased SSD will mean that increased monitor units will be required to deliver a dose at depth due to the effects of the inverse square law. This must be taken into account, and is usually only a problem for extended SSD treatments (using a fixed SSD technique)
- ***Tissue-Phantom Ratio / Tissue-Maximum Ratio (TPR)***. Used for ***fixed source-axial distance calculations*** only. The TPR/TMR describes the dose rate relative to a dose rate for a similar beam at a different depth within the target. This allows a monitor unit correction to take into account different depths of a target.
- ***Percentage Depth Dose (PDD)***. Used for ***fixed source-surface distance*** calculations only. The PDD describes the dose rate at different depths within a target for an equal source-surface distance. If the target is located at a different depth to the standard field, monitor units will need to be adjusted.
- ***Output Factor (OF)***. The output factor is change in dose rate that occurs with different field sizes. Large fields will usually have a higher output factor, leading to increased dose rates for the same number of monitor units.
- ***Wedge Factor (WF)***. Takes into account the effect of the wedge on the attenuation of the radiation beam. If a wedge is present, increased monitor units will be required to reach the same dose.
- ***Calibration Factor (CF)***. Not commonly used, typically 1 in most scenarios.

Fixed SSD Technique

$$MU = \frac{cGy \cdot SSD}{CF \times (OF \times PDD \times WF)}$$

References

1. Ferlay J, Colombet M, Soerjomataram I, et al. Estimating the global cancer incidence and mortality in 2018: GLOBOCAN sources and methods. *Int J Cancer*. 2019;144(8):1941-1953. doi:10.1002/ijc.31937
2. Hanahan D, Weinberg RA. Hallmarks of cancer: the next generation. *Cell*. 2011;144(5):646-674. doi:10.1016/j.cell.2011.02.013
3. Pollack LA, Rowland JH, Crammer C, Stefanek M. Introduction: charting the landscape of cancer survivors' health-related outcomes and care. *Cancer*. 2009;115(18 Suppl):4265-4269. doi:10.1002/cncr.24579
4. Ringborg U, Bergqvist D, Brorsson B, et al. The Swedish Council on Technology Assessment in Health Care (SBU) systematic overview of radiotherapy for cancer including a prospective survey of radiotherapy practice in Sweden 2001--summary and conclusions. *Acta Oncol*. 2003;42(5-6):357-365. doi:10.1080/02841860310010826
5. Delaney G, Jacob S, Featherstone C, Barton M. The role of radiotherapy in cancer treatment: estimating optimal utilization from a review of evidence-based clinical guidelines [published correction appears in Cancer. 2006 Aug 1;107(3):660]. *Cancer*. 2005;104(6):1129-1137. doi:10.1002/cncr.21324
6. Begg AC, Stewart FA, Vens C. Strategies to improve radiotherapy with targeted drugs. *Nat Rev Cancer*. 2011;11(4):239-253. doi:10.1038/nrc3007
7. Barnett GC, West CM, Dunning AM, et al. Normal tissue reactions to radiotherapy: towards tailoring treatment dose by genotype. *NatRevCancer*. 2009;9(2):134-142. doi:10.1038/nrc2587
8. Bernier J, Hall EJ, Giaccia A. Radiation oncology: a century of achievements. *NatRevCancer*. 2004;4(9):737-747. doi:10.1038/nrc1451
9.]Hall EJ. Cancer caused by x-rays--a random event?. *Lancet Oncol*. 2007;8(5):369-370. doi:10.1016/S1470-2045(07)70113-4
10. Baskar R. Emerging role of radiation induced bystander effects: Cell communications and carcinogenesis. *Genome Integr*. 2010;1(1):13. Published 2010 Sep 12. doi:10.1186/2041-9414-1-13
11. Emami B, Lyman J, Brown A, et al. Tolerance of normal tissue to therapeutic irradiation. *Int J RadiatOncolBiol Phys*. 1991;21(1):109-122. doi:10.1016/0360-3016(91)90171-y
12. https://letstalkscience.ca/educational-resources/backgrounders/what-are-different-types-radiation
13. https://training.seer.cancer.gov/treatment/radiation/types.html
14. Mosleh-Shirazi MA. Radiotherapy techniques for intracranial tumours.*Iran J Radiat Res*. 2006;4(2):53-62.
15. Mallick I, Waldron JN. Radiation Therapy for Head and Neck Cancers.*SeminOncolNurs*. 2009;25(3):193-202. doi:https://doi.org/10.1016/j.soncn.2009.05.002
16. Noda SE, Lautenschlaeger T, Siedow MR, et al. Technological advances in radiation oncology for central nervous system tumors. *SeminRadiatOncol*. 2009;19(3):179-186. doi:10.1016/j.semradonc.2009.02.006
17. Rosenberg I. Radiation Oncology Physics: A Handbook for Teachers and Students. *Br J Cancer*. 2008;98(5):1020. doi:10.1038/sj.bjc.6604224
18. Taylor A, Powell ME. Intensity-modulated radiotherapy--what is it?. *Cancer Imaging*. 2004;4(2):68-73. Published 2004 Mar 26. doi:10.1102/1470-7330.2004.0003
19. Korreman S, Rasch C, McNair H, et al. The European Society of Therapeutic Radiology and Oncology-European Institute of Radiotherapy (ESTRO-EIR) report on 3D CT-based in-room image guidance systems: a practical and technical review and guide. *RadiotherOncol*. 2010;94(2):129-144. doi:10.1016/j.radonc.2010.01.004

20. Hannoun-Levi, J. M., Chevallier, D., Cosset, J. M., & Gerbaulet, A. (2012). L'évolution de la curiethérapie du cancer de prostate [Evolution of prostate cancer brachytherapy]. Bulletin du cancer, 99(12), 1175–1181. https://doi.org/10.1684/bdc.2012.1668
21. HENSCHKE, U. K., HILARIS, B. S., & MAHAN, G. D. (1963). AFTERLOADING IN INTERSTITIAL AND INTRACAVITARY RADIATION THERAPY. The American journal of roentgenology, radium therapy, and nuclear medicine, 90, 386–395.
22. Wambersie, A., Chassagne, D., Dutreix, A., Almond, P., Ash, D., Burgers, M., Bush, M., Cohen, M., Hanson, W., Joslin, C., Landberg, T., Visser, A., & Wilson, F. (1996). Quality assurance in brachytherapy: the role of the ICRU in achieving uniformity in dose and volume specification for reporting. Rays, 21(4), 541–558.
23. Wambersie, A., Chassagne, D., Dutreix, A., Almond, P., Ash, D., Burgers, M., Bush, M., Cohen, M., Hanson, W., Joslin, C., Landberg, T., Visser, A., & Wilson, F. (1996). Quality assurance in brachytherapy: the role of the ICRU in achieving uniformity in dose and volume specification for reporting. Rays, 21(4), 541–558.
24. Iorio, G. C., Franco, P., Gallio, E., Martini, S., Arcadipane, F., Bartoncini, S., Rondi, N., Giglioli, F. R., Ala, A., Airoldi, M., Donadio, M., De Sanctis, C., Castellano, I., & Ricardi, U. (2017). Volumetric modulated arc therapy (VMAT) to deliver nodal irradiation in breast cancer patients. Medical oncology (Northwood, London, England), 35(1), 1. https://doi.org/10.1007/s12032-017-1061-8

2. Nuclear Magnetic Resonance (NMR)

2.1 The interpretation of the phenomenon

Nuclear magnetic resonance (NMR) is a physical phenomenon that occurs when certain elements interact with a magnetic field. NMR is the process by which the signal detected in MRI is generated, it is the foundation on which MRI is built.

By analyzing the term NMR, anyone could easily identify precisely the meaning of the terms associated with them. The term "Nuclear" refers to the nucleus of the atoms of matter, from which the signal we receive is derived. By the term "Magnetic", we refer to the property of space, to which the phenomenon is directly related, and this is the magnetic field of the atomic nuclei of matter. Finally, the term "Resonance" refers essentially to the method by which the signal is recorded in the NMR. In addition, resonance is the phenomenon in which the excitation frequency of the transmitter is equal to the effect of the receiver.

In other words, it is a phenomenon observed in the microcosm of matter, and in particular in the nuclei of such atoms. It is related to the magnetic field of the subatomic space, for which we obtain information by the method of resonance. To achieve resonance, each transmitter has to have the same frequency of excitation as its respective 'receiver', so that a strong energy-coupling can take place between the two.

Specifically in Nuclear Magnetic Resonance the role of the transmitter and the receiver are alternately played by the nucleus and the transmitting/receiving coil. It has established itself as a double-time phenomenon. In the initial time, the coil, as an electromagnetic pulse transmitter excites through resonance the nuclei of the atom as a receiver. In the second time, the core becomes this transmitter and the coil is now received as the coil of the electromagnetic signal transmitted by the nuclei.[2]

NMR is based on the presence of two properties of the atom: Magnetism and Spin angular Momentum. The protons within the nucleus of any atom contain electric charge and generate a magnetic field. Whereas it is tempting to think of such nuclear magnetism in terms of classic electromagnetic phenomena with spinning charges generating a magnetic field based on Faraday's law of induction, nuclear magnetism is in fact a quantum mechanical phenomenon, and nuclear particles do not, as currently understood, actually spin in the physical sense.

2.1.1 Nuclear Magnetism

Nuclear magnetism does, nonetheless, result in a very real magnetic field that is local to the nucleus and behaves just like the magnetic field of a permanent magnet or compass needle. Magnetic field lines describe this nuclear magnetic field and are identical to those generated by a common bar-shaped permanent magnet.

Field lines are very real and a useful way to describe the strength, orientation, and homogeneity of a magnetic field. For our descriptions of nuclear magnetism, however, it will suffice to describe the magnetic field of the nucleus using a single vector. The orientation of this magnetic field vector will indicate the orientation of the nuclear magnetic field, and the length of the vector will indicate the strength of the field.

In the absence of any magnetic field external to the nucleus, orientation of the nuclear magnetic field will be random. In the presence of an externally applied magnetic field, however, the nuclear magnetic field will align with the externally applied magnetic field, much as a compass needle aligns with the earth's magnetic field.

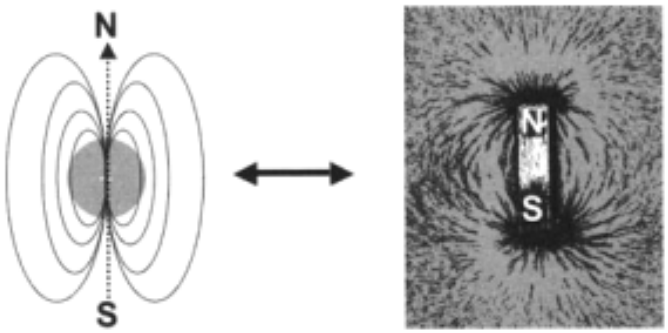

Figure 2.1 The proton's magnetic field. The magnetic field lines of a common bar magnet (right) are shown by the distribution of iron filings. The magnetic field of a proton (left) behaves in the same manner, exhibiting field lines and polarity identical to those produced by the bar magnet.[2]

At this point, we have described the magnetism of the 'H nucleus and can see that our proton essentially behaves as a tiny magnet, aligning with an external applied magnetic field. To demonstrate *NMR* and be useful for *MRI*, however, the proton must also have *Spin angular Momentum*.

2.1.2 Nuclear Spin Angular Momentum

Spin angular momentum is a property of certain nuclei (those that exhibit NMR). Its existence becomes apparent when we observe the interaction of such a nucleus with an externally applied magnetic field.

The physical phenomenon that produces this centrifugal force is called angular momentum. The same force causes the wobble of a spinning top. Spin angular momentum is an analogous force that is applicable to small particles such as atomic nuclei. [5]

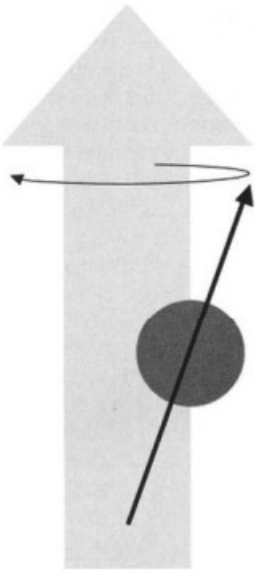

Figure 2.2 Precession. Interaction of magnetic field of the proton with an applied magnetic field leads to precession. The vector describing the proton's magnetic field circles that describing the static magnetic field. Its path traces the surface of a cone. [5]

Now let's see what happens at the same phenomenon as it pertains to nuclei. Nuclei have charge that confers nuclear magnetism. When placed in an externally applied magnetic field, they will interact with that field in much the same way as a compass needle interacts with the earth's magnetic field: they will oscillate. If the nucleus also has spin angular momentum, it will not oscillate but will *precess* around the externally applied magnetic field, pursuing the same type of conical trajectory described above.

Moreover, *Nuclear Spin* is a quantum mechanical phenomenon describing the behavior of very small particles. It is proportional to spin angular momentum, so more *spin* actually means *greater spin angular momentum.*

Nuclear Spin is described by the spin number, it is equal to either 0, a whole integer, or a noninteger multiple of $^1/_2$:

- Spin = 0, if there are an even number of both protons and neutrons. Such nuclei (like *He*) do not exhibit NMR
- Spin is an integer if there is an odd number of both protons and neutrons.
- Spin is a noninteger multiple of $^1/_2$ for all other nuclei.
- Spin ranges from 0 to 7, that means higher spin number = greater spin angular momentum.

2.2 The Nuclear World

From Bohr's atomic model, we know that atoms are composed of the nucleus and the electrons rotating around them. Two important properties of the nucleus and the electrons are their charge and their spin around their axis.

The nucleus consists of protons and neutrons. Protons are positively charged, neutrons have no charge, and electrons are negatively charged. We define as Atomic Number, the number of protons in the nucleus and as Mass Number, the sum of the protons and neutrons in the nucleus. The nucleus revolves around its axis, the electrons around it, but also around their axis.

From the beginning of electromagnetism, we know that moving (or even rotating) electric charges induce a magnetic field or otherwise exhibit a magnetic dipole moment due to self-rotation. Neutrons which appear electrically neutral as a whole exhibit a magnetic dipole moment due to the uneven radial distribution of their electric charge.

Thus a kernel with *even* Mass Number will be magnetically *inactive*, as the individual magnetic dipole moments will mutually neutralize. Conversely, cores with an unnecessary Mass Number will be magnetically *active*, that is, they will exhibit magnetic dipole moment. Nuclear Magnetic Resonance can be applied to these cores. Such nuclei are ^{1}H Hydrogen, ^{31}P Phosphorus, ^{32}Na Sodium, and ^{13}C Carbon.

Magnetic Resonance Imaging utilizes the magnetically active *Hydrogen nuclei* as they consist of a single proton, exhibit high magnetic dipole moment and are abundant in the human body in water and fat molecules. [13]

In the above discussion, reference was made to the notions of angular momentum and magnetic dipole momentum of the particles. It is important to note that these classical concepts, when referring to microcosm particles (protons, neutrons, electrons, quarks), acquire a particular *quantum character*. In general, the concepts of spin are squared quantities when describing states of microcosm particles.

2.2.1 The Hydrogen Core

Although many nuclei can undergo NMR, we will confine our discussion to the hydrogen nucleus ($^{1}_{1}H$). In human tissue, which is composed largely of hydrogen-containing water (H_2O), hydrogen is the most abundant of all the NMR-capable nuclei. For this reason, human MRI is focused almost exclusively on hydrogen.

The nucleus of the hydrogen atom consists of a single nucleon (a proton A = Z = 1). The hydrogen proton revolves around its axis at a *total angular momentum I* and the only contribution to it is that of *Spin* (*S*). Therefore, it will induce a magnetic field parallel to its axis of rotation and thus it will behave like a self-rotating small magnet with a magnetic dipole moment equal to:

$$\boldsymbol{\mu = \gamma \cdot I} \quad \textbf{(1)}$$

, where γ is the gyromagnetic ratio and is characteristic for each nucleus.

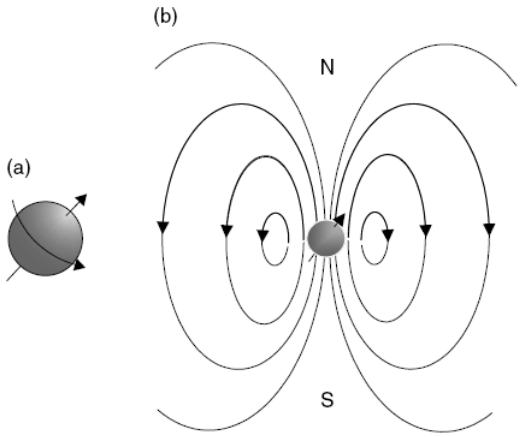

Figure 2.3 (a) The proton rotation, (b) The induced magnetic field.[2]

So, *Spin* determines the gyromagnetic ratio. This constant value is unique for each element and independent of magnetic field strength. It describes the strength of the NMR response (*the frequency of precession* ω) of a nucleus, and, thus, we will see it directs how we will be able to detect that nucleus using NMR.

2.3 Kernels in a Magnetic Field

In free space, without the presence of a magnetic field, the vectors of the magnetic moments of the magnetically active nuclei are irregularly arranged in space, resulting to a measurement of a zero component of them.

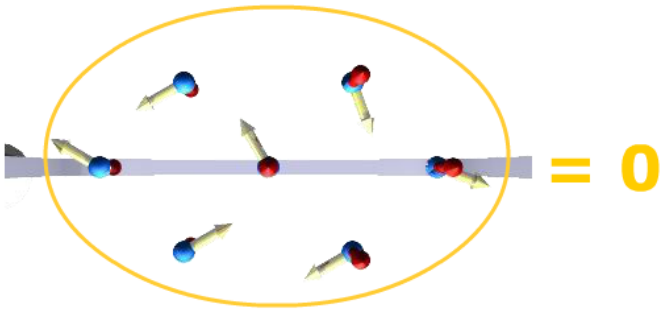

Figure 2.4 Magnetic momentums in absence of a magnetic field.[15]

On the contrary, in the presence of an external magnetic field, the vectors of the magnetic moments, of the active magnetic nuclei, are oriented either parallel or approximately anti-parallel to the strong magnetic field. The phenomenon of the orientation of magnetic moments is explained by the classical and the quantum theory.

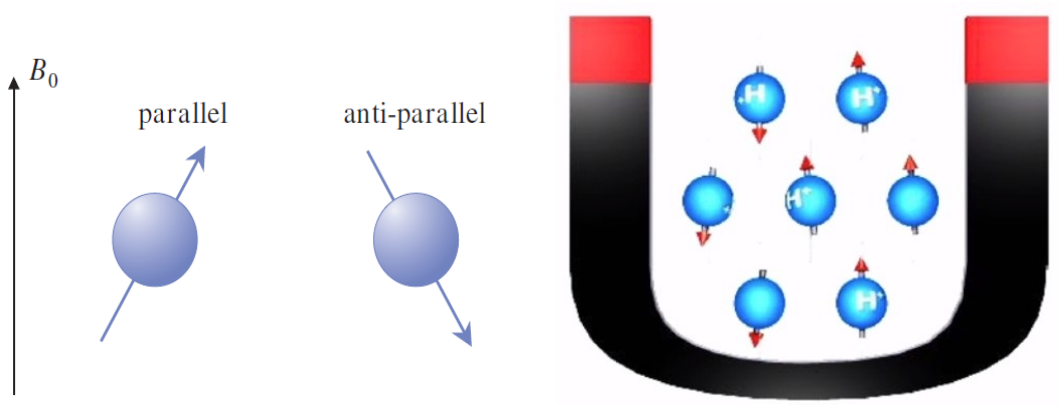

Figure 2.5 Orientation of magnetic moments in the magnetic field. [15]

This orientation is described by the laws of quantum mechanics, according to which the number of cores with parallel spin to B_0, will be slightly greater than the number of counter-spin orientations to B_0. When a sample with multiple nuclei (e.g. water) is placed within a magnetic field, then the microscopic volumes of the sample are characterized by a magnetic dipole moment, called *isochromatic*. The vector sum of all isochromes in the sample is called *total* or *net magnetization (M)*.

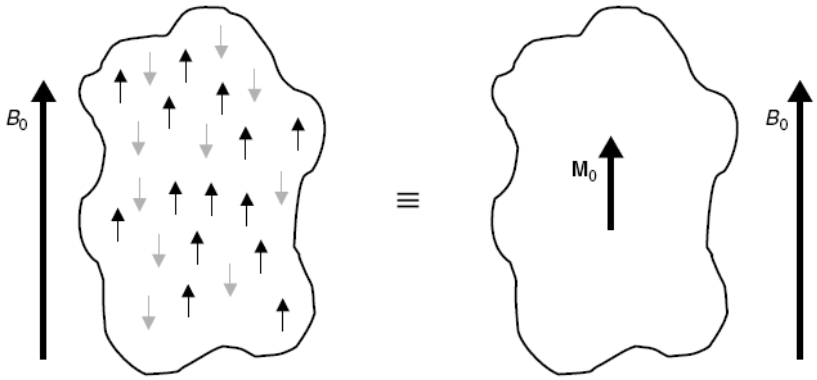

Figure 2.6 Net Magnetization M [2].

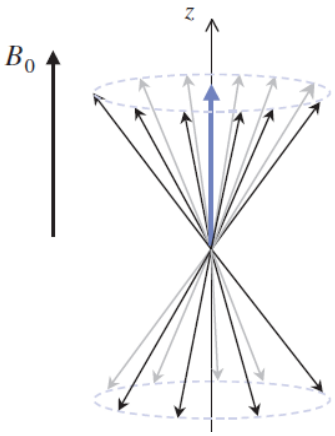

Figure 2.7 Schematic illustration of an isochromatic sample of nuclei in a magnetic field.[6]

Ideally, in a homogeneous magnetic field, all isochromats shift with the same Larmor frequency, but with a different phase. Thus two cones are formed that correspond either to the parallel or the antiparallel orientation of the isochromats with the applied magnetic field. This movement is called a *Larmor precession* or *precession*. The angular frequency precession ω_0 (Larmor frequency) depends on the intensity of the external magnetic field B_0.

The behavior of protons placed in a magnetic field is similar to the behavior of a spinning top placed in the gravitational field of the earth. A spinning top is simply an object with mass that rotates about its own axis. Just as an object moves in a straight line has linear momentum (equal to mass multiplied by linear velocity), an object that spins will have an associated angular momentum. Whereas linear momentum is directed along the line of motion of an object, angular momentum is directed along the line around which the object rotates (Figure 8). For a spinning top, the angular momentum is directed along the axis of the top.

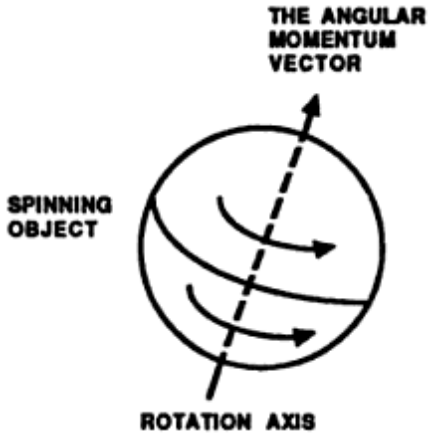

Figure 2.8 A spinning object generates an angular momentum, a vector quantity that has both magnitude and direction. The direction is along the line of the axis of rotation. [2]

If not spinning, a top that is placed on its tip will simply fall over due to the effects of gravity. If spinning rapidly, the top will initially remain upright when placed on its tip. In this position, the axis of the top will be perfectly aligned with the gravitational field of the earth. Due to frictional forces, the top will spin more slowly over time. As it slows down, the top will begin to tip over time. As it slows down, the top will begin to tip over such that the axis of the top is no longer aligned with the gravitational field of the earth. When this occurs, it can be shown mathematically that the force of gravity exerts a torque on the spinning top and changes its angular momentum such that the top rotates about the axis of the gravitational field (*Figure 2.9*).

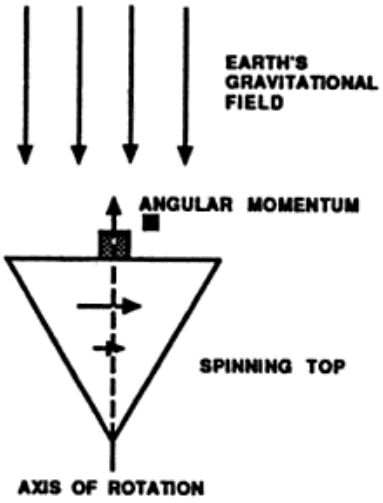

Figure 2.9 The axis of rotation of a spinning top and its angular momentum vector are aligned with the gravitatiol field of the earth.

This rotational motion is usually referred to as *precession*. Precessional motion will occur as long as the top continues to spin about its own axis. The frequency of the precessional motion is inversely proportional to the angular momentum of the top (i.e. the slower the top spins, the faster is the rate of precession) and directly proportional to the gravitational field strength.

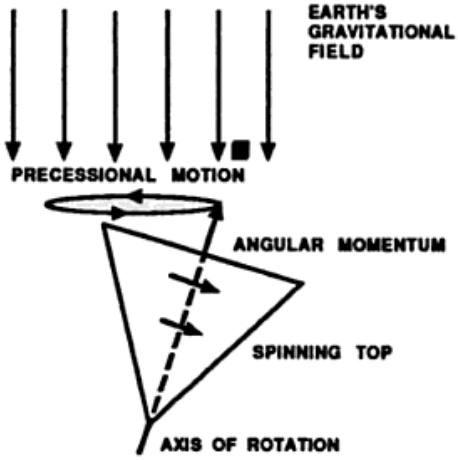

Figure 2.10 As the spinning of top slows, the gravitational force changes the angular momentum. The top starts to wobble, or precess. The rate of precession depends on the angular momentum and the strength of the gravitational force.

So when protons are placed in an external magnetic field, they behave in a manner identical to a spinning top placed in a gravitational field. As long as the angular momentum of the particles remains aligned with the axis of the external field, they will "spin" undisturbed. However, if this alignment is disturbed, the external magnetic field exerts a torque on the protons and they will precess about the axis of the external field.

This type of movement, as well as any movement that involves the additional deflection of the rotation axis of a body precessing, is called *nutation*. The corresponding angle of precession is called the nutation angle. The frequency of precession ω_0 (*Larmor frequency*), depends on the intensity of the external magnetic field B_0. The circular frequency ω_0, for the precessional motion of the nuclear impulse $\boldsymbol{I}$ or the magnetic dipole moment $\boldsymbol{\mu}$ around B_0, is expressed as:

$$\omega_0 = \gamma \cdot B_0 \ (2)$$

This equation is known as the Larmor equation. The constant γ is called the gyromagnetic ratio and has a value of *42.6 MHz/Tesla* for the proton. The Larmor frequency (ω_0) of this precessing motion is stable and its value depends on the magnitude of the magnetic field B_0 and on the value of the total nuclear gyromagnetic ratio γ.

This is also known as the *Resonance frequency*, as the protons only absorb energy (or resonate) at this characteristic frequency. The *RF* field is normally applied as a short pulse, known as an *RF* pulse.

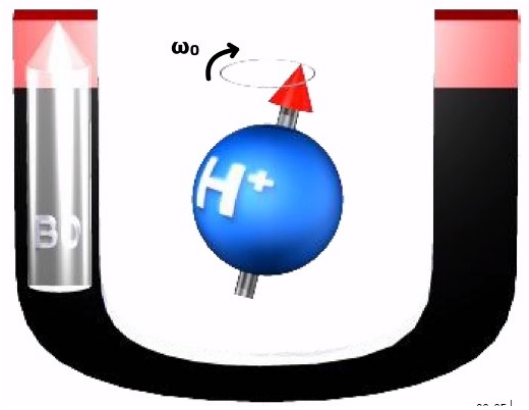

Figure 2.11 Larmor precession [15].

The Larmor frequency is therefore proportional to the strength of the magnetic field and for 1.5 Tesla, the Larmor frequency is approximately *64 MHz*. If the magnetic field intensity changes, so does the *frequency of precession* of the respective nucleus. The cores that will 'feel' the effect of a smaller magnetic field will shift more slowly than those of a bigger magnetic field intensity B_0.

2.4 Rotating Coordinate System

The study and description of motion of the total nuclear magnetism vector in the NMR phenomenon, is made much simpler by using a properly selected rotating coordinate system, instead of a fixed Cartesian system.

So we define, in the magnetic field B_0 direction, the longitudinal axis z of the Cartesian coordinate system ***(xyz)*** and ***xy*** the transverse plane. To facilitate our study, we define the rotating coordinate system ***(x'y'z')***, in which the z' axis has the same direction as the z axis and B_0, while the whole system rotates around the z' having a rotation frequency equal to the Larmor frequency. As a result, the spins are immobile in this system, while the non-coordinating spins are switched with a frequency which is the difference between their frequencies and the tuning frequency, in other words they move with a higher or lower frequency than the tuning frequency and it seems like they're

actually winning or losing phase, respectively. From now on, in order to distinguish which system we are using, we will call ***x***, ***y*** and ***z*** the axes in the fixed coordinate system and ***x'***, ***y'*** and ***z'*** the axes in the rotating system.

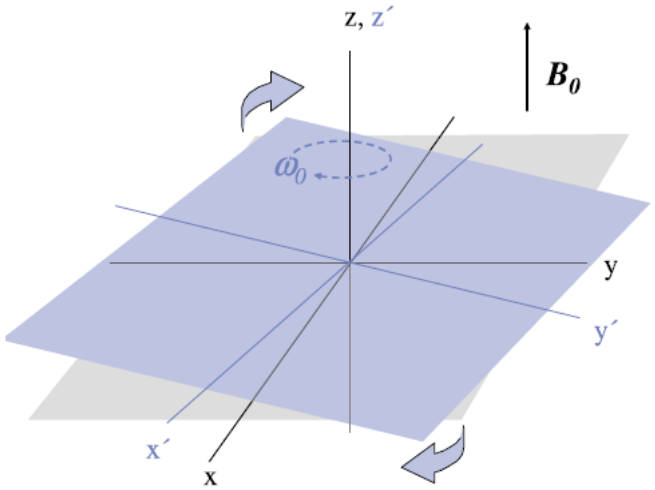

Figure 2.12 The rotating coordinate system. The Cartesian coordinate system x', y', z' is considered to be spinning in the Larmor frequency in the same direction as the nuclear spins, which appear in real estate.[2]

The result is that the nuclei which are precessing, with a frequency equal to the Larmor frequency, appear stationary. In contrast with the nuclei, which move at a higher or lower frequency than the Larmor frequency, which look as they are "winning" or "losing" phase respectively.

By convention, magnetization along the direction of the applied magnetic field is referred to as *longitudinal* magnetization and magnetization in the plane perpendicular to the external field is referred to as *transverse* magnetization. Also by convention, when using a Cartesian coordinate system, the direction of the external field is defined as the ***z*** axis and the transverse plane as the plane formed by the ***x*** and ***y*** axes.

2.5 Resonance of total Magnetization with the RF pulse

Our goal is to somehow measure the overall macroscopic magnetization of the cores, so that we get information about the microscopic structure of the sample for display. The total *magnetization (M)* is in the order of μT (microTesla) when B_0, as a vector, is in equilibrium with M, which is measured in T (Tesla). It is generally difficult to measure the value of M, when it is in the same direction as B_0. Utilizing *RF* radio pulses, it is feasible to measure M it has to be deviated it from the direction of B_0,

The radiofrequency pulse is a cyclic polarized electromagnetic wave that contains a rotating magnetic field B_1. The B_1 magnetic field is perpendicular to B_0. To succeed in diverting the magnetization, the rotation frequency of B_1 (RF pulse frequency) must be equal to the precessional Larmor frequency of the isochromatic, so that we have *magnetic resonance*. On the rotating coordinate system, B_1 will appear stationary and aligned with the x 'axis. The vector M of the

magnetization will execute a precessional motion around B_1. The sum of these two precessions around the magnetic fields B_0 and B_1 results in the removal of magnetism M from the ***z*** axis to ***x'y'***.

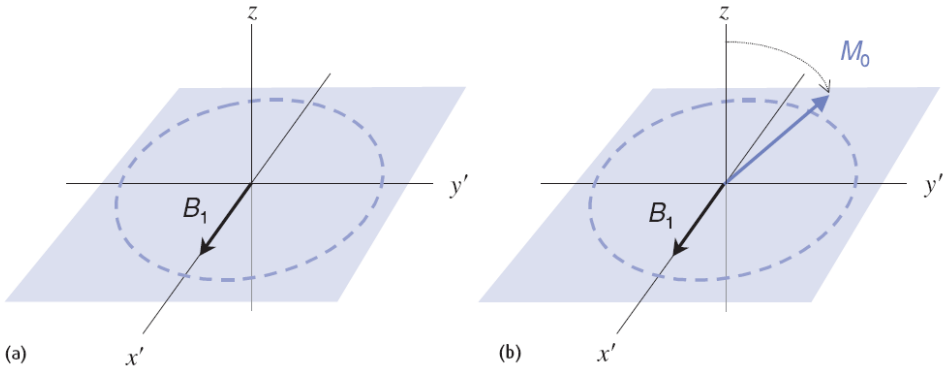

Image 2.13 **α.** $\boldsymbol{B_1}$ at the rotating coordinate system. **β.** The precession of $\boldsymbol{M_0}$ around $\boldsymbol{B_1}$ at the rotating coordinate system.

At the fixed (*xyz*) level, the *magnetization (M)* will perform a spiral motion, as shown below.

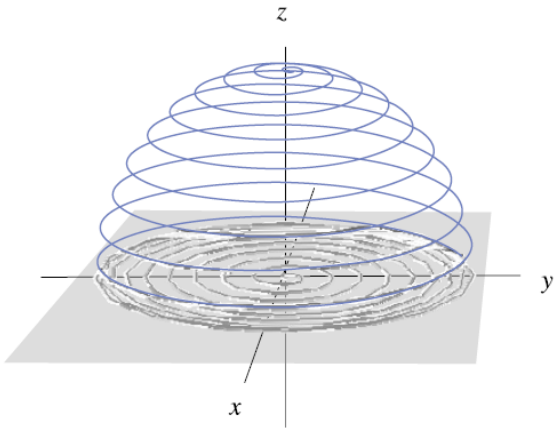

Image 2.14 The spiral motion of M at the stationary reference frame.

The final movement of the vector **M** is called *nutation*, as mentioned above. The *nutation* will be performed for as long as the pulse is applied. The angle of nutation is given by the relation:

$$\alpha = \gamma \cdot \mathrm{B_1} \cdot \mathrm{t_p} \quad (3),$$

, where $\mathrm{B_1}$is the intensity of the magnetic field of the *RF* pulse and $\mathrm{t_p}$ is the duration of its application. From the relation above, we can assume that we can cause the deflection of magnetization at different angles depending on the intensity and the duration of the RF pulse that we will apply.

At a microscopic level, the application of the *RF* pulse results in a decrease in the population of nuclei at low energy levels, while simultaneously the increase of the population of nuclei at high energy levels. In other words, macroscopically, the *total magnetization* will be reduced

and specifically for an *RF* pulse suitable to cause 90° nutation, the *longitudinal magnetization* will be zero. Respectively, if we apply a 180° *RF* pulse it will cause a reversal of the magnetization.

Another consequence of exposure to the RF pulse is that the isochromatics begin to move around the Bo in phase with each other, in other words they obtain phase coherence. At macroscopic scale, this implies the appearance of magnetism at the transverse plane. Thus, we can analyze *M* in two components, the longitudinal magnetization *Mz* parallel to the z axis and the Transverse magnetization *Mxy* on the *xy* plane.

Transverse magnetization (M_{xy}) works like a rotating magnet (Figure 15.a). With the use of a coil, therefore, we can produce an electrical voltage due to induction. The relation between *voltage* and *time* gives us the MR signal. This signal is called *Free Induction Decay /F.I.D.* Therefore, the greater the intensity and duration of the *transverse* magnetization component, the more intense the magnetic resonance signal will be.

The *Longitudinal* component ($M_{z)}$ has no contribution in the measured *MR signal,* since it remains in the same direction as B_o, essentially non-measurable. The *FID signal*, in fact, attenuates at a high speed, since after excitation from the RF deflection pulse, new mechanisms are used to restore the system back to equilibrium and minimum energy. It is important to remember that energy must always be conserved.

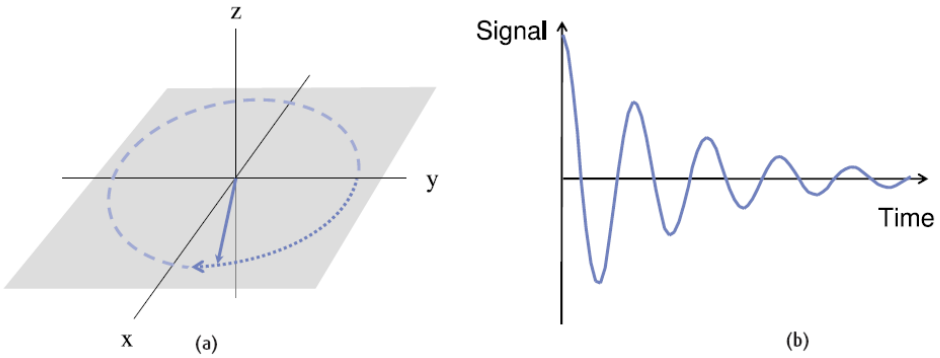

Image 2.15 a. Transverse magnetization after the RF pulse **b.** FID signal.

2.6 Magnetic Relaxation: What happens when the Radiofrequency pulse is shut off?

When the RF pulse application stops then the whole system, which had been disturbed, returns to its original state. The *Transverse Magnetization* begins to decrease, while *Longitudinal Magnetization* increases. The two phenomenons are called *Transverse Magnetic Relaxation* (M_{xy}) and *Longitudinal Magnetic Relaxation* (M_z).[13]

2.6.1 Longitudinal Magnetic Relaxation

The Longitudinal Magnetic Relaxation is described by the exponential increase of the longitudinal component of the magnetization M_z, given by the relation:

$$Mz(t) = Mz(0)(1 - e^{\frac{-t}{T1}}) \quad (4)$$

, where $M_z(t)$ is the longitudinal magnetization at time t, $M_z(0)$ is the initial longitudinal magnetization, t represents the time from pulse pausing, and T1 is the time constant expressing the time required to recover 63% of the original longitudinal magnetization, immediately after its interaction with a radio frequency (*RF*) pulse of 90^0. The following Figure-Diagram showing the process of *T1* relaxation after a 90° rf pulse is applied at equilibrium.

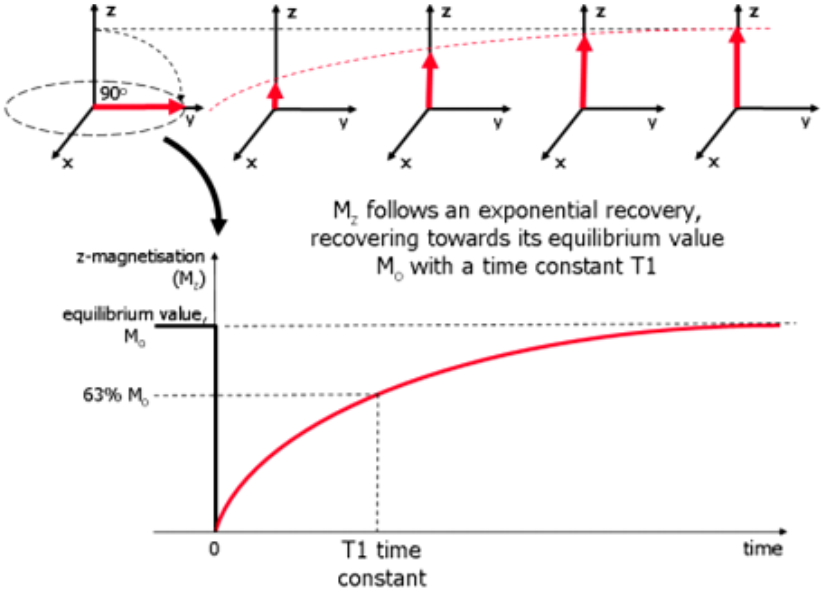

Figure 2.16 The Longitudinal Magnetic Relaxation T1. [11]

The *T1 relaxation time* is dependent on the external magnetic field B_0 and is smaller in stronger fields. The temperature dependence is also measurable. It actually represents a time constant for regrowth of the Longitudinal Magnetization (M_z) *after RF pulse.* The *relaxation rate* is defined as the inverse of *T1*, i.e. *1 / T1*. The *relaxation rate* corresponding to *T1* is typically designated by the symbol *R1*, where:

$$R1 = 1/T1 \quad (5)$$

With all the above said, *Longitudinal Magnetic relaxation* is due to the interaction of magnetic spins with the atoms of the nearby lattice where the energy obtained by the system from the application of the RF pulse is attributed.

Energy must therefore leave the spin system for *T1 relaxation* to occur. This energy loss is unrecoverable and represents the transfer of heat. At the most basic level, therefore, T1-relaxation is

simply an energy flow between spins and their external environment. The amount of energy transferred from the nuclei is very small compared to normal molecular kinetic energies, so it is quickly dispersed and goes largely unnoticed at body temperatures.

T1 relaxation time is typically measured in milliseconds (ms). The corresponding relaxation rate is therefore measured in units of [1/ms].

2.6.2 Transverse Magnetic Relaxation

The decay of transverse magnetization (M_{xy}) is a result of the loss of phase coherence between the protons after the cessation of the RF pulse. Transverse magnetic relaxation is described by the exponential reduction of the transverse component (M_{xy}) of magnetization, given by the relation:

$$Mxy(t) = Mxy(0)e^{\frac{-t}{T2}} \quad (6)$$

,where $M_{xy}(t)$ is the transverse magnetization in time *t,* M_{xy} (0) the transverse magnetization immediately after the cessation of RF pulse and T2 the time constant expressing the time required for the loss of 37% of the initial transverse magnetization immediately after its interaction with a 90^0 RF pulse.

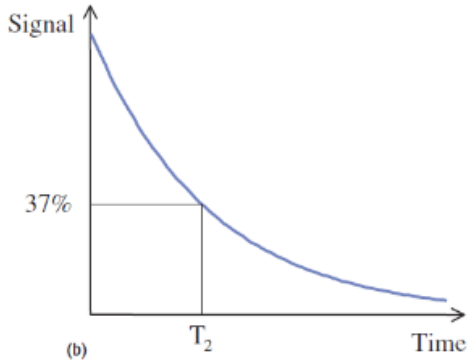

Figure 2.17 The Transverse Magnetic Relaxation.[2]

T2 relaxation time is independent of the B_o magnetic field in which it is measured, but is dependent on the measurable temperature. The rate of transverse magnetic recovery is equal to:

$$R2 = 1/T2 \qquad (7)$$

The reduction of transverse magnetization is the result of the loss of phase coherence between the protons within the isochromatic and after the cessation of the RF pulse. The loss of phase coherence is due to strong bipolar interactions between the nuclei within the isochromatic group of spins.

Internal inhomogeneities are created due to the interaction between protons as they move in the tissues. Actually, if two protons approach each other, then the magnetic field they are experiencing will increase or decrease due to the interaction, resulting to the changes in precessional frequency to slightly greater or smaller from that of the neighboring protons.

Specifically, T2 relaxation is related to the amount of *spin-spin interaction* that takes place. Free water contains small molecules that are relatively far apart and moving rapidly and therefore *spin-spin interactions* are less frequent and *T2 relaxation* is *slow* (*leading to long T2 relaxation times*). Water molecules bound to large molecules are slowed down and more likely in interact, leading to faster *T2 relaxation* and *shorter T2 relaxation times*. Water- based tissues with a high macromolecular content (e.g. muscle) tend to have shorter T2 values. Conversely, when the water content is increased, for example by an inflammatory process, the *T2* value also increases.

Lipid molecules are of an intermediate size and there are interactions between the hydrogen nuclei on the long carbon chains (an effect known as *J-coupling*) that cause a reduction of the *T2 relaxation time constant* to an intermediate value. Rapidly repeated *RF* pulses, such as those used in turbo or fast spin echo techniques, can have the effect of reducing J-coupling, resulting in an increased *T2 relaxation time* and higher signal intensity from fat.

When the two interacting protons are removed, then their precessional frequency will return to the original value, but the phase difference created during the interaction is irreversible. The homogeneous external magnetic field actually has small differences in the value of its intensity, with the result that this small inhomogeneity causes an additional loss of phase coherence, which is not due to the actual phenomenon. We characterize this process as pseudo-recovery with time constant *T2inh*. Consequently, magnetic relaxation is due to natural processes but also to *pseudo-processes*, and is generally characterized by the time constant *T2**.

In any real *NMR* experiment, however, the transverse magnetization decays much faster than would be predicted by natural atomic and molecular mechanisms. This rate is denoted as *T2* ("T2-star"*). *T2** can be considered an "observed" or "effective" T2, whereas the first *T2* can be considered the "natural" or "true" T2 of the tissue being imaged. T2* is always less than or equal to *T2*.

The final relaxation rate of T2* is given by the sum of the individual rates and is expressed by the following relation:

$$\frac{1}{T2^*} = \frac{1}{T2} + \frac{1}{T2inh} \quad (8)$$

, where *T2inh* is the *inhomogeneous spin relaxation time*. From the relation above it turns out that the time constant *T2** is always smaller than *T2*.

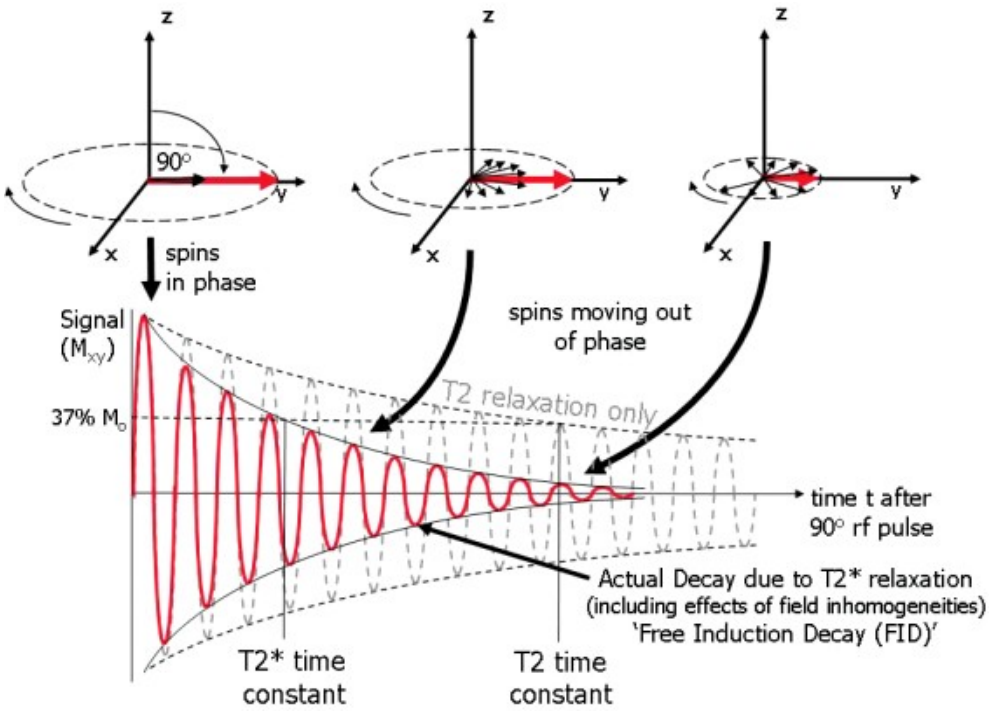

Figure 2.18 A comparison of T2 decay and the more rapid T2* decay arising mainly from the magnet inhomogeneity.[11]

Longitudinal and Transverse magnetic relaxation are two independent phenomenons that occur simultaneously but their duration is very different. The loss of phase coherence of the proton occurs very rapidly and therefore transverse magnetization is rapidly zeroed within a few hundred milliseconds (*ms)*. Longitudinal magnetic relaxation is much slower (*sec*), (*Figure 2.19*). In biological tissues, T1 is about five times longer that of T2.

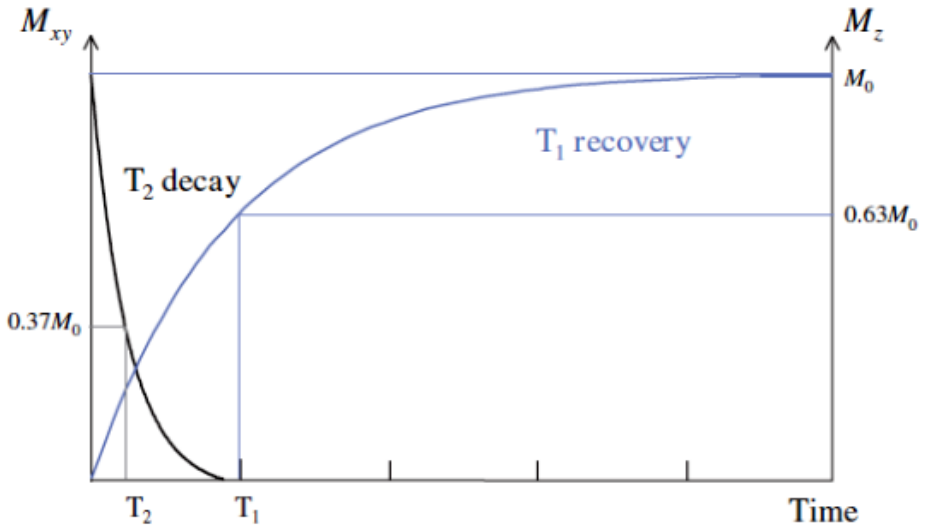

Figure 2.19 Simultaneous appearance of T1 and T2 relaxations. T2 is much faster than T1.

2.7 MR Pulse Sequences

Each MR sequence is a combination of *RF pulses* and *gradient fields*. In every type of sequence, the goal is to display an area as fast as possible with the highest contrast as possible between the different tissues. Alongside, having a reduction of artifacts and keeping the Signal to Noise ratio (SNR) in high levels. We will now "put it all together" and view the chain of events required to produce an MR image in its entirety.

The execution of a pulse sequence is much like a symphony. In an orchestra, each instrument must turn on at the correct note (frequency) and volume (amplitude) at the correct time and of course, become silent at exactly the right time. In the MR pulse sequence, the time-varying magnetic fields (radiofrequency and gradient) and receiver are the instruments. Each is activated at a specific frequency and amplitude for a specific period of time. The epochs during which the time varying magnetic fields are on are termed pulses. The sequence, of course, is the order in which the various pulses occur. So with all the above said, we have a *pulse sequence*.

So, the architecture of a sequence consists of basic and necessary structural elements, but also of many parameters that can be differentiated. The basic parameters set by the user are:

- ***TR***: the time between two successive pulses (*Repetition Time*)
- ***TE***: the time elapsed from 90^0 pulse to *Echo Time*
- ***TI***: the time between the 180^0 pulse and the depletion of the longitudinal component of magnetization. (*Inversion Time*)

While there are many more parameters in some sequences such as the *flip angle*, or the *turbo factor* which we will not analyze in this work.

When considering the values of the variable parameters, the user can choose the effect on the image contrast by modifying the *magnetic recovery times* (*T1*, *T2*, *T2** or the *ADC diffusion coefficient* of the displayed object/tissue). The user will also need to set the parameters in a way, so that he has the optimal combination of *contrast*, *resolution* and *speed* for *image acquisition*.

2.7.1 Types of MRI Sequences

There are hundreds of sequences for MRI with different names, depending on their development from each company. We will describe the characteristics of the main family sequences and we will mention the most important ones.

There are *two* main *sequence families*, depending on the *type* of *echo* recorded:

1. ***Spin Echo sequences (SE)***, characterized by the presence of a 180° rephasing *RF* pulse
2. ***Gradient Echo sequences (GE)***

Numerous variations have been developed within each of these families, mainly to increase acquisition speed:

- *Fast Spin Echo* sequences, *Single Shot* FSE and *Haste*
- *Gradient echo* sequences with spoiling of residual transverse magnetization (spoiled gradient echo and *ultrafast gradient echo*), a group of gradient echo sequences with steady state residual transverse magnetization (Steady state gradient echo) and its derivatives (Contrast enhanced steady state gradient echo) and with balanced gradients (Balanced steady state gradient echo), echoplanar (EPI).

Some sequences are hybrid, mixing *Spin Echo* and *Gradient Echo* (GRASE, SE-EPI).

Based on these *two fundamental methods*, all the sequences that exist are based on the two sequence families and appear in the following map with the contrasting characteristics of the images they produce.

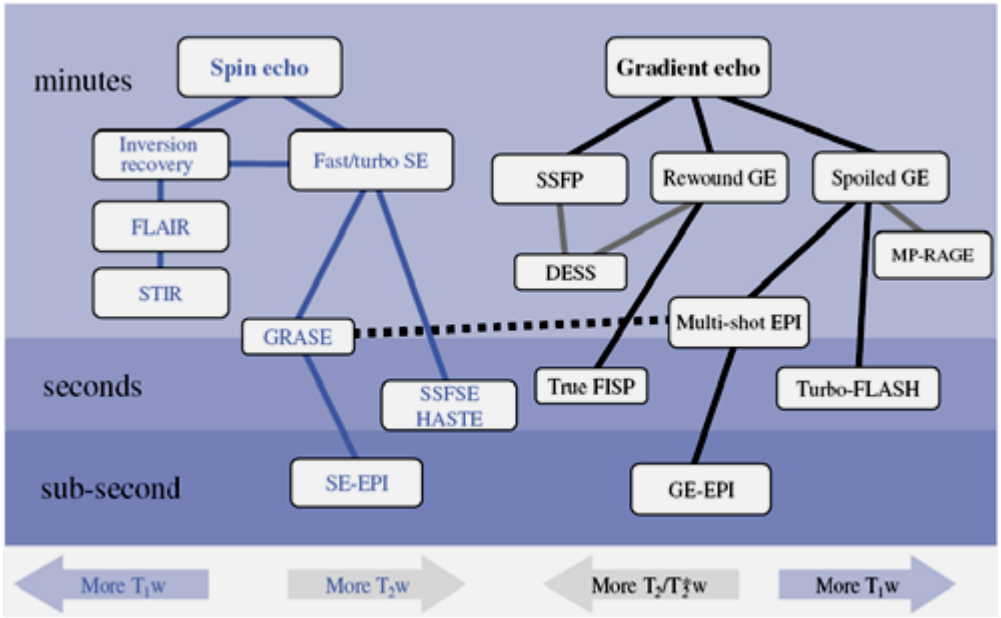

Figure 2.20 Sequence's tree.

In the following chapters we will describe in more detail the sequences that were used in the experiments, to fully understand how they work, and the choice of the optimal values of their parameters.

3. Magnetic Resonance Imaging System

The magnetic resonance imaging system is a complex and usually an expensive structure that requires high technology know-how. To understand how it works, we will analyze it in four main parts:

1. The powerful *Magnet,*
2. the *Gradient Coils*,
3. the *Radio Frequency Receivers (RF coils)* and
4. the *Computer Unit*.

3.1 The powerful Magnet

As we saw in the previous chapter, in order to achieve the phenomenon of nuclear magnetic resonance (NMR), it is necessary to place the sample in a 'large' homogeneous static magnetic field. The larger the magnetic field of the system, the higher the signal we will receive from our sample, compared to the noise (SNR). The more homogeneous the field, the smaller the errors for the necessary calculations for the display.

When medical professionals refer to magnetic resonance (MR) scanners, they sometimes say the scanner is a 1.5T or 3.0T scanner. This is because scanners are frequently identified by their *magnetic field strength*. In terms of MR, T stands for Tesla, a unit of measurement to define the *magnetic flux density*. One Tesla is equal to 10,000 Gauss. It is named after Nikola Tesla (*1856-1943*), the Croatian-American physicist, inventor and electrical engineer. [2]

With higher Tesla scanners, the magnet is stronger, both in general and within the bore of the machine. The magnet and its magnetic field is arguably the most important aspect of an MRI scanner. Typical values of the 'large' magnetic field strength in imaging systems are from 0.2T to 7T, with the most common values: *1.5T* and *3T*. For more sophisticated applications, mainly in research, 10T or larger magnetic fields are also used. There are three types of magnets that can create such fields:

• *Permanent magnets*, which are relatively inexpensive and maintenance, but are very heavy constructions and have relatively low values of intensity of their generated field.

• *Electromagnets*, which are relatively cheap, but require a high energy consumption and cooling and ultimately fail to achieve high voltage values.

• *Superconductive electromagnets*, which are the most common choice for an imaging system. They are more expensive than the other two types of magnets, because in order to achieve superconductivity, the coil is placed in a liquid Helium (He) tank which is in a Helium gas or liquid Nitrogen tank itself. To maintain them, these systems require constant monitoring and filling of the Helium tank at regular intervals. But the result of this cost and this process is a very strong and homogeneous magnetic field.

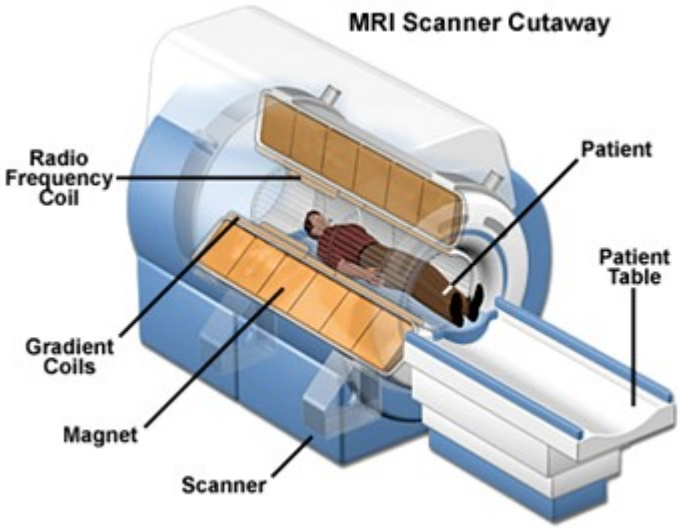

Figure 3.1 MRI tomography system.[15]

3.2 The Gradient Coils

These coils are placed around the volume of the large magnetic field (image). They create magnetic fields of the same direction as $\boldsymbol{B_0}$, but of linearly changing intensity in one dimension in space. Their magnetic field is added to $\boldsymbol{B_0}$ so that the total field shows an escalation in the value of its intensity with respect to one dimension. We have different gradient coils for the three dimensions, *x, y* and *z*, which cause the field intensity to escalate in their nominal direction. We will analyze their use in the next chapter as it lies in the choice of the imaging section, and in the spatial coding of the signal. The characteristics of gradient coils are:

- The maximum change they cause in the magnitude of the magnetic field per unit length is measured in mT/m and determines the maximum spatial resolution of the system.

- The slew rate, which expresses the time it takes to achieve the escalation in $\boldsymbol{B_0}$. It is measured in mT/m/ms. High rising rates and short switching times of the gradients are necessary for imaging using high-speed sequences (EPIs).

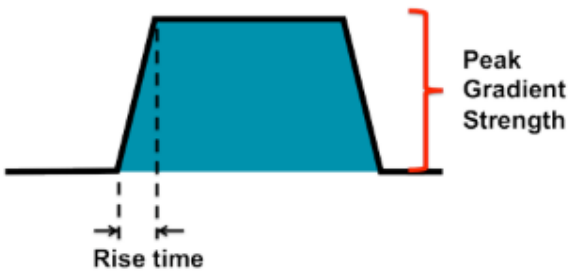

Figure 3.2 Slew rate is defined as Peak gradient strength ÷ Rise Time

- Their linearity, which should be as perfect as possible throughout the display space.

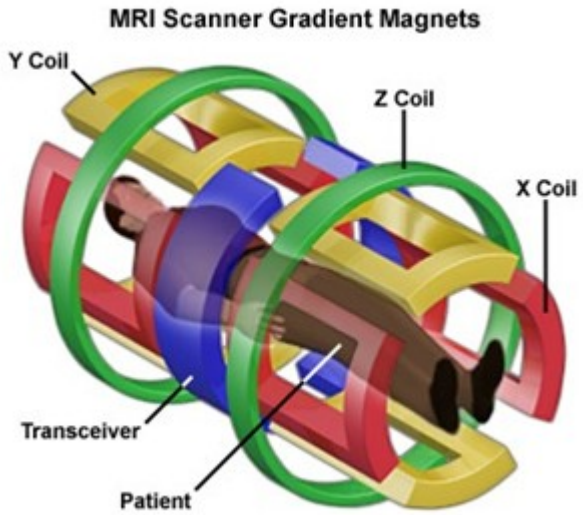

Figure 3.3 The Gradient Coils[15].

3.3 The Radio Frequency Receivers (RF coils)

Radiofrequency coils (RF coils) are the "antennae" of the MRI system, broadcasting the *RF* signal to the patient and/or receiving the return signal. RF coils can be receive-only, in which case the body coil is used as a transmitter, or transmit and receive (transceiver).

RF coils as transmitters should emit a uniform RF pulse throughout the volume for display, while as receivers they should be quite sensitive and have a high signal-to-noise ratio (SNR). For optimal signal reception in each case we use different types of coils: *volume* coils, *surface* coils, *quarter-coil* coils, *tubular* and *Phased-array* coils. Depending on the case, there are types that are superior to others. Because proton resonance frequencies are so close to those of FM and television, the entire imaging system is housed in a Faraday cage so that it is completely electromagnetically isolated and protected from any external interference.

3.4 The Computer Unit

All the electronic systems reported in the previous sections work in complex combinations, in order to achieve resonance, to receive the signal as well as the reconstruction of the final image. In accordance, a good computing power unit with data storage space and ergonomic control console with appropriate software systems is required.

4. Introduction to Spatial Encoding

In order to get from the NMR phenomenon to imaging, the system performs quite complex processes. The image reconstruction technique used by all manufacturers is that of the two-dimensional (2D) *Fourier transform* (spin warp technique), which replaced the reverse projection technique, which was initially applied but lags behind in speed. We will analyze the steps separately in their simplest form, so that we understand how to produce the image in an MR imaging system. For imaging it is necessary to add spatial data to the signal to allocate a position to the different signals.

To do so, we start by selecting the slice plane, within which the horizontal and vertical directions will then be defined. The term « encoding » is used, as the spatial data obtained are not the classic co-ordinates (x, y, z), but are observed through a specific spatial filter. The RF signals received are then processed to reverse the filter effect and reconstruct the image. Decoding of spatial information, included in the NMR signal as modifications of frequency and phase, is performed by an inverse Fourier Transform.

4.1 Magnetic field Gradients in Spatial Encoding

Spatial encoding relies on successively applying magnetic field gradients. First of all, a slice selection gradient (GSS) is used to select the anatomical volume of interest. Within this volume, the position of each point will be encoded vertically and horizontally by applying a phase encoding gradient (GPE), and a frequency-encoding gradient (GFE).

The different gradients used to perform spatial localization have identical properties but are applied at distinct moments and in different directions. Gradient equivalence in the three directions of space means that slices can be selected on any spatial plane. We'll use the example of an axial plane to explain spatial encoding.

4.2 Selecting the Slice Plane

The first step of spatial encoding consists in selecting the slice plane. To do this, a magnetic field gradient, the *Slice Selection Gradient* (*GSS*), is applied perpendicular to the desired slice plane. This is added to B_0, and the protons present a resonance frequency variation proportionate to *GSS* (*Larmor equation*). An *RF* wave is simultaneously applied, with the same frequency as that of the protons in the desired slice plane. This causes a shift in the magnetization of only the protons on this plane. As none of the hydrogen nuclei located outside the slice plane are excited, they will not emit a signal. The *RF* wave associated with the slice selection gradient and the adapted resonance frequency is called the *selective pulse*.

Since the gradient function changes the intensity of the magnetic field B_0 of the magnet *linearly*, the magnetizations of the nuclei within the specific positions of the selected section along the slope will be characterized by a unique precessional frequency when the gradient will be in operation (turned on). A section can therefore be selectively stimulated by the transmission of the RF signal at the specified precessional frequency.

Thus, more specifically the *gradient* ***Z*** selects the transverse cross-sections, so that the magnetizations of the spin cores on the patient's head rotate at a different frequency than those at his legs. *Gradient* ***Y*** selects the *coronal* slices, so that the magnetizations of the spin cores in the back of the patient are at a different frequency than those in the front. Finally, the *gradient* ***X*** selects the *sagittal* slices, so that the magnetizations of the nuclei spins on the right side of the patient rotate at a different frequency than those on the left, while a combination of two of any gradient selects oblique sections.

In order to achieve the thickness in one section, a frequency range must be transmitted to stimulate all the core spin which are located at different points in the plane. This frequency band is called *Transmit Bandwidth*.

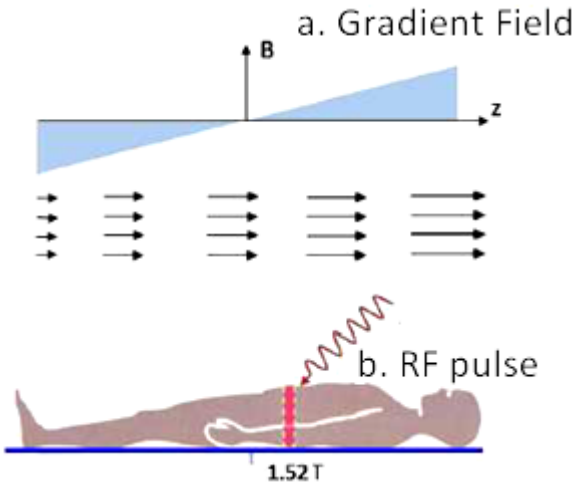

Figure 4.1 Transverse slice selection.[15]

More specifically, the slice thickness is determined by the slope of the corresponding *gradient field* and the broadcast bandwidth (*Figure 4.2*). On the contrary, the thicker slices require a slight inclination in the *Gradient field* and a large *Bandwidth*, while their use helps to reduce the *spatial resolution* of the image.

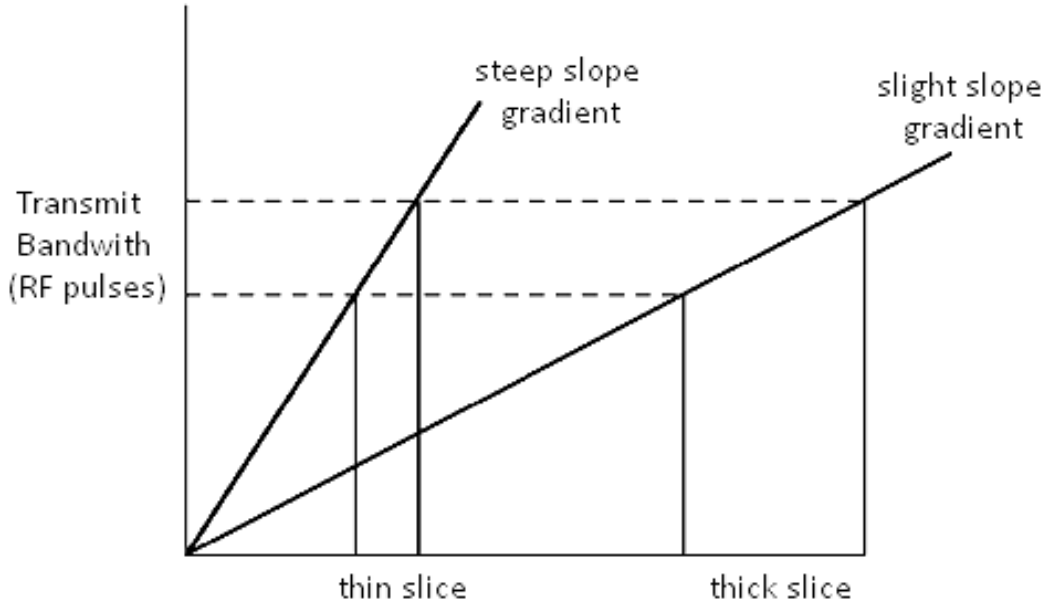

Figure 4.2 Slice thickness according to the Gradient field slope.

A slice is therefore stimulated by the transmission of an RF pulse with a central frequency that will excite the midpoint of the slice, while the points (on both sides left and right) will be excited by frequencies through the *transmit bandwidth* and the thickness of the slice will determine the inclination of the gradient field slope. The gap between the slices is also determined by the gradient inclination and the thickness of the slice. The size of the gap is important for reducing the pseudo-indications in the image.

The gradient used for the section selection remains activated during the excitation of the cores by the RF pulse. After selecting a slice for imaging, the intensity of the magnetic field of the nuclei within the excited intersection is equal to the intensity of the field of the system. The precessional frequencies of the spins in the slice are equal to the Larmor frequency. The frequency of each signal from the slice is also equal to the Larmor frequency, regardless of the position of each signal.

The system must also use *gradients* to provide the two-dimensional (2D) information that represents the spatial position of the spin rotations within the section. When a gradient is activated, the precessional frequency of a core is determined by its physical position within the gradient.

4.2.1 Phase Encoding (PE)

The second step in spatial encoding consists in applying a phase encoding gradient, which we will choose to apply in the vertical direction. The *phase encoding gradient (GPE)* intervenes for a limited time period. While it is applied, it modifies the spin resonance frequencies, inducing dephasing, which persists after the gradient is interrupted. This results in all the protons precessing in

the same frequency but in different phases (the protons in the same row, perpendicular to the gradient direction, will all have the same phase). This phase difference lasts until the signal is recorded.

The signal in this process must be located along the small axis of anatomy. This signal localization is called *Phase Encoding* (*PE*). When the *phase encoding gradient* (*PEG*) is activated, the intensity of the magnetic field and therefore the precessional frequency of the core are modified along the gradient axis. As the speed precession of the nucleus changes, so does the accumulated phase in the magnetic moments along it.

The nuclei that have been accelerated due to the presence of the gradient. They move faster and forward towards their transition path than if the gradient had not been applied. The nuclei that have slowed down due to the presence of the gradient move slightly backwards around their transition path, than if gradient had not been applied

In particular, the magnetizations of the spin cores that receive a higher magnetic field intensity, when the gradient is activated, will precede the magnetizations that do not receive any stimulation. This is because when a spin precesses to a higher frequency it rotates faster and thus covers more perimeter motion than if the gradient was not applied. In the opposite case now, where the spins of the cores receive lower magnetic field intensity, the vector of the core's inversion is delayed in its orbit and thus "falls short" of phase.

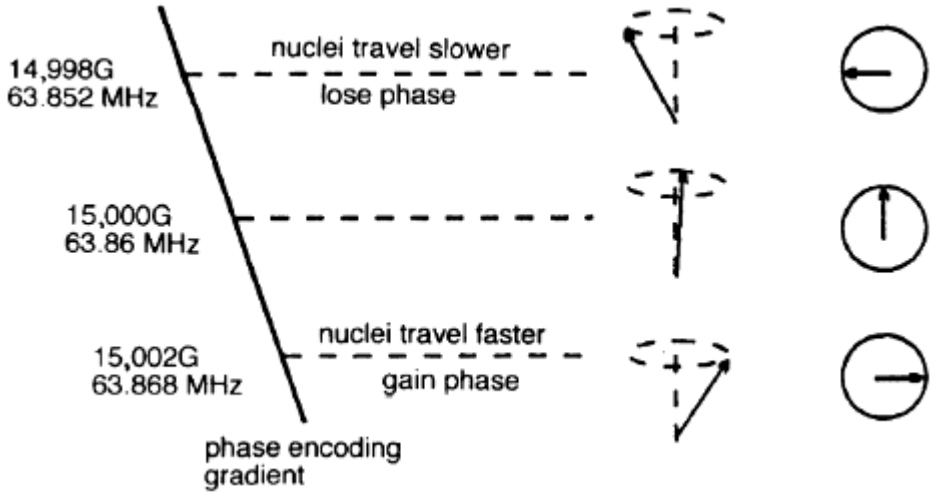

Figure 4.3 Phase Encoding.[6]

The level of displacement of phase of a spin compared to the phase of a non-excited spin has to do with its distance from the initial point, defined as the *isocenter*, where the gradient there has *zero value*.

To locate the signal along the *smallest dimension of the anatomy* of the image, a *Phase Encoding field* is applied. This additional field causes a phase shift in all the spins along its slope.

- When the phase coding field is off, the cores return to the Larmor frequency but their phase shift remains, i.e. everything moves at the same angular velocity, but their positions on the perimeter are different. This phase shift is used to locate the cores (and therefore the signal) spatially along one dimension of the image.
- The inclination or width of the phase coding field determines the degree of phase shift (*Figure 4.4*). Phase coding fields with larger inclinations produce a larger phase shift between two points than smaller inclinations. They also increase image resolution along the phase coding axis

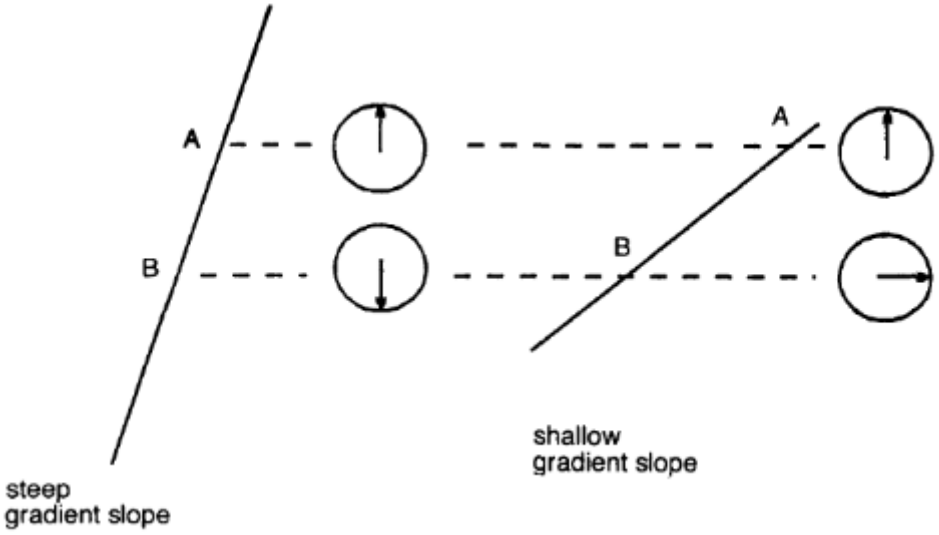

Figure 4.4 Phase shift depending on the inclination of the Phase Encoding Gradient (GPE).

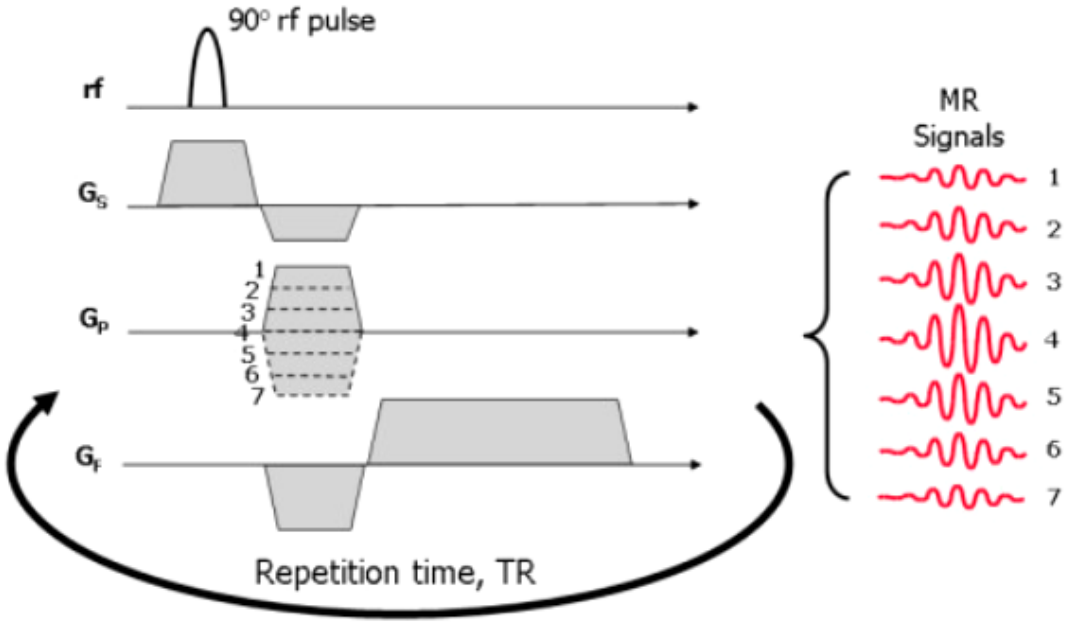

Figure 4.5 Phase encoding steps and repetition time, TR. [11]

To acquire sufficient information for image reconstruction, the pulse sequence is repeated a number of times, with an increment in the strength (or slope) of the *phase encoding gradient* being applied each time. In this example shown above *(Figure 4.5)*, 7 values of *Phase Encoding gradient slope* are used (shown by the dotted lines). Note that as the *strength* of the *Phase Encoding gradient* increases, this increases the amount of de-phasing along the *gradient*. When the strength (or slope) of the phase encoding gradient is zero (step 4), there is no de-phasing and the signal has its maximum possible amplitude. The time interval between each repetition is known as the *repetition time, TR.*

The coil generated by the *Phase Encoding Field* is activated after the *RF* excitation pulse is *switched off*. It usually *stays on* for *4 ms,* while the width and polarity of the coil alternate at each step of the *Phase Encoding process*.

4.2.2 Frequency Encoding

The final step in spatial encoding consists in applying a Frequency Encoding Gradient, when the signal is received. This modifies the Larmor frequencies in the horizontal direction throughout the time it is applied. It thus creates proton columns, which all have an identical Larmor frequency. As this gradient is applied simultaneously on receiving the signal, the frequency data is included.

A *Gradient* corresponding to the large axis, of the image to be produced, is applied so that the *MR signal* is located along it. Frequency shifting occurs due to this field, which is used for signal localization. It produces a shift in the angular frequency of the elementary magnets, depending on the position of the cores. The field and therefore the frequency increase gradually from the center to one end of the application axis and decreases gradually to the other end. Thus, it maps each frequency and produces a spatial classification. This process is called *Frequency Encoding*.

The *frequency encoding field* is applied for a very short time, usually a few milliseconds, while receiving MR signals. Frequency encoding is done simultaneously, across the gradient application axis, with the counted *MR* signals. Finally, the size of the field inclination determines the size of the large axis of the image that is to be produced and the size of the anatomy projection field, which affects the resolution of the final image. So, it determines the size of the anatomy covered along the frequency encoding axes during the scanning procedure. This is called the *Field of View (FOV)*.

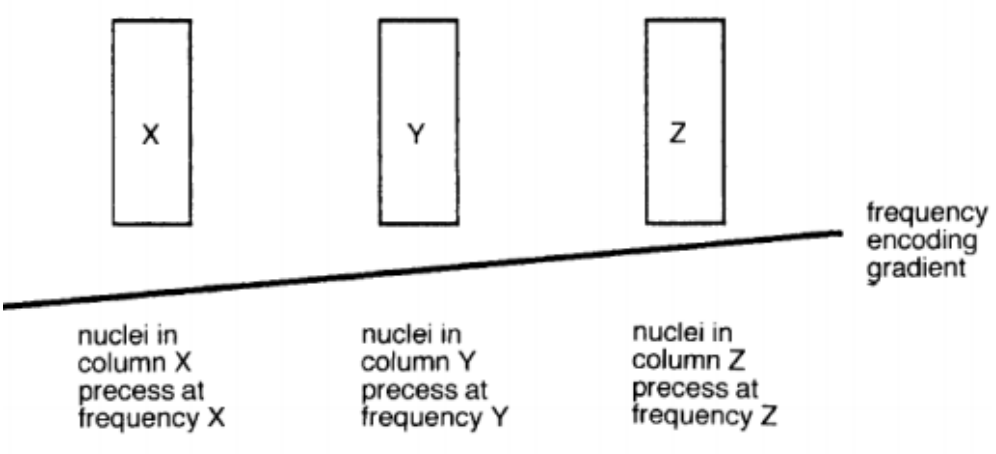

Figure 4.6 Frequency Encoding.[13]

Table 1. Gradient inclination axes at a rectangular plane.

	Slice selection	Phase encoding	Frequency encoding
Sagittal	X	Y	Z
Axial (body)	Z	Y	X
Axial (head)	Z	X	Y
Coronal	Y	X	Z

4.3 K-space

Spatial encoding selects an individual slice and produces a frequency shift of magnetic moments of spins along one axis of the slice and a phase shift along the other as we have seen previously. The system now has a way of locating an individual signal within the image by measuring the number of times the magnetic moments of spins cross the receiver coil (frequency) and their position around their precessional path (phase).

The phase shift caused by the phase-encoding gradient creates a spatial frequency. This is because a waveform is derived from plotting the change of phase of magnetic moments of hydrogen nuclei located at different locations along the gradient. Spatial frequencies are also obtained from slice-selection and frequency encoding because they too cause frequencies that are dependent on spatial position. Data from these spatial frequencies are used by *Fast Fourier Transform (FFT)* mathematics to produce an image.

During the scan, data are acquired and stored in k-space. K-Space is a spatial frequency domain, where information about the frequency and spatial origin (from which point of the patient's anatomy is produced) of a signal is collected and stored.

«*K*» denotes spatial frequency (strictly speaking it refers to the angular wavenumber, which is a function of spatial frequency and wavelength, but for our purposes it's acceptable to just use the term spatial frequency). Therefore, *K-Space* is a storage space for spatial frequencies. The units of k-space are *rad/m (or cm)*. This is because spatial frequency is represented as a phase change over distance along a gradient.

The units of phase are *radians* (units of degrees in a circle) and the units of distance are *m* (or *cm*). This is different from the standard unit of frequency, *rad/s* or *Hz*. These units are appropriate when looking at the magnetic moment of a single spin because, in that context, the phase change of the magnetic moment is measured as it precesses over time. Spatial frequency is different because it measures the *change of phase* between the magnetic moments of a row of spins along the gradient.[11]

K space does not have a spatial correspondence analogy of ***1: 1*** with the image that will eventually be produced by the MRI, so the peak of the K space does not correspond to the peak of the produced image. K space is simply an "intermediate" area where data is stored until scanning is complete. A schematic representation of K space is shown below.

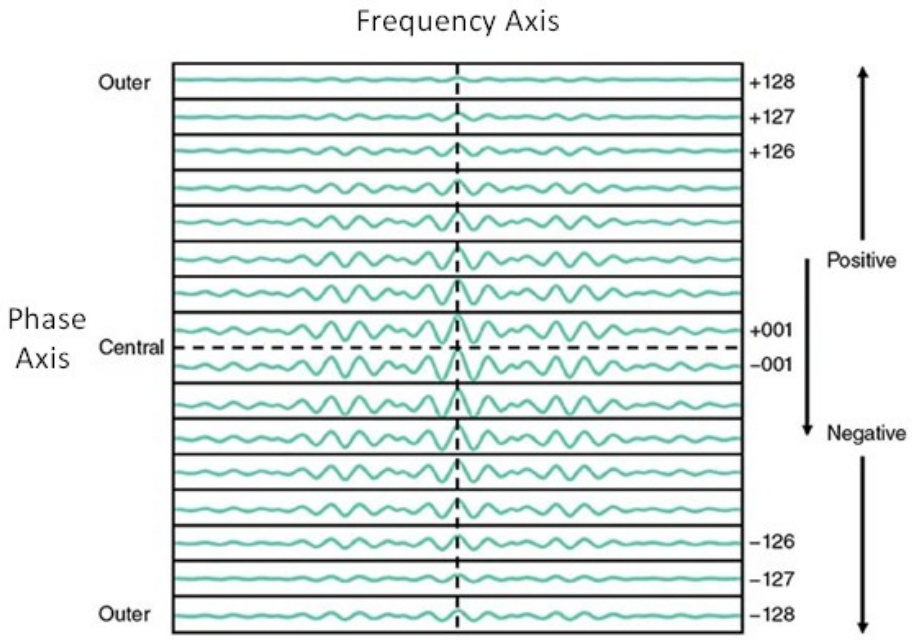

Figure 4.7 K-space.

Figure 4.7 illustrates k-space for one slice. *K-Space* is rectangular and has two axes perpendicular to each other. The *frequency axis* of k-space is horizontal and is centered in the middle of several horizontal lines. Data from frequency encoding are positioned in k-space along this axis. The phase axis of k-space is vertical and is centered in the middle of k-space perpendicular to the frequency axis. Data from phase encoding are positioned in k-space along this axis. In the simplest

method of k-space filling, data are stored in horizontal lines that are parallel to the frequency axis and perpendicular to the phase axis of k-space, the number of which corresponds to the number of phase encodings performed during the scan.

Each time a frequency or phase encoding is performed, the data is collected and stored in a K-space line. The lines closest to the phase axis, both *positive* and *negative*, are called central lines. Lines that are away from the phase axis, both positive and negative, are called external lines. The upper half of the K space is characterized as *positive* while the lower half as *negative*.

The polarity of the *phase encoding coil* determines whether the *positive* or *negative* half of K-space will be filled. The part of the phase coding field with positive slopes fills out the lines in the positive half of K space, while the negative slopes fill out the lines in the negative half. The lines are numbered depending on their position from the central horizontal axis. Thus, the positive lines start from the upper half of the space, while the negative ones from the lower half. The lines of the K space are filled in a different way and at a different speed, depending on the sequence of pulses that we will use (from left to right or vice versa, from bottom to top or vice versa, linearly or spirally). Finally, the K-space is symmetrical to both axes. This is called *conjugate symmetry*, because the data on the right side of K-space are the same as those on the left, and the data at the top half are the same as those at the bottom half.

The *central lines* of the K-space are filled with data which are generated after the application of lateral field encoding coils of small slopes, while the outer lines of the K space are generated after the application of large phase encoding field slopes. Intermediate lines are obviously filled in by the application of phase encoding fields with intermediate gradient slope values.

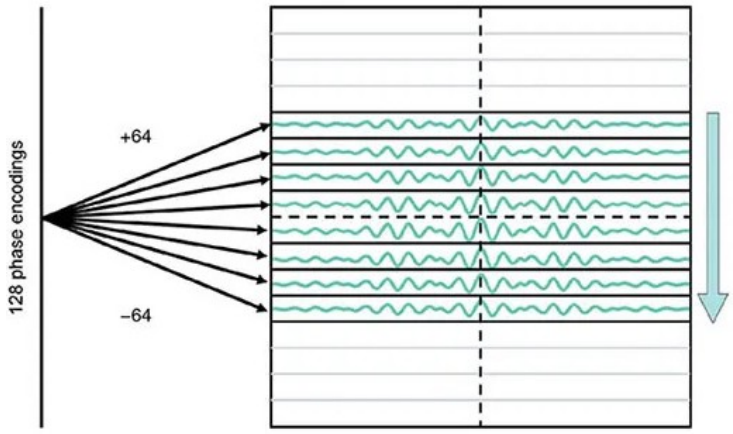

Figure 4.8 K-space- Application of different phase encoding gradient slopes.

Fields with a shallow gradient phase encoding slope do not cause a large *phase shift* along their axis. Therefore, the stimulation of magnetic moments with *RF* pulses or the adjustment by imposing a gradient field will be more effective (the displacements of the magnetic moments will be more uniform), since the inherent phase shift after phase encoding is small. The resulting signal will therefore be a large amplitude signal.

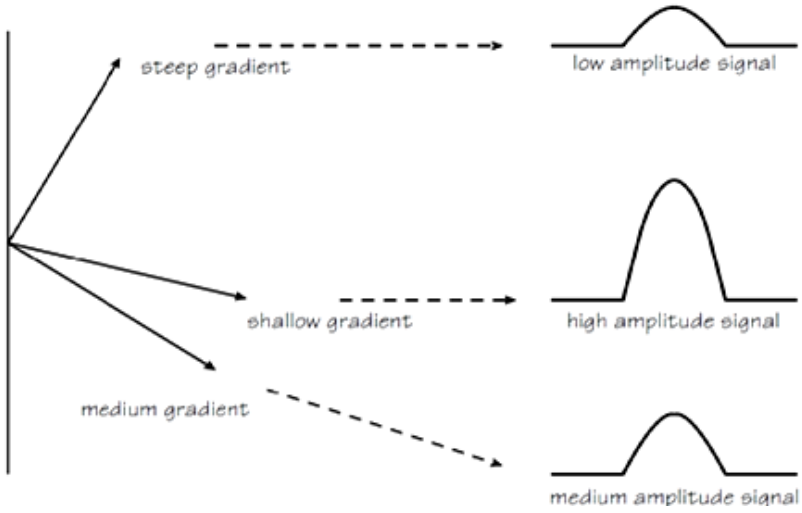

Figure 4.9 The produced signal, depending on the inclination of the phase encoding gradient.

In addition, fields with a steep phase encoding slope cause a large *phase shift* along their axis. Therefore, the excitation of magnetic moments with RF pulses will be ineffective (the displacements of the magnetic moments will be non-uniform), since the inherent phase shift after phase coding is big. The resulting signal will therefore be a small amplitude signal *(Figure 4.9)*.

The various frequencies contained in the MR signal are placed in K-space to the frequency axis. The center of the echo (reflection of MR signal) represents the maximum signal amplitude as all magnetic moments are in phase at this point. Elsewhere, besides the center, the magnetic moments have some phase difference between them and therefore the signal amplitude is less. The amplitude of the frequencies is therefore recorded in relation to the frequency axis, so that the center of the sound is centered on the frequency axis. The parts of the signal that correspond to *rephasing* and *dephasing* magnetizations are recorded on the left and right sides of the frequency axis, respectively (*Figure 4.10*).

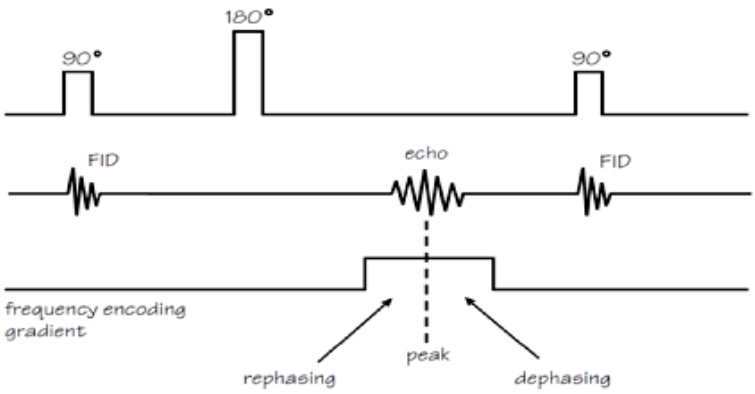

Figure 4.10 The signal amplitude during the application of the frequency encoding gradient.

When *K-space* is filled, after a series of pulses, an inverse two-dimensional Fourier transform is sufficient to obtain the final image from the MR signal. This transformation decodes the spatial origin of the signal from phase and frequency, and from the K-space (*frequency - phase*), leading to

the *2D image* (horizontal distance - vertical distance). We must remind at this point that *K-space* has not a one to one space to image correspondence.

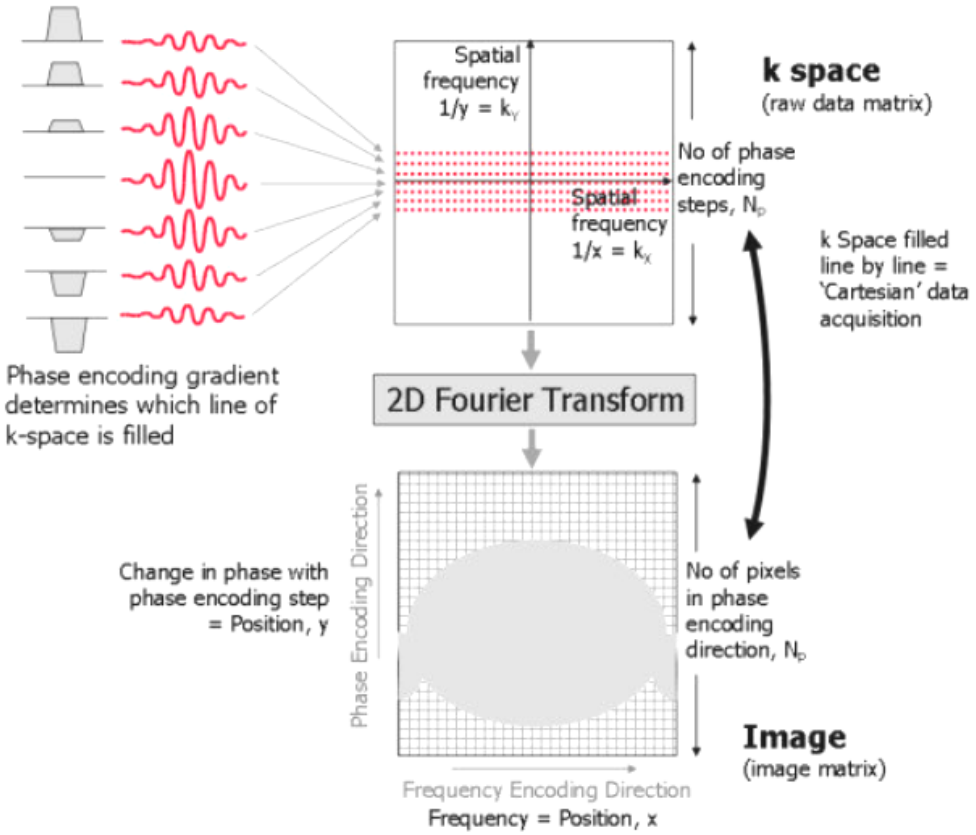

Figure 4.11 Image reconstruction, k-space and image space. The MR signals derived from each Phase Encoding step are stored in the K-space. A two-dimensional Fourier transformation of this matrix results in the reconstruction of the image. The number of phase encoding steps determines the number of pixels in the image along the phase encoding direction. The coordinates of the image are the spatial coordinates x and y. The distribution of MR signal components in the image is determined by their frequency along the frequency encoding direction (in this case, x) and by their change in phase with each phase encoding step along the phase encoding direction (in this case, y). The Coordinates of k-space are the spatial frequencies kx = 1/x and ky = 1/y. The data points in k-space (the sampled MR signals) therefore represent the spatial frequencies content of the image. In a Cartesian data acquisition, the data points are stored line by line along the kx direction, with each line corresponding to a separately sampled MR signal. The position along kx depends on the time point during the sampling period. The location of each line of data points in the ky direction is determined by the amplitude and duration of the phase encoding direction at each phase encoding step. [11]

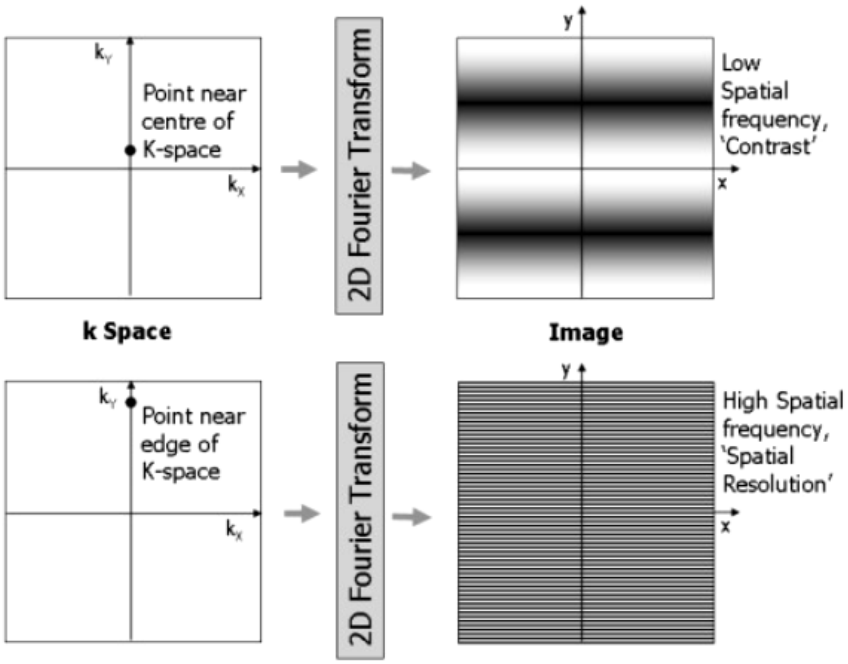

Figure 4.12 Frequency Encoding and Spatial Resolution.[11]

A single point in *k-space* defines a spatial frequency that can be represented as a wave in image space. A point close to the centre of k-space contributes a *low spatial frequency*, represented by a wave with broad peaks and troughs. This provides the signal content for large regions of uniform signal in the image and therefore the image contrast. A point at the edge of *k-space* contributes a *high spatial frequency* and is represented by a fine 'toothcomb' wave. The highest spatial frequency content defines the spatial resolution limit of the image.

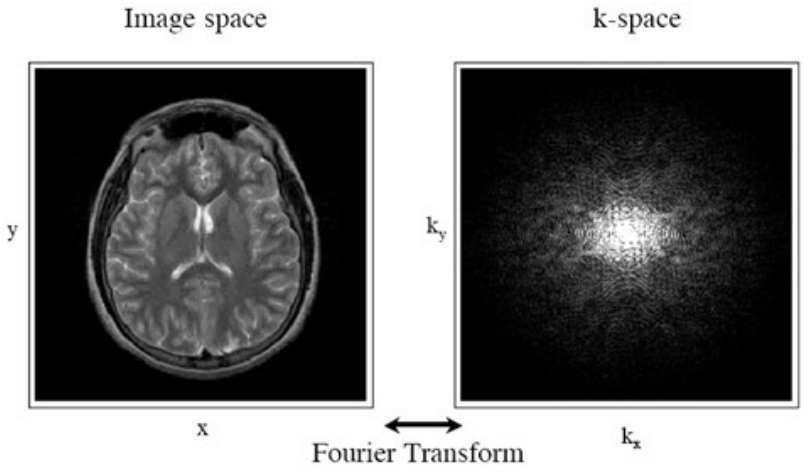

Figure 4.13 2D image – K-space image before and after a Fourier Transform.

5. Molecular movement and MRI

We must first understand the processes by which *magnetic recovery* is achieved. After an excitation of an *atomic* or *molecular* system, it returns to the state of thermodynamic equilibrium through *interactions* due to:

1. *Collisions with neighboring atoms-molecules.*
2. *Impulsive energy release.*
3. *Forced energy release.*

In the first case, the energy is released to the environment in the form of *heat* while in the second and in the third case through the emission of *electromagnetic radiation*. However, the nuclei are surrounded by electron clouds and are thus isolated from atomic-level collisions. Also, impulsive energy emission of electromagnetic energy in the frequency range of magnetic resonance is practically impossible. The main *interaction mechanism* is *forced energy transmission*. In order for this mechanism to be effective, it must have a direct effect on nuclear spins. Also, the interaction it describes must be time-varying, and it must have a periodicity with an appropriate time scale in relation to the duration of the phenomenon.

In an excited system, *magnetic recovery* is due to the magnetic interaction that results from periodic changes in the local magnetic fields of the cores through various mechanisms. These *periodic changes* lead to *T1* and / or *T2 recovery*.

Recovery mechanisms are distinguished in those that transfer energy from nuclear spins to the environment and in those that redistribute energy within the nuclear spin system. During T1 magnetic recovery, the energy is transferred in and out of the nuclear spin system (spin-grid time). In *T2* magnetic recovery, energy is retained within the nuclear spin system (spin-spin time). [2]

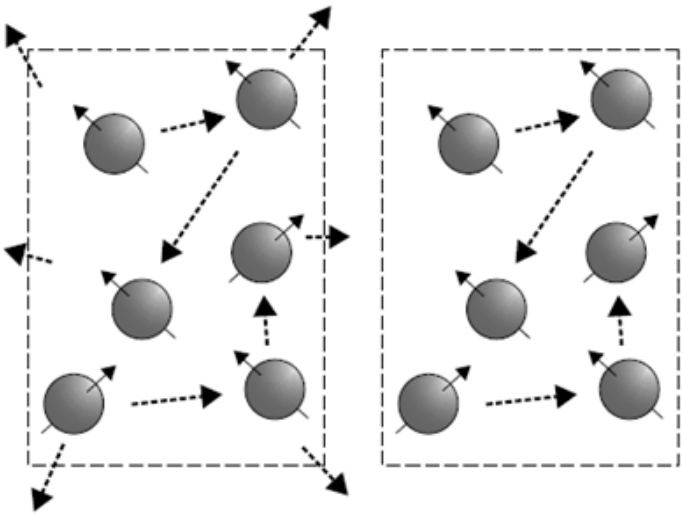

Figure 5.1 Energy exchange during T1 excitation (left) and T2 damping (right).

5.1 Randomly Fluctuating Background Magnetic Field (BR)

Periodic changes in the local magnetic fields of the cores result in the appearance of a field, which is superimposed on the homogeneous field B_0 and is called a *randomly fluctuating background magnetic field* or just *background magnetic field* (*BR*). There are many sources of *background*. The most important is *dipolar coupling*.

5.1.1 Sources of BR

I. *Dipole-Dipole interaction or Dipolar Coupling*

Magnetic dipole–dipole interaction, also called *dipolar coupling*, refers to the direct interaction between two magnetic dipoles. The rotating hydrogen core acts as a dipole. When two nuclei approach, then a local field will be created due to the interaction between the dipoles.

For example, let's suppose that there are two hydrogen nuclei within a homogeneous magnetic field B_0 at a distance r from each other. The field at the transverse B_{xy} level that will be created, due to the interaction between the dipoles, will be equal to:

$$B_{xy} \propto 1/r^3 sin\theta cos\theta \qquad (9)$$

, where θ is the angle between B_0 and the vector that connects the centers of the two nuclei

The B_{xy} will be changing constantly, because it depends on the distance and the angle which is formed between the nuclei, which are in constant motion. This *fluctuating* magnetic field induces *magnetic recovery*. [10]

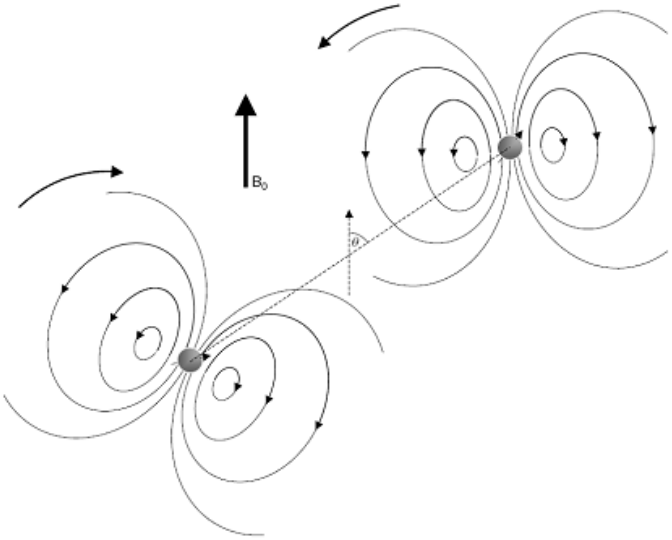

Figure 5.2 Dipole-Dipole interaction.

II. *Electron Paramagnetism*

The electron's magnetic moment is larger than *nuclear magnetic momentum*. The unpaired electrons of the outer layers of the paramagnetic atoms create strong recovery centers and thus neighboring tissues show increased rates of *magnetic recovery*.

An intensely paramagnetic element found in the human body is *iron*. Also, the external administration of paramagnetic substances which locally reduce *T1*, causing the strengthening of signal from specific areas. *Lanthanides* and *transitional elements* have been used for this purpose. *Gadolinium* compounds, such as *Gd-DTPA*, are particularly popular in clinical practice.

III. *Scalar Interactions*

When two cores interact indirectly with each other through the mediating electrons of an electronic bond, they produce a time-varying field which contributes to the system's *magnetic recovery*. An important difference of this interaction with *dipolar coupling* is its independence from the *distance between the nuclei*.

Also, the *alteration* of the magnetic field is slow, the resulting frequencies are small and therefore this mechanism contributes mainly to the restoration of *T2* and less for *T1*. It is not a very important restoration mechanism in biological molecules, but it acquires special importance in nuclear systems that are enriched with paramagnetic ions.

IV. *Spin Rotation*

Rotating molecules create their own magnetic field. As the molecules move, so do the electrons in the molecules, and an *electric current* is created. This current is the source of a magnetic field, the size of which depends on the rotation of the molecule. In other words, it is a *fluctuating* field that is partly responsible for the *tissue-repair* process.

Light and fast-moving molecules are more efficient than large molecules.

V. *Shielding Anisotropy*

As the direction of a molecule changes with the applied field B_0, so does the field exerted on its nuclei. This phenomenon depends on the intensity of B_0.

5.2 Longitudinal and Transverse components of BR

The background field can be analyzed in two components, the vertical and the parallel in the main field B_0 . The vertical component of B_0 acts in a similar way to the radio frequency pulse B_1. Some nuclei pass from high to low energy state, releasing energy to the environment, resulting in *T1 magnetic recovery*. The transverse component of the *background field* contributes in a small amount to the *T2 recovery*.

The longitudinal component of BR is added to field B_0 , resulting in local alterations in the field. The isochromatics, depending on the summed up field to which they are subject to, precess with a different Larmor frequency. Their *phase coherence* is lost and *transverse magnetization* decays.

5.3 Molecular motion and magnetic recovery times T1 and T2

Molecular motion forms the magnetic interactions between the nuclei. This happens because *molecular motion* itself involves the nuclei of its atoms as a part of the molecule. Because each nucleus has its own magnetic field (*magnetic dipolar moment* μ), as it moves it affects the local magnetic field of its neighboring nuclei. Thus, the molecular motion results in the creation of locally *fluctuating* magnetic fields and induces *magnetic recovery*. This effect can also be described quantitatively. The appropriate theory for this purpose was developed by *Bloembergen*, *Purcell* and *Pound* and is known as *BPP theory*. To understand it, we must be familiar with the concept of *molecular motion*.[13]

Every *atom* or *molecule* of the elements in nature is in a constant periodic or random motion. Also, molecules change their type of motion quickly because they collide with each other. The time for which a molecule is in the same kinetic state, that is, the time between two collisions, is called the *correlation time* τ_c . In the case of rotational motion, it is the time required for the molecule to perform a 33^o *arc rotation*, while in the case of *kinetic motion* it refers to the time it takes for the molecule to travel a distance equal to its length.

It is obvious that, for a certain type of movement, the molecules that move *slowly* will remain in the same *kinetic state* for a long time and will be characterized by *long correlation times*. The exact opposite will happen in molecules that move *fast* and have *short correlation times*. Solid molecules have a large τ_c (molecules very close to each other, in slow motion) and gases also have small τ_c (molecules more distant, fast moving). τ_c is also affected by *temperature*. At higher temperatures the τ_c *decreases*.

5.4 Frequency Distribution of BR

5.4.1 Autocorrelation Function

The *G(t) autocorrelation function* is a correlation function of the kinetic state of the molecule at two different times. In fluids and in most biological tissues, the movements at molecular level that are responsible for *magnetic recovery* are *random rotational* and *random transport molecular motion*. In this case the function is decreasing and the *BPP theory* proposes the following exponential form of it:

$$G(t) = \exp(-\tau/\tau_c) \quad (10)$$

, where τ_c is the *correlation time*.

5.4.2 Spectral Density Diagram

Any random movement can be analyzed based on the Fourier transform into individual periodic movements of different frequencies. The diagram depicting the relative intensities of harmonic motions as a function of their frequencies is the diagram of *spectral density J (ω)* of this molecular motion. The *spectral density J (ω)* is *proportional* to *G (t)* in the *frequency range*. The two functions form a Fourier pair.

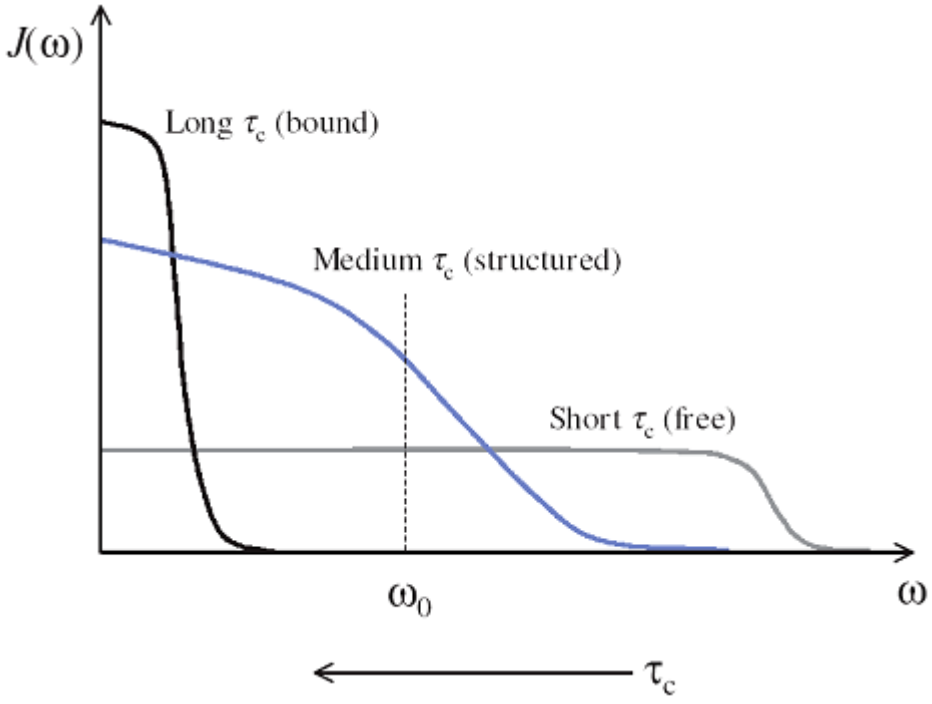

Figure 5.3 Spectral Density Diagram. [16]

The diagram above shows the *spectral density J (ω)* of three materials:

1. *large molecular weight* (long τ_c),
2. *medium molecular weight* (medium τ_c) and
3. *low molecular weight* (short τ_c).

For simplicity, we can consider an equal number of molecules from each material. The *area* of the three curves is the same because the total number of molecules involved in the movements is *constant*.

The *low molecular weight* molecules that move fast, are characterized by *short correlation times* and a quite *spread-spectral frequency density*. In other words, the number of molecules that perform a harmonic motion of a certain frequency is small but extends over a wide range of frequencies. On the other hand, *high molecular weight* molecules move slowly, have long correlation times and a spectral density that is limited to low frequencies. Overall, most molecules are located in a small, low-frequency region. Medium molecular weight molecules have an intermediate state.

The *frequency range* of each *spectral density diagram* before the *critical point* of the curve (points on the diagram of a function, where the *derivative* is *zero* or the *derivative* does *not* exist) is called the *visible spectral range*. In this region the function *J (ω)* is independent of the value of *ω*. The area around the turning point is called the spectral dispersion region.

The form of the *density function* depends on the sample being investigated, a simplified version of which is shown below:

$$J(\omega) = \frac{2\tau_c}{1+\omega^2 {\tau_c}^2} \qquad (11)$$

From the relation above, it becomes clear that at *low frequencies* ($\omega\tau_c << 1$), *J (ω)* is independent of *ω* (*visible spectral line*). In the frequency range where $\omega\tau_c = 1$, *J (ω)* decreases sharply to the value of *zero* (*spectral dispersion region*) and in the *high frequency range* $\omega\tau c >> 1$, *J (ω)* takes is equal to *zero*.

According to the BPP theory, the longitudinal relaxation rate $(T1)^{-1}$ is given by:

$$\left[T1\right]^{-1} \propto \left[B^0_{Rx}\right]^2 J(\omega) \qquad (12)$$

$$\propto \left[B^0_{Rx}\right]^2 \frac{2\tau_c}{1+\omega^2 {\tau_c}^2} \qquad (13)$$

, where B^0_{Rx} is the amplitude of the *'x-component'* of the *background fluctuating magnetic field BR*, and the transverse relaxation rate is given by:

$$\left[\mathrm{T}_2\right]^{-1} \propto (2\mathrm{T}1)^{-1}] + \frac{\gamma^2}{2}\left[\mathrm{B}_{Rz}^{0}\right]^2 J(0) \qquad (14)$$

, where *J (0)* describes the *spectral density* corresponding to the *DC* component of the *background magnetic field*. *Figure 5.4* below, shows the classic plots of *T1* and *T2* as a function of τc for fixed ω. There are two distinct regions to this diagram that are separated by a well-defined minimum in *T1* that corresponds to $\omega\tau c \approx 1$.

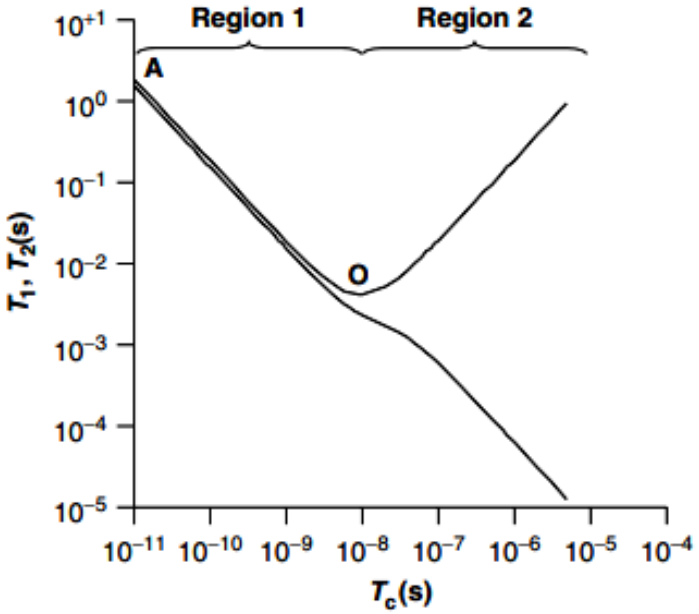

Figure 5.4 Plots of T1 and T2 as a function of τc. A minimum in T1 occurs at $\omega\tau c \approx 1$

Region 1 corresponds to the value $\omega \cdot \tau_c \ll 1$ and lies between the points ***A*** and ***O*** in *Figure 40*. In this regime, molecules tumble rapidly. The motion is so rapid that the field generated by them averages to *zero* as far as the (precessing) *isochromats* are concerned. In *Region 1* it is clear that *T2* is relatively long and is also equivalent to *T1*. The corresponding *spectral line* from the signal generated by samples in this region is narrow and as such *Region 1* is known as the *extreme narrowing regime*.

In the intermediate range of motion (dense liquids, $\omega \cdot \tau_c \approx 1$) between Region 1 and Region 2, the frequency of the *background field* matches the *Larmor frequency*. Those components that oscillate at the *Larmor frequency* will be particularly effective at driving transitions between the *two energy states* of the *spin* system. At this point on the graphs, the random *background field* is *'on resonance'* and is most *effective* at inducing *longitudinal relaxation. T1* passes through a minimum while T2 continues to decrease. In this area, where the frequency of molecular motion is equal to the frequency of Larmor, that's why *T1 recovery is the most efficient*.

Region 2 is characterized by *divergence* of *T1* and *T2*. *T1* relaxation processes also contribute to *T2* relaxation, the so called *'nonsecular' contribution*, which requires a time-varying

field. However, *Region 2* is dominated by the secular contribution which is described by the *J (0)* term in *Equation (13)*. Here the *DC components* of the *background field* start to dominate, while τ_c increases, which only contribute to *T2 recovery*. The influence of these components causes *T2* to continue to decrease linearly as τ_c increases (tumbling slows and the background field becomes ever more static). In contrast, the power available for longitudinal relaxation falls away dramatically as the background field moves away from resonance.

In conclusion, *slow movements* periodically form *low-frequency magnetic fields* and lead to more efficient *T2 recovery*. Movements that periodically form magnetic fields with frequencies close to the *Larmor frequency* lead to more efficient *T1 recovery*. [2]

References for Chapters 2-5

1. Finlay, C. C., Maus, S., Beggan, C. D., Bondar, T. I.. International Geomagnetic Reference Field: the eleventh generation. (2010) Geophysical Journal International. 183 (3): 1216. doi:10.1111/j.1365-246X.2010.04804.x
2. Tofts P. Quantitative MRI of the brain. Measuring changes caused by disease: Wiley; 2003.
3. McRobbie DW, Moore EA, Graves MJ. *MRI from Picture to Proton*.; 2017. doi:10.2214/ajr.182.3.1820592
4. Hayt MW. MRI in practice.*DentomaxillofacialRadiol*. 1999;28(1):66-66. doi:10.1038/sj.dmfr.4600402
5. Mark A. Brown, Richard C. Semelka. MRI - Basic Principles and Applications: Wiley-Liss; 2003
6. Callaghan PT. Principles of NMR microscopy: Oxford University Press; 1991.
7. Slichter CP. Principles of magnetic resonance: Springer; 1996.
8. Westbrook C. MRI at a glance: Wiley-Blackwell; 2002.
9. Robert C. Smith, Robert C. Lange. Understanding Magnetic Resonance Imaging
10. Elizabeth Berry, Andrew J. Bulpitt. Fundamentals of MRI: An Interactive Learning Approach
11. Ridgway JP. Cardiovascular magnetic resonance physics for clinicians: part I. *J CardiovascMagnReson*. 2010;12(1):71. Published 2010 Nov 30. doi:10.1186/1532-429X-12-71
12. Marinus T. Vlaardingerbroek, Jacques A. Boer. Magnetic Resonance Imaging: Theory and Practice
13. Michael L. Lipton. Totally Accessible MRI: A User's Guide to Principles,Technology, and Applications
14. Allen D. Elster. Questions and Answers in MRI (http://mri-q.com/index.html)
15. https://www.imaios.com/en/e-Courses/e-MRI
16. Lavdas I, Behan KC, Papadaki A, McRobbie DW, Aboagye EO. A phantom for diffusion-weighted MRI (DW-MRI). *J. Magnetic Resonance Imaging*.2013;38(1):173-179. doi:10.1002/jmri.23950

6. Gel Dosimetry

6.1 Gel Dosimeters as Phantoms in MRI

Phantoms play an important role in ensuring the proper operation of *magnetic resonance imaging* systems. They serve in the *quality control* of the *MRI* system of a laboratory, but also in the comparison of *(a)* the results we get from different *MRI systems* or *(b)* of the results we get from the handling of different people. However, when applying *magnetic recovery time* measurement methods (*quantitative MRI*), it is necessary to use a series of appropriate *phantoms* for measuring calibration instruments.

In this way, the optimization and validation of the measurement methods is achieved. Other uses of the *phantoms* are in staff training as well as in various experimental studies.

6.2 Properties of Phantoms

Phantoms which simulate magnetic recovery times and ADC should have certain features, including:

1. *Magnetic recovery times* and *diffusion rates* similar to those of human tissues (T_1: approximately 200-1200ms, T_2: 40-200ms, T_1/T_2:4-12 *ADC*: 50-200 x 10^{-5} mm^2/sec).
2. Ability to independently change the times *T1*, *T2* and *ADC*.
3. Same dependence of *T1*, *T2* and *ADC* on *temperature* and *frequency* measurements with those of soft tissue.
4. Chemical homogeneity.
5. Chemical and physical stability over time.
6. Ability to control the shape.
7. Low cost and easy to manufacture.

6.3 Gel dosimeter components

The main components of a polymerization (polymerization as a phenomenon will be explained in a following paragraph) gel dosimeter are:

a) *Water* (approximately 80-90%),

b) *Monomer molecules*,

c) A *gel substance* (agarose or gelatin).

Water is so abundant in dosing solutions because it gives them three special characteristics:

i) *Tissue equivalence*,
ii) Free *radicals* are produced during its *radiolysis*, which initiate polymerization,
iii) Water protons signal magnetic resonance imaging. coordination.

These dosimeters, which are made in atmospheric conditions, contain an additional substance that *binds oxygen*, the "*oxygen-scavenger*" substance (*Tetrakis (Hydroxymethyl) Phosphonium chloride-THPC* or *ascorbic acid*).

Monomers

Monomer molecules are organic compounds capable for reacting with each other to form a larger molecule called a *polymer*. The formation of the *polymer* requires *two types* of molecules, one substance that is polymerized (*monomer*) and another that connects the polymers together, playing the role of a *crosslinker*. The most common polymer *crosslinker* is *bisacrylamide-(Bis)* (*Figure 6.1*). This substance forms bonds between the polymer chains and creates the *three-dimensional distribution* of the *dose*.

From 1994 until today, there are various types of monomer molecules used in polymerization gel dosing, each of which gives the corresponding name to the type of dosing meter. PAG dosimeters contain polyacrylamide as a monomer and were introduced in 1998 [1]. A year later, VIPAR dosimeters with *vinylpyrrolidone* monomers were discovered. Also in 2004 appeared *HEA*, containing *acrylamide* with ethyl alcohol (*Hydroxymethyl acrylate*) [2] and in 2006 *NIPAM* [3] containing *isopropylarylamide*. The most common *monomer molecules* are shown in *Figure 6.1*.

It is noted that these molecules are *toxic* and affect the central and peripheral nervous system. In fact, the crosslinker substance of monomers causes itching. That is why it is necessary to take protection measures during the manufacture process of the gel dosimeters (such as special clothing, gloves etc.) and to provide the appropriate facilities (lab) for their preparation.

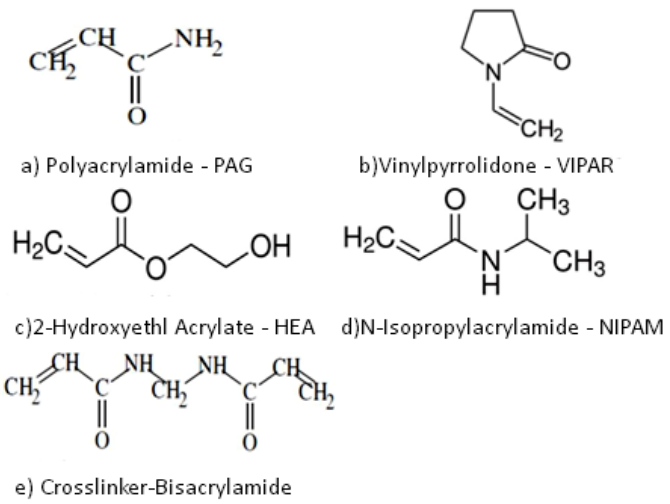

Figure 6.1 Structural formulas of the most common monomers (a-d) and the polymer crosslinker (e) molecule.[3]

Today, the only non-toxic monomer is *isopropylachrylamide*. After use, the dosimeters melt at high temperatures and are removed from the various phantoms in which they were injected. Each laboratory must have special disposal sites for the used solutions.

The size of *monomer* molecules is measured in Angstrom ($4 \sim 30 \times 10^{-10}$ m). The mean distance between the monomers in a non-irradiated dosimeter depends on the % content of the monomer in the solution. Specifically for PAG dosimeters that have 3% w / w monomers and 3% w / w polymer binding, the average distance between the monomers is 20×10^{-10} m and 25×10^{-10} m the average distance between the connector molecules. Also, the average distance of water molecules is about 4×10^{-10} m and the size of gelatin molecules is very large compared to the molecules of the other components. Therefore, gelatin molecules have little effect on the diffusion of other small molecules [4].

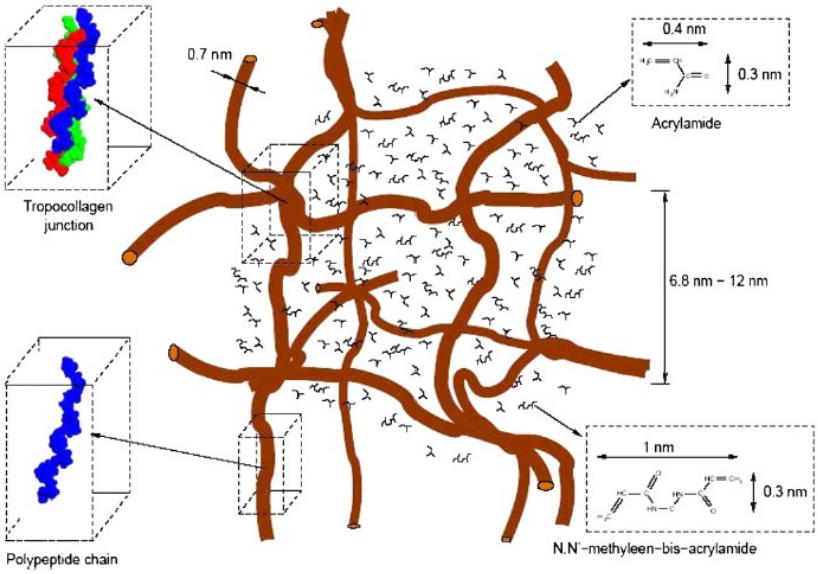

Figure 6.2 Representation of the microscopic construction of the non-irradiated polymerization gel dispenser [4].

In recent years, a new way of expressing the *content* of monomer molecules in the dosimeter solution has been used. Specifically, two *contents* describe the composition of the solution, *% T* and *% C*.

% T is the content of monomer molecules and polymer crosslinker molecules relative to the total mass of the solution.

$$\% T = \frac{total\ mass\ of\ monomers}{total\ mass\ of\ the\ solution} \quad (19)$$

% C is the content of the molecules of the crosslinker substance relative to the total mass of the monomer molecules and their molecules of the bonding substance.

$$\% C = \frac{total\ mass\ of\ crosslinker\ \ molecules}{total\ mass\ of\ monomers} \quad (20)$$

Gelation Substances

In order for the polymer gel dosimeters to keep the polymers firmly in place during irradiation a gelation substance is needed. With this substance, the dosimeters coagulate and the polymer chains that are formed and connect together do not diffuse. In addition, they remain stable spatially, maintaining the three-dimensional distribution of the dose. The first gelation substance used was *agarose*, a polysaccharide whose main ingredient is *agar*. Gelatin was then used, a transparent, tasteless substance which contains collagen, which is isolated from the skin and bones of animals.

Today, almost all polymer gel dosimeters contain *gelatin* as a gelation substance. It was chosen because it has better characteristics compared to *agarose*. Gelatin dissolves more easily in water, is cheaper and improves the discretion of the dosimeter. The structure of polymer gel dosimeters is determined by the percentage of *gelatin* and *monomer* molecules in the solution. Usually the *gelatin* content of the solution ranges from *4% w / w ~ 7% w / w.* A particularly important feature is the *gelation* of aqueous gelatin solutions, which is characterized by the creation of a three-dimensional layout of *biopolymer chains*. The creation of this network comes from the maturation of the *collagen* contained in *gelatin*. A *collagen unit* is a *280nm* long rod, made of *polypeptide chains*, wrapped around each other, creating a helix in space.

The *gelation process* begins just a few minutes after the temperature of the solution drops to 35^0C. After the first few hours, the rate of gelation decreases significantly. However, the gelation continues even a week after the manufacture.

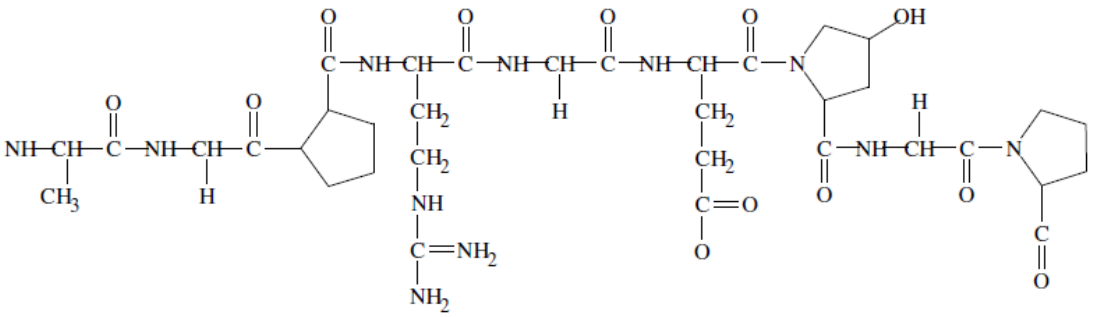

Figure 6.3 The structural formula of the gelatin molecule.[5]

Oxygen scavengers

The presence of oxygen in the atmosphere prevents the recording of the absorbed dose of the polymer gel dosimeters. Oxygen molecules connect with the initial roots of the polymers, so they won't connect with each other, preventing the polymerization process to end. Due to this fact, initially the gel dosimeters were made in *nitrogen* and *argon* cages.

In 2001, Fogg [5] proposed the use of substances that would bind atmospheric oxygen without terminating polymerization. The substance they used was *ascorbic acid* and the new dosimeter was named *MAGIC* and could be produced in atmospheric conditions. Then, the use of other *"oxygen-scavenger"* substances for the production of dosimeters under atmospheric conditions was studied. Of all the studied substances, the most effective is *"Tetrakis" THPC*, an ionic compound with *phosphorus* and *methyl hydroxyl*.

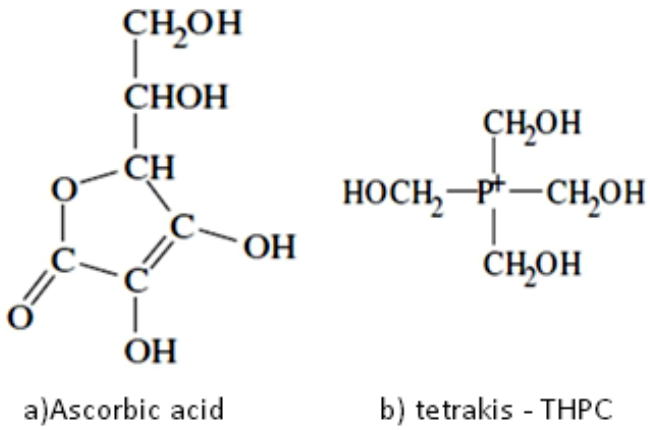

Figure 6.4 Structural formula of the oxygen-scavenger molecules a) Ascorbic Acid and b) tetrakis THPC.[6]

Today, the most common substances are *Tetrakis (THPC)* and *Ascorbic acid*, which can be used to produce polymer gel dosimeters faster and more economically. Depending on the monomers of the dosimeter, each of these substances has a different effect on its dosimetric characteristics [6]. Therefore, for the effective use of these substances, it is necessary to carefully choose the appropriate substance and its concentration, in order to bind oxygen.

6.4 Gel dosimeter manufacture and storage

The time required to make a polymer gel dosimeter depends on the type of dosimeter that is to be created, the amount needed and the manufacture conditions (whether it is in a cage or in atmospheric conditions). Various research teams have been following almost the same manufacture process with small differences. The following is the usual production process under atmospheric conditions.

Initially, the volume of the required dosimeter is calculated and the phantoms to be irradiated are filled with *double distilled water*. This amount of water is poured into a container of refractory glass and 10% extra double distilled water is added, due to the reduction of the volume of water from its evaporation. The container is placed together with a magnetic stirrer in a *magnetic hotplate stirrer (Figure 6.5)*.

Figure 6.5 Magnetic hotplate stirrer.

The amount of water is heated to 40^0C. When the temperature stabilizes, gelatin is added, which is constantly stirred to dissolve. Once the solution is clear, the temperature of the solution is reduced to 34^0C. Then the *monomer* is added, after it is completely dissolved, the substance that will connect the polymers (*Bisacrylamide crosslinker*) is slowly added. It takes a long period of time for *Bis* to dissolve completely. When it is completely dissolved, the solution is cooled again until its temperature reaches 32^0C and then the *oxygen-scavenger* substance is added. Once it is completely dissolved, the solution is injected into the phantoms. It should be noted that during the preparation, the temperature of the solution should not exceed 50^0C. If the temperature of the solution is high enough, polymerization is likely to start due to the high heat. A study in *2000* [7] states that changes in temperature during the manufacture of the gel dosimeter affect its dosimetric response and also affect the repeatability of the method.

It is especially important to keep the phantoms of the solutions, because these dosimeters are sensitive to *light* and *temperature*. Specifically, the solutions in order to coagulate, they are being placed in a dark place with a temperature around 10^0C for one day. The dark part is chosen because the dosimeters are sensitive to light and by exposing them to it, it is possible for *photo-polymerization* to begin before they are irradiated. Therefore, their protection from light is necessary. Usually the phantoms are covered with a *parafilm* (a semi-transparent, flexible film) for extra protection. In addition, special care is required for the temperature of the storage space. A study was conducted in *2007* [8], which showed that the dosimeter response changes and depends on its storage temperature. For this reason, it is recommended that the dosimeters be stored in a dark place with a controlled temperature and that their storage temperature should not deviate from the temperature of their irradiation and reading. Changes in radiation temperature affect the response of the dosimeter and changes in temperature during reading affect the discretion of the dosimeter, its accuracy and repeatability [9].

6.5 Polymerization Reaction

In general, 90% of a polymerization gel dosimeter consists of water. During the irradiation and absorption of the radiation energy from the dosimeter, water is radiolyzed. During *radiolysis*, *electrons* and *positively charged ions* (*cations*) are produced by water and they are called *free water radicals*. These *radicals* are very active and react with the monomer molecules of the dosimeter. The size and type of radiolytic products produced in the first femtosecond (SI unit: $10^{-15}s$) after irradiation depend on the type and energy of the radiation.

For *photon radiation* (of the *MV* order) used in radiotherapy, the position of the radiolytic products is located inside an area of the order of one nanometer (*1 nm*) around the path of the radiation. These phenomena occur in a very short time and in infinitesimal space, which is why their observation is limited due to quantum uncertainties. From the moment of the creation of the radiolytic products, the probability of free radicals approaching the monomers through the *Brownian motions* is increasing with time [10].

Initiation is the first step of the polymerization process. During *initiation*, an active center is created from which a *polymer chain* is generated. The polymerization initiation reaction occurs when the free radicals of the water react with the monomer molecules, breaking the double bonds of the monomeric carbon atoms and creating free molecular radicals of the monomers. The rate of the reactions depends on the ability of the monomer to react with the free radicals and on the concentration of both, the monomer and the free radicals in the solution. The concentration of free radicals in the solution depends on the dose of radiation. Thus the evolution of the polymerization reaction is controlled by the type of monomer molecules, the concentration of the monomer and the dose rate of the radiation.

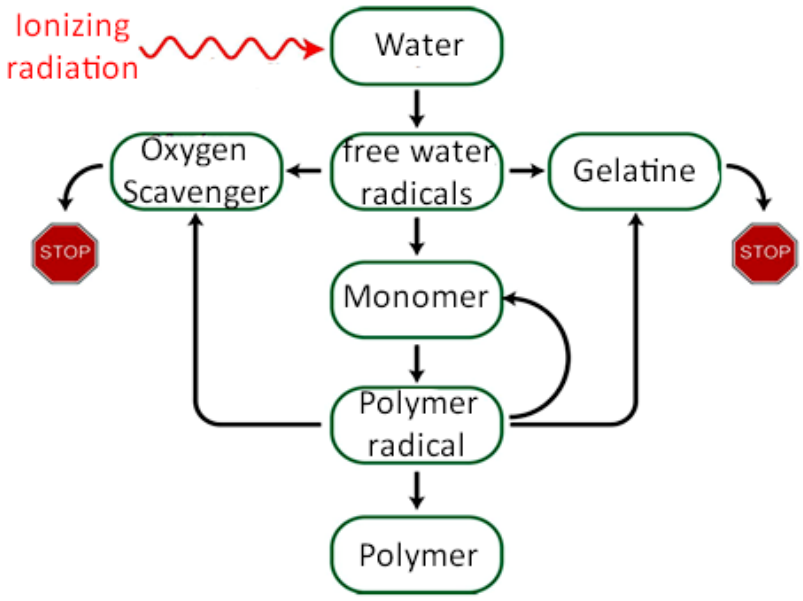

Figure 6.6 Schematic representation of the chemical reactions of the polymer gel dosimeter components with ionizing radiation.

The next stage of the polymerization reaction is *chain propagation*. At this stage, the ends of the free radicals of the monomers, which are created at specific points in the mass of the dosimeter, are joined together in a straight line. With this process, straight polymer chains are created, which grow depending on the number of free radical monomers created during the absorption of the radiation. The *crosslinker* molecule plays an important role in the process of forming *polymer chains*. This substance connects the straight polymer chains together, creating *vertical joints*. With these reactions, a three-dimensional (3D) structure of polymer chains is created in the mass of the dosimeter, which is called the *Polymer*.

The final stage of the polymerization reaction is the *chain termination*. The development of the polymer chain can be stopped when two chains are joined together having only one active end for their joint. After this reaction, the chain cannot grow further and the *polymerization* is terminated. The *gelatin* contained in the solution plays an important role in maintaining the *three-dimensional* polymer structure, formed in the dosimeter. In particular, the polymer is trapped inside a *semi-solid* matrix, which is made of *gelatin*. This *matrix* provides the polymer mechanical stability, keeping it stable within the mass of the dosimeter. This keeps the spatial distribution of the dosimeter constant. Finally, it is noted that by increasing the concentration of *gelatin* in the dosimeter solution, the extent of the polymerization is reduced, while the spatial information of the distribution is being maintained in a specific position in the dosimeter.

6.6 Radiotherapy techniques and Polymer gel dosimetry

Modern radiotherapy techniques have drastically altered the dos process to the target tumor. The complexity of the procedure resulted in an increased need to confirm the 3D dose distribution. The usual two-dimensional dosimetric techniques used partially, determine a dose distribution and require reconstitution to produce the three-dimensional distributions. This makes clear that it is needed to use a dosimetric system that can directly render the 3D dose distribution with high accuracy and physical identification in 3D reality. Gel polymer dosimeters (gel) were developed for this cause.

Polymer gel dosimeters belong to the category of *chemical* dosimeters. Their function is based on the fact that exposure of chemical dosimeters to ionizing radiation causes changes in their chemical properties [38]. In particular, the percentage of absorbed dose is related to the extent of the chemical changes caused to the dosimeter. By adding a gelatin agent, the chemical dosimeter solution can be spatially stable and provide information on 3D dose distribution. By optimizing imaging techniques, these changes can be visualized and evaluated with great accuracy.

Polymer gel dosimeters have been shown to be a valuable tool for measuring characteristic radiation beams [39, 40, 41, 42 and 43] as well as for three-dimensional confirmation of dose distributions in radiotherapy [44, 45, 46 and 47].

Today, several different types of polymer gel systems have been introduced, each with different dosimetric characteristics. The vast majority of these dosimetric systems, their characteristics and their usefulness in measuring radiation beams as well as in three-dimensional dose confirmation in radiotherapy have been presented [4] in terms of study, evaluation and documentation. However, despite the large number of available polymer gel systems, each with different characteristics, their use in clinical practice has not yet been adopted. Any such new system introduced should be determined by all its dosing and functional characteristics so that it can be used safely in clinical radiotherapy.

The minimum set of these features should include:

1. *Dose response* and *repeatability* characteristics - useful dose range.
2. *Sensitivity* of the dose response characteristics to the "*phantom preparation and irradiation*" time period.
3. *Sensitivity* of dose response characteristics in relation to "*irradiation and reading*" time.

The problem in evaluating the final accuracy of the dose maps obtained in a gel dosimetry experiment is that there is no 3D 'gold standard' with which to compare. The most reasonable strategy is to compare doses obtained with gel dosimetry with doses obtained by the 'most reliable' dosimetry techniques that apply to a certain spatial dimension. As such, dose profiles of a single photon or electron field can be compared with dose profiles obtained with an ionization chamber or diamond detector [47]. In two dimensions, gel dosimetry can be compared with film dosimetry [39, 47]. Most comparisons have been made with treatment plans [16, 18 and 50]. The verification of the treatment plan can be seen as the most important application of gel dosimetry in radiotherapy quality assurance so far. Factors that have an influence on the accuracy are listed in *Table 2*. These factors can be classified in two categories: (1) dosimetric factors cause deviations between the measured dose and the described dose and (2) spatial deviations cause deviations in the spatial distribution of the delivered dose. In terms of the chemical processes within the gel dosimeter, inaccuracies arise from differences in dose–response between calibration phantoms and the dose verification phantom, from chemical instabilities and from the loss of spatial integrity [4].

Table 2. Factors influencing the precision and accuracy in 3D gel dosimetry under conditions of good practice. [4]

	Precision		Accuracy	
	Dosimetric	**Spatial**	**Dosimetric**	**Spatial**
Fabrication	Dose sensitivity of the gel dosimeter	Spatial variations in manufacturing temperature	Discrepancies between calibration vials and phantoms	Volumetric contraction of the gel dosimeter
			Chemical stability spatial stability	
Radiation	Stochastic variation in the delivered dose	Variations in phantom positioning	Positioning error of the calibration phantom	Phantom positioning error
	Variations in the temperature during irradiation	Spatial temperature variations in combination with temperature sensitive dose response	Dose-rate-dependent response	
	Variations in the temperature during irradiation	Spatial temperature variations in combination with temperature	Dose-rate-dependent response	
	Reproducibility of calibration phantom positioning		Energy-dependent response	
	Radiochemical noise		Temperature dependence	
			Tissue equivalence	
			Recipient wall effects	
Imaging	Stochastic noise	Voxel size/shape (resolution)	Voxel shape (bandwidth) imaging artifacts	Imaging artifacts
			Temperature during scanning	

6.7 Magnetic Resonance Imaging techniques for gel dosimeters

After irradiation, the polymer gel dosimeters should be able to produce *dose distribution maps*, with the use of an *imaging technique*. Today, various imaging techniques are used to evaluate them, such as *MRI*, *Optical CT*, *x-ray CT*, *Ultrasound* and *Raman spectroscopy*. An imaging method is effective in *polymer gel dosimetry* when it is able to detect the changes caused by radiation inside the dosimeter.

The first *imaging technique* used [11] was *Magnetic Resonance Imaging*, which is the most common method. The principles of Magnetic Resonance Imaging are described in the next paragraph and will be analyzed further since it is the technique method used in this study. This technique is the most common for estimating the dose of polymer gel dosimeters. In particular, the chains of polymers created by the precipitation of radiation, affect the mobility of water molecules in the dosimeter. The water molecules, which are attached to the chains of the polymers, can move very slowly and very finely compared to the water molecules, which are located near the monomers of the non-irradiated dosimeter.

The *MRI* detects these changes by measuring the high or low magnetic recovery rates of the water molecules that are attached to the polymers. The extent of the polymer chains inside the dosimeter is related to the absorbed dose. As long as the arrangement of the polymer chains is maintained spatially in the gel solution, the dose distribution can be illustrated using *MRI*.

The correlation between the irradiated dose and the rates of magnetic recovery is achieved by producing a calibration curve between the rate of magnetic recovery and the dose of radiation (*R2-dose calibration curve*). This method is used for absolute dosimetry. Changes in the composition and structure of the radiation-induced dosimeter alter the rates of magnetic resonance imaging (*R1*) and sphincter (*R2*). These changes are related to the absorbed dose and the calibration curve is generated. Changes in spin-magnetic recovery rates (*R2*) due to radiation are more intense than those of spin-mesh (*R1*) rates. For this reason, the estimation of polymerization gel dosimeters is based on *R2* changes.

Although *MRI* has been shown to be a reliable and highly accurate method for measuring the dose of polymerization gel dosages, its application contains several difficulties and disadvantages. Its use is quite limited, due to the high cost of system equipment and the restriction of access to these systems due to the high workload in clinical settings. Another disadvantage of the method is the effect of temperature changes on the accuracy of the estimation of dose distributions during scanning of the sample.

Also, the accuracy of the measurement is downgraded by the existence of technical errors (false indications) contained in the *MRI*. These false indications are caused by various factors, such as the spatial inhomogeneities of the magnetic field, the gradient fields and the radio frequency fields, the selected dimensions of the display field, the developing fluctuations, the choice of the range of the reception zone [13, 14, and 15].

In the following paragraphs, the Spin Echo technique is described, the evolution of which is the Multiple Echo Spin Echo, as well as some other fast sequences, including the *HASTE* technique.

6.7.1 Spin Echo technique

The Spin Echo technique was introduced in 1950 by Hahn and it is the basic sequence in MRI, on which other sequences are based [1, 2, 5]. The schematic representation of this sequence is shown in *Figure 6.7.* First we consider a nuclear spin system, in the selected section, which is in a state of thermodynamic equilibrium and interacts with a *90º RF pulse* [*Figure 6.7 (1)*]. The application of the *RF pulse* causes the spread of the isochromatic spins, which resembles with the opening of a fan, and induces a weak signal of Free Induction Decay (FID) in the receiving coil.

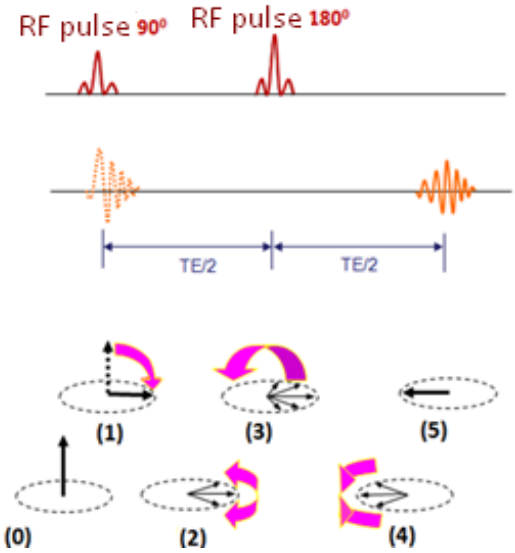

Figure 6.7 The Spin Echo technique in a nuclear spin system.[48]

The *spread of the isochromatics* and the weak *FID signal* are produced due to *pseudo-restorations* of *T2**, which appear due to the heterogeneities of the static magnetic field. Hahn's aim was to minimize the effect of the *T2* pseudo-restorations* of the signal produced and to enhance *T2 restorations*, so that the final receiving signal depends mainly on restoring the *transverse magnetization* of the hydrogen nuclei in the area of interest.

Minimizing field inhomogeneities in the generated signal was achieved using another RF *pulse of 180º*, which is applied for a short time (*TE/2*), after the 90º RF pulse [*Figure 6.7(3)*]. The use of this pulse causes a time reversal of the evolution of the phenomenon, while maintaining the direction of the movement of the isochromatics. Therefore, after the *180ºRF pulse*, the fast isochromatics will be chronically behind from the slow ones. Then the fast isochromatics will start to approach the slow ones [*Figure 6.7(4)*] and the "*fan*" will start to close.

After a period *TE* of time, the fan will be closed, the system will have been returned to equilibrium [*Figure 6.7(5)*] and the *FID* signal that will be produced will mainly depend on the *T2 magnetic recovery*. This signal is called "*echo*". The technique, in which we produce only one *FID* signal (one "echo") in *TR* time using a *90º* pulse and a *180º* pulse, is called *Spin Echo technique*.

6.7.2 Multiple Spin Echo Techniques (Carr Purcell and Carr -Purcell-Meiboom- Gill)

A series of multiple "echoes" (Multi Echo Spin Echo) provides a series of signals to many "echoes" of the sample, each of which is received at a different time. In order to achieve the production of many "echoes" from the same sample, it is necessary to use pulses 180◦. The result in two dimensions is the production of a series of images from a specific section of the displayed sample at regular intervals. Using appropriate customization algorithms, these images are processed and reconstituted to produce a computed mathematical image called a two-dimensional parametric value map.

Today, the use of a *Multi Echo Spin Echo* (*MESE*) sequence has been shown to measure the dose of gel dosimeters, resulting in optimal noise reduction in the generated image [12]. In this way, the signal-to-noise ratio in the image is optimized and the spatial resolution of the dosimeter is increased. Thus, in order to display a polymerization gel dosimeter, it is necessary to use a suitable sequence, in order to visualize spatially the optimal possible spatial resolution of the dosimeter in the shortest possible time.

A. Carr Purcell (CP) Technique

A few years after the introduction of the *Spin Echo technique* (1954), *Carr and Purcell* proposed a new technique based on *Hahn's* technique, but with fewer errors. This new technique has been called *Multiple Spin Echo*, because in *TR time* many *180º* RF pulses are applied and not just one as in the Spin Echo technique. Each *180º RF pulse* is emitted at a specific time and after its application a *FID* signal is created (*echo*).

The series of the applied *180º RF pulse* create a series of signals of the same region as they weaken over time (*Figure 6.8*). These signals received on a TR time have the same phase encoding. Thus, everything is stored in the same line of the *K space*.

The main advantage of this technique is the fact that the scanning of the area of interest is much faster. Another advantage is that there is a minimization of molecular diffusion errors, due to the reduction of the *time interval* (*TI*) between the two pulses.

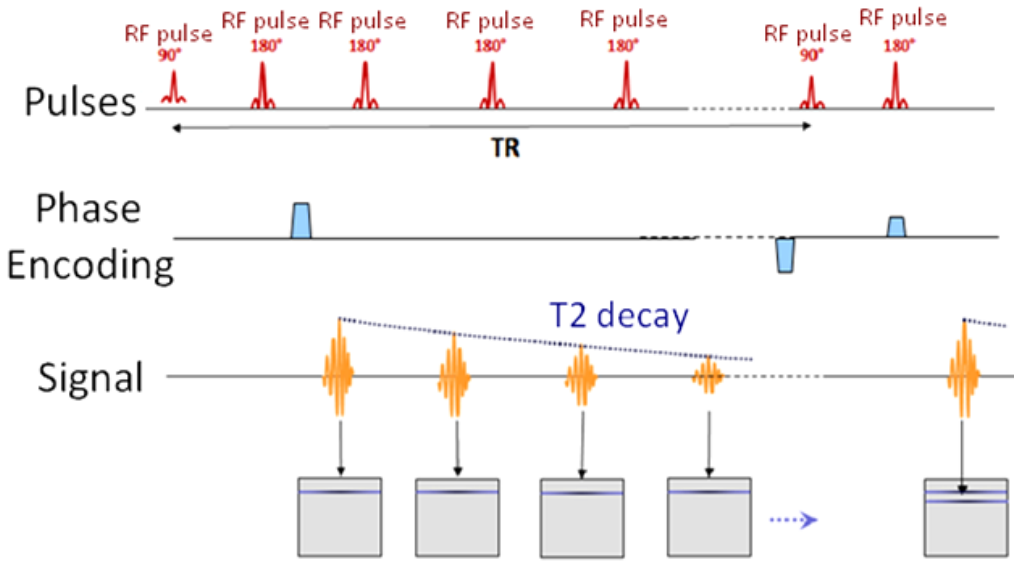

Figure 6.8 The Multiple Spin Echo technique.[48]

B. Carr Purcell Meiboom Gill (CPMG) Technique

In 1958, Meiboom and Gill introduced a new sequence, based on *CP technique,* but improved, in terms of cumulative errors. The difference between the new *CPMG technique* and the *CP technique* is the application axis of the *180º* RF pulses. Specifically, in the *CP technique*, the *90º RF pulse* and

the *180⁰ RF pulses* are applied to the same axis, ***x***. This, however, creates errors caused by the *heterogeneity* of the *180⁰ RF pulses*.

In contrast to the CPMG technique, the 90⁰ RF pulse is applied along the ***x***-axis, while the 180⁰ RF pulses are applied to the ***y***-axis. In this way, each time a 180⁰ RF pulse is applied to the ***y***-axis, brings back *in phase* possible errors, which may have been created by applying an inaccurate previous *180⁰ RF pulse* to the same axis. This process results in minimizing the cumulative errors associated *inhomogeneities from the 180⁰ RF pulse*.

Finally, another technique based on the previous two is *Phase-Alternating Phase-Shift (PHAPS)*. During this technique, each line of the K space is stored twice [6]. First consisting of signals recorded with the *CP technique*, where the *90⁰* RF pulse and the *180⁰ RF pulses* are applied to the same axis, ***x***. Then, the same line is recorded using the *CPMG technique*, where the *90⁰* RF pulse is applied along the ***x*** axis, while the *180⁰* RF pulses are applied along the ***y*** axis.

6.7.3 RARE (Rapid Acquisition with Relaxation Enhancement) techniques

RARE techniques are quick versions of the *Multiple Spin Echo technique*. They are usually referred to as *Fast Spin Echo* (General Electric) or *Turbo Spin Echo* (Siemens, Philips) techniques depending on the manufacturer. In these techniques, unlike conventional Spin Echo, in only one TR more than one phase encoding gradients are applied (application of different phase encoding gradients), so that many lines of the K space are filled in a time period of one TR.

Each *echo* created after a *180⁰* pulse is encoded incrementally with respect to phase, in order to fill a different line of *K space*. The number of signals received from a series of *180⁰* pulses in one *TR,* is called the *Turbo factor*. As shown in *Figure 6.9*, more than one line of K space is recorded in each *TR*, depending on the *Turbo factor*. This technique fills the *K space* faster and the *scanning time* is reduced depending on the number of echoes that are being received in each *TR*.

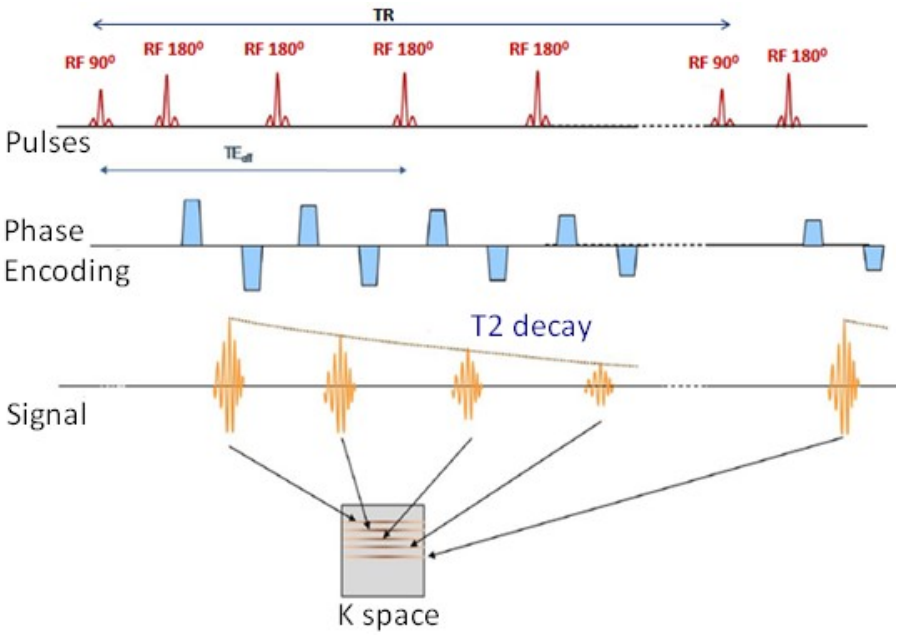

Figure 6.9 The Fast Spin Echo technique. Completion of many lines in K space in only one TR.[48]

The two fastest versions of these techniques are the *SSTSE* and *HASTE* techniques. In the *Single Shot Turbo Spin Echo (SSTSE)* techniques, all the lines of *K space* of a slice are recorded in one TR. Half Fourier Acquisition Single shot TSE (HASTE) techniques fill the half lines of *K space* in one TR. The rest of the K-space lines are supplemented by using *Fourier transform* for better image resolution, while reducing the series of the pulses.

HASTE technique consists of an initial *90ºRF pulse* and then *multiple 180º RF pulses* follow. So, we receive an image from only one section (the first one). In the next TR, there has been magnetic restoration and the HASTE sequence starts from the beginning, for the next section, with a next *90ºRF pulse.*

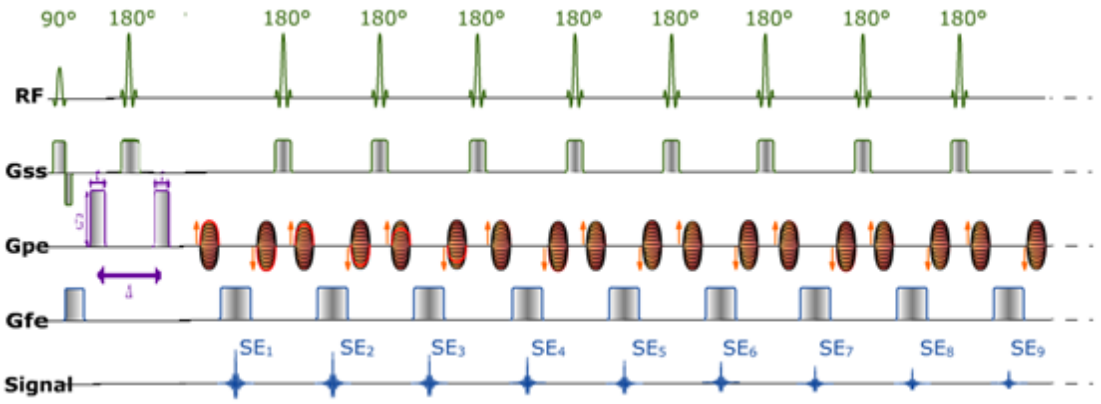

Figure 6.10 The HASTE sequence. [48]

The main disadvantage of the fast technique sequences is that each line of *K space* has a different effect on the *T2 restorations*, because over time the T2 signal decays. This results in the deterioration of the *spatial resolution* of the final image. Recently, efforts have been made to improve the performance of these techniques so that they can be used as reliable methods for reading polymer gel dosimeters.

6.7.4 Selection of Magnetic Resonance Imaging Parameters in Polymer Gel Dosimetry

Imaging parameters, such as the *TE*, *TR* times, the *nutation angle*s of the magnetization, have a large effect on the *contrast* of MR images [7]. The most common *contrast parameter* used in polymer gel dosimetry is the *restoration rate R2* (spin-spin). During scanning, *T2* emphasis images are generated. These images are collected to construct the calculated *R2 maps*.

Theoretically, *T1* and *T2 emphasis maps* can be constructed, but it has been shown that the heterogeneities of the magnetic field and the radiofrequency pulses have a negative effect on the *dose reading accuracy* from these maps [8]. These effects can be minimized by constructing the *calculated R2 maps*, since the changes in this rate are directly proportional to the radiation dose.

Many imaging techniques can be used to produce *quantitative R2 maps*. The simplest technique is the conventional *Spin Echo*. In this technique, by changing the *TE parameter*, the *emphasis* of *T2 restoration* on the *base images,* which are received from the MRI system, changes. Finally, the *R2* value in each elementary section of the calculated R2 map, is calculated from *two T2 base images* [*Figure 6.11 (a)*].

To optimize the *Signal to Noise Ratio (SNR)* of the *R2 maps*, it is preferred to use the *Multiple Spin Echo technique* [9]. In this sequence, several different *T2 emphasis images* are obtained during a *TR*. Each *R2 value* of each elementary section of the *calculated R2 map* is calculated by *fitting* the *T2 values* to an *exponential curve*, which corresponds to the signals of the base image pixels [*Figure 6.11 (b)*].

Also, a percentage of the *SNR* from the initial base images can be reduced by selecting the right *TE*. The more *TE's* there are, the more base images are taken. The only limitation in the choice of the number of *TE* is the minimum required time between two consecutive *TE* (ΔTE_{min}). In order to receive two consecutive acceptable signals, there must be a *time interval* (*TI*) between them to stimulate, encode and restore the system.

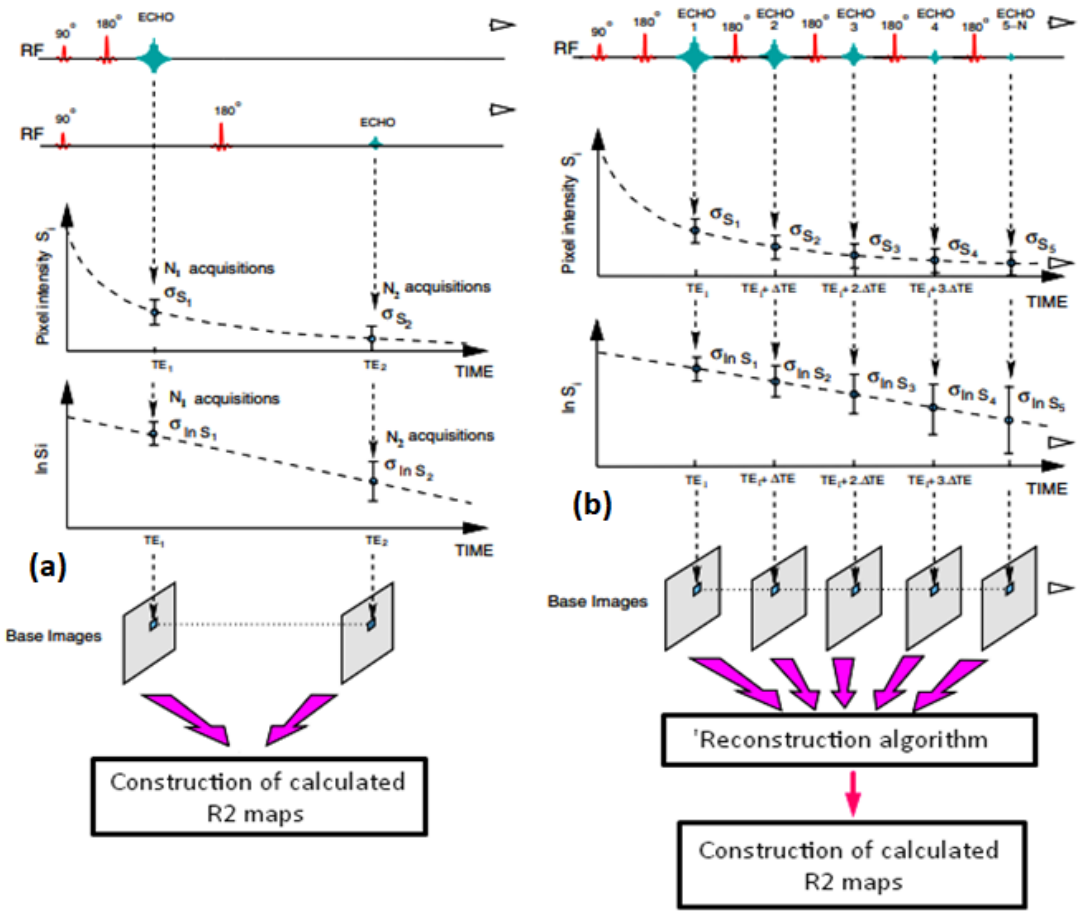

Figure 6.11 Construction of calculated R2 maps, using **(a)** the Spin Echo technique and **(b)** the Multiple Spin Echo technique [4].

6.8 Dosimetric Characteristics

Polymer gel dosimeters have a special place in the *dosimetry* of radiotherapy due to their ability to record the dose in three dimensions (3D). Prior to their application in clinical practice, their accuracy and reliability must be assessed and determined.

This evaluation is achieved by studying their *dosimetric characteristics*, such as:

a. dose response,
b. dose sensitivity,
c. dose resolution,
d. temporal and spatial stability,
e. dose rate and energy dependence
f. temperature dependence during irradiation – storage – scanning
g. tissue equivalence and
h. reproducibility

Each of these features is described in detail below.

a) Dose Response

The basic principle, on which the use of polymerization gel dosimeters is based, is that the radiation falling on the dosimeter causes the polymerization of the monomer molecules, and the polymer chains formed remain in a specific position in the extent of the dosimeter. The extent of polymerization is proportional to the amount of dose absorbed. In fact, because polymer molecules interact with water molecules, the extent of polymerization can be estimated from the Magnetic Resonance Imaging. In particular, it has been found that the rate of magnetic resonance imaging (R2) varies depending on the dose absorbed.

The response to the dose of a dosimeter can be estimated from the display of a series of glass vials filled with a gel solution, each of which has been irradiated at different doses (*Figure 6.12*). A vial of radiation is always left unattended and the doses at which the vials are exposed are related to the response of each dosimeter. The *R2* response and dose of a polymerization gel dispenser follows exponential behavior. In each such response there is a dose saturation limit. This limit is a specific dose value above which no change in R2 rate is observed and where all monomer molecules have been consumed and converted to polymers. This limit depends on several factors, but mainly on the type of monomer molecules and their concentration. In order to accurately use polymerization gel dosimeters in specific radiotherapy shots, it is necessary to visualize the calibration vials together with the treatment plan verification model in order to minimize the uncertainty in calibrating the dosimeter. In this way, absolute dosimetry is achieved. Other less accurate dosing methods have also been presented [16].

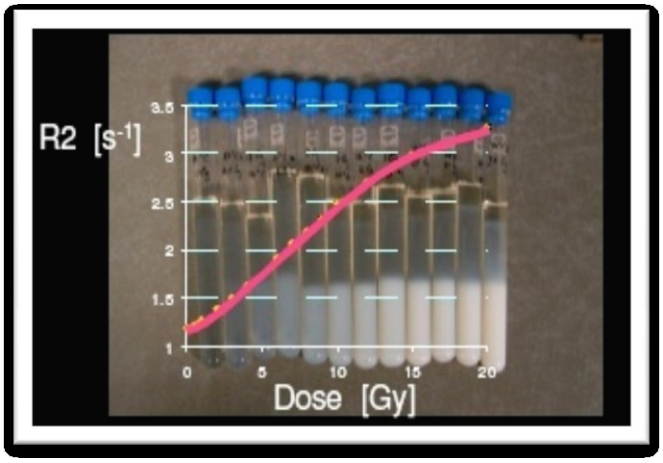

Figure 6.12 An example of calibration of irradiated vials.

b) *Dose Sensitivity*

Dose sensitivity is the change in the magnetic recovery rate of the *ΔR2 spin-spin* compared with the change in *dose* at the linear region of *the R2-dose response curve*, given by the following relation:

$$Sensitivity\ R2\text{-}dose = \frac{\Delta R2}{\Delta(dose)} \qquad (21)$$

The dose sensitivity depends on the *concentration* and the *type* of the monomer, as well as on the temperature and time of measurement (the time where the imaging took place). In literature, different sensitivity values have been presented for different types of monomers as well as for different imaging/scanning times [17, 4, 18].

c) *Dose Resolution*

To determine the optimal and appropriate *dose range* for each polymer gel dosimeter, it is necessary to determine the accuracy of the estimated dose at different *Confidence intervals p (Confidence Level)*. This accuracy is determined by the concept of *dose resolution* in determining the dose $D^P{}_\Delta$ [19]. This size is defined as the minimum dose differentiation between two dose distributions with different values at a specific level of confidence p. $D^P{}_\Delta$ is the minimum detectable dose, and should theoretically be close to zero. It is calculated from the following relation:

$$D_\Delta^P = k_p \cdot \sqrt{2} \cdot \sigma_D \qquad (22)$$

, where k_p , is the factor is related to the type of dose distribution and σ_D is the standard deviation of the measured dose (*Figure 6.13*). The error in measuring the σ_D dose depends on the sensitivity of the dosimeter and the uncertainty in measuring each point.

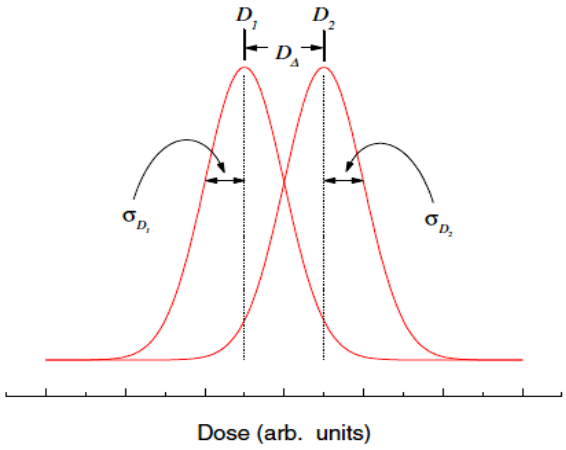

Figure 6.13 Calibration of irradiated vials [19].

From the above, it is clear that the performance of a technical display and the dosimeter can be estimated by determining the minimum dose differentiation. In this way it is possible to make a quantitative comparison between the different polymerization gel dosimeters as well as their different reading techniques. Also, optimizing the dose response of the dosimeter and the imaging protocol can lead to the lowest possible value of the discrete dose capacity.

Finally, the termination of the polymerization reaction due to the exposure of the dosing meter to oxygen at low doses and the saturation effects of the dosimeter at high doses are two possible factors that may cause D^{P}_{Δ} degradation.

d) Temporal and Spatial Stability

In order for a dosimeter to be reliable, it must be kept constant in time. There are two *types of stability* that characterize a dosimeter: temporal and spatial stability. The time stability is estimated by the rate of change of the *R2* rate over time, and has been studied for the various types of gel dosimeters [4, 20, 21, and 22]. The lower the rate of change of *R2* over time, the more stable the dosimeter is. Today, it is estimated that there are two phenomenons that affect the stability time of dosimeters. One reason is the continuance of the polymerization reaction in the dosimeter several hours after irradiation. The other cause is the *maturation* process or the continued gelation of gelatin or agarose (or more generally the gelation material of each solution). Studies have shown that this process continues even one month after irradiation. In order to avoid errors due to the n*on-time stability* of the dosimeters, it was proposed [4] to simultaneously read the verification model together with the calibration models.

The spatial stability of a dosimeter expresses the capacity of the dosimeter to keep the dose distribution constant. Several studies have shown the spatial variation of dose distribution in the dosimeter over time after irradiation [17, 23, and 24]. Nowadays, it is considered that the main cause of lack of spatial stability of the dosimeters is the diffusion of monomer molecules from high concentration regions to low concentration regions.

In particular, monomers react with polymer chains in areas where the absorbed dose is too high. This has the effect of creating an apparent excess of the expected *dose response* at specific points of the dosimeter. For this reason, polymer gel dosimeters should be used in a range of doses where no such overdoses occur. Therefore, when producing new polymer gel dosimeters, the *diffusion coefficients* of the monomers as well as the *lifetime* of the *polymer radicals* should be taken into account, in order to keep both as low as possible.

Finally, it has been suggested [25] that *diffusion* of monomers can be significantly reduced by using a suitable type of monomer molecules and molecules of "cross linking" substance, large in size, in order to diffuse at a very low rate.

e) Dose rate and Energy dependence

Several studies have reported that polymer gel dosimeters are independent of the dose *rate* [12]. However, dose dependence has been observed for specific types of gel dosimeters, such as *BANG-3* and *PAG* [26]. According to this study, by increasing the dose rate reduces the dose sensitivity. Dose rate dependence affects the outset of the polymerization reaction, affecting the concentration of the products produced during these reactions.

Today, we consider that polymer gel dosimeters are independent of the *radiation beam energy*. However, it has been reported, that dosimeters which contain monomeric molecules such as methacrylic acid, are dependent on the energy of the photon beam for doses greater than *10Gy*. This dependence is related to the *type* of monomer molecules used.

From the above, we conclude that polymer gel dosimeters, which are independent of the *dose rate* and the beam energy, can be considered as *reliable three-dimensional (3D) dosimeters* [26].

f) Temperature dependence during irradiation – Storage – Scanning

The *dose response* of a polymer gel dosimeter is particularly sensitive to changes in *temperature* during irradiation, *storage* and *scanning*. In 2002, the temperature changes of a dosimeter during its irradiation were presented [27]. This research suggested that temperature is another factor that affects the dose response of a dosimeter, and therefore needs special attention.

Another study also noted the importance of storing dosimeters before radiation and before scanning them [6]. In particular, it was suggested that dosimeters should be placed in environments that have room temperature 24 hours before irradiation and MR imaging, so that their temperature is constant and equal to that of the surrounding areas.

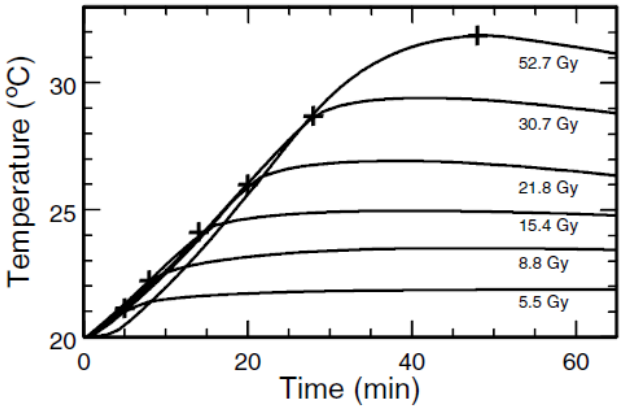

Figure 6.14 Temperature changes in the dosimeter depending on the absorbed dose [18].

Furthermore, when *MRI* is used as a reading method, it is necessary not to change the temperature of the dosimeter during its scan [18]. The use of high *RF* pulses during scanning can be absorbed by the dosimeter and cause a local increase in temperature. These changes in temperature across the dosimeter can lead to changes in the *R2* rate of the given dosimeter and eventually to an incorrect estimation of the recorded dose. For this reason, special care is needed, especially when it takes a long time to make three-dimensional maps and consequently a long scanning/reading time.

g) Tissue Equivalence

Since polymer gel dosimeters consist of 90% water, they can be considered to be equivalent to human tissue [28, 29, 30]. It has been noted that these dosimeters have a density that can be approximately 2% to 6% higher than that of water, which depends on the concentration range of molecules of the different monomers used and of gelatin [31, 32, and 33]. The equivalence of these tissue dosimeters is based on the fact that they do not contain atoms with high *Atomic numbers*.

For reliable results in clinical practice it is required that the dosimeters have physicochemical and geometrical properties similar to those of the patient. That is the reason why efforts have been made in recent years [34], to simulate heterogeneities in polymerization gel dosimeters, such as bone and lung.

h) Reproducibility

A polymer gel dosimeter is reliable when the dose measurements taken from it are repeatable. The *reproducibility* of the measurements is being tested between the *intra-batch* and *inter-batch* reproducibility areas. *Figure 6.15* shows the control of *intra-batch reproducibility*, where the *R2* rate was measured at 20 different points of the same dosimeter, which received the same dose [26].

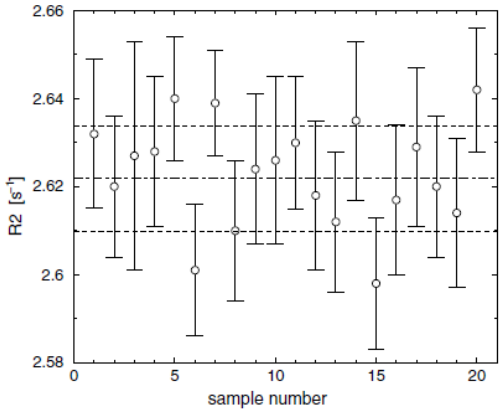

Figure 6.15 Reproducibility check of different areas of the same dosimeter [35].

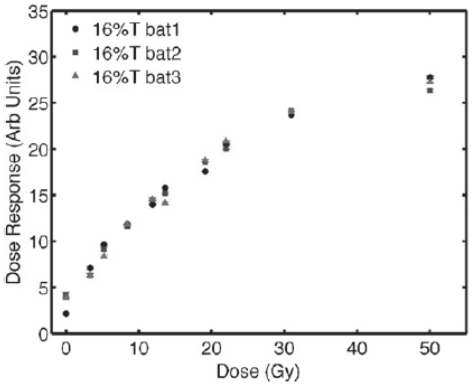

Figure 6.16 Test response of a dosimeter of three different batches, using CT [35].

The smaller the *standard deviation* of these measurements, the more reliable is the dosimeter. *Figure 6.16* also shows the repeatability of a dosimeter of three different batches using Computed Tomography [35]. In this study, the *dose response* of the dosimeter was determined three times, once for each batch.

6.9 Accuracy and precision of polymer gel dosimetry

The use of polymer gel dosimeters is a multi-stage dosimetry method. Specifically, it includes the manufacture of dosimeters, their storage, their reading/scanning process by a suitable imaging method, the analysis and the calibration of the images. Each of these stages adds *systematic* or *random errors* to the final result of the *dose distribution*.

6.9.1 Sources of error

In order to apply this method in clinical practice, it is necessary to identify all possible sources of dose uncertainty and to take into account the final estimation of dose distribution [36]. In the following paragraph, the main sources of uncertainty in determining dose after irradiation are reported [10].

a. Differences in dose response between the verification and calibration phantom.

Several groups of researchers have reported dose deviations between the calibration vials and the verification phantom, which belong to the same batch of gel solution. This phenomenon can be explained by several possible factors. It has also been noted that differences in temperature when storing large volumes of phantoms in a refrigerator [8], causes differences in dose response and leads to systematic errors.

b. Lack of chemical stability.

There are two types of non-chemical stability for gel dosimeters. The first type is related to the continuation of the polymerization reaction after irradiation and affects the slope of dose response. The second type is related to the continued gelation of gelatin and causes an increase in *R2* rate values. These chemical instabilities also depend on the type of monomer used in the dosimeter. Their minimization is achieved by simultaneously reading the calibration and verification phantoms.

c. Lack of spatial stability.

The lack of spatial stability is due either to the diffusion of the monomer molecules from high-absorbed dose regions to low-absorbed dose regions, or to the presence of oxygen molecules in the solution. These differences in dose response occur after irradiation and affect the assessment of dose distribution. In 2004 a mathematical model was presented, which describes and evaluates these changes, but can only be applied to PAG dosimeters [23].

d. Installation errors of calibration phantoms.

Incorrect placement of the phantoms when scanning them (MR Imaging) can lead to an error in estimating the dose. This error leads to an error in the calibration curve of the dosimeter and consequently to a systematic error in estimating the dose distribution.

e. Temperature dependence during irradiation and imaging.

It has been observed that in some types of gel dosimeters, changes in temperature during irradiation affect their response to dose [37]. One possible explanation is that as the temperature increases, the diffusion coefficients of the monomer molecules change, resulting in a change in the

kinetic behavior of these molecules in the gelatin solution. It has also been reported that reading dosimeters by using *MRI*, changes the temperature to its extent. Specifically, with increasing temperature, the *R2* rate changes and therefore the dose response changes. This effect can be reduced by carefully selecting the parameters of the reading sequence, in a way that will not cause an increase in the temperature of the dosimeter.

f. Effect of bottle wall material.

To prevent oxygen from entering through the walls of the phantoms, the vials are usually made of glass or materials that are equivalent to human tissue. Also special attention should be paid in the case of glass vials. If they consist of large atomic numbers, there is a possibility that the beam passes through them, causing *beam hardening*.

g. Image Document Size Dosage from the Imaging Technique.

The dose estimation from parametric maps is related to the size of the pixels of the maps, each of which contains information from specific data of the volume of interest. Specifically, the signal of each pixel is the total signal from several measurements over time of the same volume element. In most cases, the signal of each pixel contains information from other elements of the volume around the element of interest. In MRI, the size of the elementary volume is determined by the range of the receiving coil and the slice thickness. In cases where high spatial resolution is required, the selection of an elementary volume size is very important.

h. Imaging Artifacts.

The presence of image artifacts can degrade the dose value in each elementary region. These "pseudo-icons" can be connected to either the phantom or the imaging device. The ones connected to the reading/imaging device come from machine malfunctions and the ones related to the phantom come from the gel solution. Also, the "pseudo-icons" associated with the reading device depend on the shape of the phantom and it is difficult to determine the accuracy of this measurement. Usually a large phantom or a phantom with sharp edges can be depicted differently from a cylindrical or spherical phantom. In addition, "pseudo-images" derived from the dosimeter itself are mainly due to temperature differences during the imaging/scanning process or due to the diffusion of monomers.

References

1. Baldock C, Burford RP, Billingham N, et al. Experimental procedure for the manufacture and calibration of polyacrylamide gel (PAG) for magnetic resonance imaging (MRI) radiation dosimetry. *Phys Med Biol*. 1998;43(3):695-702. doi:10.1088/0031-9155/43/3/019
2. Gustavsson H, Bäck SA, Lepage M, Rintoul L, Baldock C. Development and optimization of a 2-hydroxyethylacrylate MRI polymer gel dosimeter. Phys Med Biol. 2004;49(2):227-241. doi:10.1088/0031-9155/49/2/004
3. Senden RJ, De Jean P, McAuley KB, Schreiner LJ. Polymer gel dosimeters with reduced toxicity: a preliminary investigation of the NMR and optical dose-response using different monomers. Phys Med Biol. 2006;51(14):3301-3314. doi:10.1088/0031-9155/51/14/001
4. Baldock C, De Deene Y, Doran S, et al. Polymer gel dosimetry. Phys Med Biol. 2010;55(5):R1-R63. doi:10.1088/0031-9155/55/5/R01
5. Fong PM, Keil DC, Does MD, Gore JC. Polymer gels for magnetic resonance imaging of radiation dose distributions at normal room atmosphere. Phys Med Biol. 2001;46(12):3105-3113. doi:10.1088/0031-9155/46/12/303
6. Bayreder C, Georg D, Moser E, Berg A. Basic investigations on the performance of a normoxic polymer gel with tetrakis-hydroxy-methyl-phosphonium chloride as an oxygen scavenger: reproducibility, accuracy, stability, and dose rate dependence. Med Phys. 2006;33(7):2506-2518. doi:10.1118/1.2208741
7. De Deene Y, Hanselaer P, De Wagter C, Achten E, De Neve W. An investigation of the chemical stability of a monomer/polymer gel dosimeter. Phys Med Biol. 2000;45(4):859-878. doi:10.1088/0031-9155/45/4/304
8. De Deene Y, Pittomvils G, Visalatchi S. The influence of cooling rate on the accuracy of normoxic polymer gel dosimeters. Phys Med Biol. 2007;52(10):2719-2728. doi:10.1088/0031-9155/52/10/006
9. De Deene, Yves. (2010). How to scan polymer gels with MRI?. Journal of Physics: Conference Series. 250. 012015. 10.1088/1742-6596/250/1/012015.
10. Baldock C, De Deene Y, Doran S, et al. Polymer gel dosimetry. Phys Med Biol. 2010;55(5):R1-R63. doi:10.1088/0031-9155/55/5/R01
11. Maryanski MJ, Gore JC, Kennan RP, Schulz RJ. NMR relaxation enhancement in gels polymerized and cross-linked by ionizing radiation: a new approach to 3D dosimetry by MRI. Magn Reson Imaging. 1993;11(2):253-258. doi:10.1016/0730-725x(93)90030-h
12. De Deene Y, Baldock C. Optimization of multiple spin-echo sequences for 3D polymer gel dosimetry. Phys Med Biol. 2002;47(17):3117-3141. doi:10.1088/0031-9155/47/17/306
13. De Deene Y, De Wagter C, De Neve W, Achten E. Artefacts in multi-echo T2 imaging for high-precision gel dosimetry: I. Analysis and compensation of eddy currents. Phys Med Biol. 2000;45(7):1807-1823. doi:10.1088/0031-9155/45/7/307
14. De Deenet Y, De Wagter C, De Neve W, Achten E. Artefacts in multi-echo T2 imaging for high-precision gel dosimetry: II. Analysis of B1-field inhomogeneity. Phys Med Biol. 2000;45(7):1825-1839. doi:10.1088/0031-9155/45/7/308
15. De Deene Y, De Wagter C. Artefacts in multi-echo T2 imaging for high-precision gel dosimetry: III. Effects of temperature drift during scanning. Phys Med Biol. 2001;46(10):2697-2711. doi:10.1088/0031-9155/46/10/312
16. Oldham M, McJury M, Baustert IB, Webb S, Leach MO. Improving calibration accuracy in gel dosimetry. Phys Med Biol. 1998;43(10):2709-2720. doi:10.1088/0031-9155/43/10/002
17. De Deene Y, Vergote K, Claeys C, De Wagter C. The fundamental radiation properties of normoxic polymer gel dosimeters: a comparison between a methacrylic acid based gel and acrylamide based gels. Phys Med Biol. 2006;51(3):653-673. doi:10.1088/0031-9155/51/3/012

18. De Deene Y, Hanselaer P, De Wagter C, Achten E, De Neve W. An investigation of the chemical stability of a monomer/polymer gel dosimeter. Phys Med Biol. 2000;45(4):859-878. doi:10.1088/0031-9155/45/4/304

19. Gustavsson H, Bäck SA, Lepage M, Rintoul L, Baldock C. Development and optimization of a 2-hydroxyethylacrylate MRI polymer gel dosimeter. Phys Med Biol. 2004;49(2):227-241. doi:10.1088/0031-9155/49/2/004

20. McJury M, Oldham M, Leach MO, Webb S. Dynamics of polymerization in polyacrylamide gel (PAG) dosimeters: (I) ageing and long-term stability. Phys Med Biol. 1999;44(8):1863-1873. doi:10.1088/0031-9155/44/8/301

21. Venning AJ, Hill B, Brindha S, Healy BJ, Baldock C. Investigation of the PAGAT polymer gel dosimeter using magnetic resonance imaging. Phys Med Biol. 2005;50(16):3875-3888. doi:10.1088/0031-9155/50/16/015

22. Vienning A, Healy B, Nitschke K and Baldock C 2005 Investigation of the MAGAS normoxic polymer gel dosimeter with Pyrex glass walls for clinical radiotherapy dosimetry *Nuclear Instruments and Methods in Physics Research A* **555** 396-402

23. Vergote K, De Deene Y, Vanden Bussche E, De Wagter C. On the relation between the spatial dose integrity and the temporal instability of polymer gel dosimeters. Phys Med Biol. 2004;49(19):4507-4522. doi:10.1088/0031-9155/49/19/005

24. De Deene Y, Hurley C, Venning A, et al. A basic study of some normoxic polymer gel dosimeters. Phys Med Biol. 2002;47(19):3441-3463. doi:10.1088/0031-9155/47/19/301

25. McAuley, Kimberley. (2004). The chemistry and physics of polyacrylamide gel dosimeters: Why they do and don't work. Journal of Physics: Conference Series. 3. 10.1088/1742-6596/3/1/005.

26. DeDeene Y 2004 Essential characteristics of polymer gel dosimeters *J. Phys.: Con. Ser.* **3** 34-57

27. Salomons GJ, Park YS, McAuley KB, Schreiner LJ. Temperature increases associated with polymerization of irradiated PAG dosimeters. Phys Med Biol. 2002;47(9):1435-1448. doi:10.1088/0031-9155/47/9/301

28. Baldock C et al 1996 Energy response and tissue equivalence of polymer gels for radiation dosimetry by MRI *Proceedings of European Society for Magnetic Resonance in Medicine and Biology*

29. Keal P and Baldock C 1998 Radiological properties and water equivalence of dosimetry gels *Med Phys* **25** 194

30. Rousselle I et at 1999 Tissue equivalence of dosimeter gels: case of brain phantoms irradiated with photons *DOSGEL99*

31. Hilts M, Jirasek A, Duzenli C. Effects of gel composition on the radiation induced density change in PAG polymer gel dosimeters: a model and experimental investigations. Phys Med Biol. 2004;49(12):2477-2490. doi:10.1088/0031-9155/49/12/001

32. Venning AJ, Nitschke KN, Keall PJ, Baldock C. Radiological properties of normoxic polymer gel dosimeters. Med Phys. 2005;32(4):1047-1053. doi:10.1118/1.1881812

33. Venning AJ, Nitschke KN, Keall PJ, Baldock C. Radiological properties of normoxic polymer gel dosimeters. Med Phys. 2005;32(4):1047-1053. doi:10.1118/1.1881812

34. De Deene, Y., Vandecasteele, J., & Vercauteren, T. (2013). Low-density polymer gel dosimeters for 3D radiation dosimetry in the thoracic region: A preliminary study. Journal of Physics: Conference Series, 444(1), 1-4. [012026]. https://doi.org/10.1088/1742-6596/444/1/012026

35. Jirasek A, Hilts M, Berman A, McAuley KB. Effects of glycerol co-solvent on the rate and form of polymer gel dose response. Phys Med Biol. 2009;54(4):907-918. doi:10.1088/0031-9155/54/4/006

36. Baldock C, Murry P, Kron T. Uncertainty analysis in polymer gel dosimetry. Phys Med Biol. 1999;44(11):N243-N246. doi:10.1088/0031-9155/44/11/402

37. Jordan K, Avvakumov N. Radiochromic leuco dye micelle hydrogels: I. Initial investigation. Phys Med Biol. 2009;54(22):6773-6789. doi:10.1088/0031-9155/54/22/002

38. Hilts M, Audet C, Duzenli C, Jirasek A. Polymer gel dosimetry using x-ray computed tomography: a feasibility study. Phys Med Biol. 2000;45(9):2559-2571. doi:10.1088/0031-9155/45/9/309

39. Pappas, Evangelos & Seimenis, Ioannis & Angelopoulos, Angelos & Georgolopoulou, P & Kamariotaki-Paparigopoulou, M & Maris, Thomas & Sakelliou, L & Sandilos, Panagiotis & Vlachos, L. (2001). Narrow stereotactic beam profile measurements using N-vinylpyrrolidone based polymer gels and magnetic resonance imaging. Physics in medicine and biology. 46. 783-97. 10.1088/0031-9155/46/3/313.

40. Pappas E, Petrokokkinos L, Angelopoulos A, et al. Relative output factor measurements of a 5 mm diameter radiosurgical photon beam using polymer gel dosimetry. Med Phys. 2005;32(6):1513-1520. doi:10.1118/1.1916048

41. Pappas E, Maris TG, Papadakis A, et al. Experimental determination of the effect of detector size on profile measurements in narrow photon beams. Med Phys. 2006;33(10):3700-3710. doi:10.1118/1.2349691

42. Pappas E, Maris TG, Zacharopoulou F, et al. Small SRS photon field profile dosimetry performed using a PinPoint air ion chamber, a diamond detector, a novel silicon-diode array (DOSI), and polymer gel dosimetry. Analysis and intercomparison. Med Phys. 2008;35(10):4640-4648. doi:10.1118/1.2977829

43. Pantelis E, Antypas C, Petrokokkinos L, et al. Dosimetric characterization of CyberKnife radiosurgical photon beams using polymer gels. Med Phys. 2008;35(6):2312-2320. doi:10.1118/1.2919099

44. Kipouros P, Pappas E, Baras P, et al. Wide dynamic dose range of VIPAR polymer gel dosimetry. Phys Med Biol. 2001;46(8):2143-2159. doi:10.1088/0031-9155/46/8/308

45. Karaiskos P, Petrokokkinos L, Tatsis E, et al. Dose verification of single shot gamma knife applications using VIPAR polymer gel and MRI. Phys Med Biol. 2005;50(6):1235-1250. doi:10.1088/0031-9155/50/6/013

46. Papagiannis P, Pappas E, Kipouros P, et al. Dosimetry close to an 192Ir HDR source using N-vinylpyrrolidone based polymer gels and magnetic resonance imaging. Med Phys. 2001;28(7):1416-1426. doi:10.1118/1.1382603

47. De Deene Y, De Wagter C, Van Duyse B, Derycke S, De Neve W, Achten E. Three dimensional dosimetry using polymer gel and magnetic resonance imaging applied to the verification of conformal radiation therapy in head-and-neck cancer. Radiotherapy and Oncology1998;48:238-291. https://doi.org/10.1016/S0167-8140(98)00087-5

48. https://www.imaios.com/en/e-Courses/e-MRI

49. Ibbott, G. S., Attix, F. H., Slowey, T. W., Fontenla, D. P., & Rozenfeld, M. (1997). Uncertainty of calibrations at the accredited dosimetry calibration laboratories. Medical physics, 24(8), 1249–1254. https://doi.org/10.1118/1.598146

50. Ramm, U., Weber, U., Bock, M., Krämer, M., Bankamp, A., Damrau, M., Thilmann, C., Böttcher, H. D., Schad, L. R., & Kraft, G. (2000). Three-dimensional BANG gel dosimetry in conformal carbon ion radiotherapy. Physics in medicine and biology, 45(9), N95–N102. https://doi.org/10.1088/0031-9155/45/9/401

Experimental Part

7. Purpose of the study

The *purpose* of this thesis is to manufacture a *new polymer gel dosimeter* and compare it with a *reference* gel. More specifically, to compare with a widespread and used gel, the *VIPET* gel [1]. The role of the different constituent chemicals is investigated. The concentration of the different chemicals was varied and the response of the gel upon irradiation investigated. It is shown that other chemicals may also be used to scavenge oxygen with different reaction rates for the various anti-oxidants observed. The new polymer gel dosimeter (named *VIPASCU*) consists of the same monomers as the *VIPET* gel, except from its oxygen scavenger.

The importance of the study is based on the optimization of the quality of the therapeutic results during conformal radiotherapy, while using Magnetic Resonance Imaging in polymer gel dosimeters. In particular, in conformal Radiotherapy, the audit of dose distributions in three dimensions (3D) plays a particularly important role. As for very small tumors, the precise determination of the target tumor is also very important. It is necessary to find a reliable dosimetry method, which controls the dose distribution in three dimensions with the highest possible accuracy, in order to ensure the quality of the dosimetric results. It is also very important to find a software tool that allows you to merge images of different imaging techniques to determine accurately the target volume.

The use of dosimetry gels has the potential to provide high-resolution measurements of dose in modern radiotherapy technique to verify dose distributions. Furthermore, use of dosimetry gels minimizes the disadvantages of volume averaging, non-water equivalence or need for dose perturbation correction.

In order to verify the results, different manufacturing batches were investigated. The results can be used to improve quantitative dosimetric results in polymer gel dosimetry based on VIPET-type polymer gels and also offer recommendations for polymer gels with similar dose rate dependence [2]. Data which show the impact of different concentrations of oxygen scavengers on the dose rate dependence of the dose response is presented. The dose response was determined over a large dose range (D = 0 Gy to D = 64 Gy) using parameter selective MR-imaging based on the relaxation rate R2 = 1/T2. The dose sensitivity, defined as slope $\boldsymbol{\Delta R2/\Delta D}$ within the range of linear dose response, was evaluated. In order to verify our results, we investigated different manufacturing batches.

Moreover, a statistical software (*MedCalc*) was used for a *Regression analysis (Scatter diagram & regression line)* between the small and the big vials of the different chemistry batches. Regression analysis is a statistical method used to describe the relationship between two variables and to predict one variable from another.

Finally, it is well known that the performance of a polymer gel dosimeter cannot be assessed based on the R2-dose sensitivity alone (*Baldock et al 1999a, 1999b, 2001, Lepage et al 2001a, De Deene 2004a, 2004b*). Numerous parameters need to be considered such as spatial and temporal stability, edge response and dose resolution, which requires the properties of the dosimeter to be coupled with the ability of the measurement technique to provide low uncertainties (*Baldock et al 2001, Lepage et al 2001a*). So, the dose resolution of the "best" *VIPASCU* gel composition, according to the experiments outcomes, was compared to the VIPET gel's dose resolution.

References

1. Papoutsaki, M. V., Maris, T. G., Pappas, E., Papadakis, A. E., & Damilakis, J. (2013). Dosimetric characteristics of a new polymer gel and their dependence on post-preparation and post-irradiation time: effect on X-ray beam profile measurements. Physica medica : PM : an international journal devoted to the applications of physics to medicine and biology : official journal of the Italian Association of Biomedical Physics (AIFB), 29(5), 453–460. https://doi.org/10.1016/j.ejmp.2013.01.003
2. Khan M, Heilemann G, Kuess P, Georg D, Berg A. The impact of the oxygen scavenger on the dose-rate dependence and dose sensitivity of MAGIC type polymer gels. Phys Med Biol. 2018;63(6):06NT01. Published 2018 Mar 12. doi:10.1088/1361-6560/aab00b

8. Materials and methods

8.1 Manufacturing of polymer gels

The manufacture procedure of the polymer gel dosimeters took place in the chemical laboratory of Medical Physics, which is housed in the Medicine Department of University of Crete (UOC). The polymer gel dosimeters were manufactured using gelatin, water and ascorbic acid together with copper-sulfate as an oxygen scavenger in chemical laboratory with standard equipment under normoxic conditions.

VIPASCU gel

Three batches of VIPASCU gel (further referred to as *Batch (A)*, *Batch (B)*, and *Batch (C)*) with different concentrations of *oxygen scavenger* were manufactured. *Table 3* provides a list of the different gel compositions that have been made.

Table 3. Monomer Components and Concentrations of the VIPASCU gel compositions

VIPASCU gel				
Batch (A)				
Monomer Components	VIPASCU(1)	VIPASCU(2)	VIPASCU(3)	
	Concentration range			
Gelatin	5 % w/w	5 % w/w	5 % w/w	
Vinyl	6 % w/v	6 % w/v	6 % w/v	
Bis	4 % w/v	4 % w/v	4 % w/v	
Distilled water	85 % w/v	85 % w/v	85 % w/v	
Ascorbic acid	**0.2 mM**	**1 mM**	**5 mM**	
Copper(II) sulfate pentahydrate	***0.01 mM***	***0.01 mM***	***0.01 mM***	
Batch (B)				
Monomer Components	VIPASCU(4)	VIPASCU(5)	VIPASCU(6)	
	Concentration range			
Gelatin	5 % w/w	5 % w/w	5 % w/w	
Vinyl	6 % w/v	6 % w/v	6 % w/v	
Bis	4 % w/v	4 % w/v	4 % w/v	
Distilled water	85 % w/v	85 % w/v	85 % w/v	
Ascorbic acid	**0.1 mM**	**0.2 mM**	**0.3 mM**	
Copper(II) sulfate pentahydrate	***0.00016 mM***	***0.00016 mM***	***0.00016 mM***	
Batch (C)				
Monomer Components	VIPASCU(7)	VIPASCU(8)	VIPASCU(9)	VIPASCU(10)
	Concentration range			
Gelatin	5 % w/w	5 % w/w	5 % w/w	5 % w/w
Vinyl	6 % w/v	6 % w/v	6 % w/v	6 % w/v
Bis	4 % w/v	4 % w/v	4 % w/v	4 % w/v
Distilled water	85 % w/v	85 % w/v	85 % w/v	85 % w/v
Ascorbic acid	**0.2 mM**	**0.2 mM**	**0.2 mM**	**0.2 mM**
Copper(II) sulfate pentahydrate	***0 mM***	***1.5 mM***	***3 mM***	***5 mM***

As observed in *Table 3*, the concentration of *Ascorbic Acid* was varied from *0.2 mM to 5 mM*. Furthermore, the concentration of its cosolvent, *Copper (II) sulfate pentahydrate*, was also tested and varied from *0mM to 5mM*.

All gels were prepared under *normoxic conditions*, using a *custom-made construction* made by Prof. Maris and his team. This construction consists of a large, glass cylindrical vial which vacuum seals with an acrylic cover, made from a 3D printer. This cover has a *pressure meter*, two tubes and a twist-off cap, as seen in *Figure 8.1*.

Gelatin was slowly added to distilled water and was heated up to approximately 50°C under continuous magnetic stirring. After approximately 45min the gelatin had been completely dissolved, leaving a clear solution. After that, the solution was then put into a water bath until it cooled down to approximately 35°C and then first *vinyl* and then *bisacrylamide* were also added, making sure that each of them were dissolved in the solution. Finally, *ascorbic acid* and *copper sulfate* were added to the gel. The solution was mixed at high blending speed, until a clear solution with a beautiful light cyan color.

Figure 8.1 Custom-made construction where the gels were manufactured.

The monomers were inserted through the twist-off cap. Each time the cap was opened, argon gas was added through the white tube, in order to ensure the glass vial was kept under normoxic conditions. The use of argon to remove oxygen from the gel solution is necessary to avoid unwanted inhibition of gel polymerization. The effect of oxygen on the dose sensitivity of the polymer gels has been presented by a number of groups. [1, 2, 3]

The white tube continues to the bottom of the vial and a thermometer is attached to it, to have a real-time temperature awareness of the gel solution. When the desired solution was ready, argon gas was inserted through the blue tube, while checking the pressure meter, in order to transfer the gel

solution through the white tube into sealed cylindrical glass vials. All gels were poured in cylindrical plexiglass vials. The vials were filled up to the top to avoid any additional oxygen coming into contact with the gel. Then, the vials were tightly sealed with their caps and parafilm foil to block oxygen infusion [2].

Eventually, each batch consisted of:

- **Batch A**: Three additional compositions of the *VIPASCU gel solution*, **VIPASCU(1)**, **VIPASCU(2)** and **VIPASCU(3)** were manufactured, with different concentrations of Ascorbic Acid (0.2 mM, 1 mM and 5 mM) and a *Copper(II) sulfate pentahydrate* concentration equal to *0.01mM*, following an identical procedure to investigate the inter-batch variability. Each composition consisted of one big cylindrical plexiglass vial (100 ml) and six small cylindrical plexiglass vials (20 ml), as shown in *Figure 8.2*.

Figure 8.2 *Batch A* of VIPASCU gel, consisted of big and small vials.

- **Batch B**: Three compositions of the *VIPASCU gel solution*, **VIPASCU(4)**, **VIPASCU(5)** and **VIPASCU(6)** were manufactured, with different concentrations of Ascorbic Acid (0.1 mM, 0.2 mM and 0.3 mM) and a *Copper(II) sulfate pentahydrate* concentration equal to *0.00016mM*. In this batch, only 3 *big* vials were filled for each composition.

- **Batch C**: Four compositions of the *VIPASCU gel solution*, **VIPASCU(7)**, **VIPASCU(8)**, **VIPASCU(9)** and **VIPASCU(10)** were manufactured, with different concentrations of *Copper(II) sulfate pentahydrate* (0 mM, 1.5 Mm, 3 mM and 5 mM) and a concentration of Ascorbic acid equal to *0.2 mM*. In this batch, only 4 *big* vials were filled for each composition.

VIPET gel

The gel dosimeter used here had a gelatin content of 5% weight fraction (wf). This is to be compared with the usual VIPAR gel composition, first presented by *Pappas et al (1999)* [3]. Besides, the modified VIPAR gel composition constitutes a mixture of the monomer N-vinylpyrrolidone (VIPE) in 6% wf, the cross-linker N,N-methylenebisacrylamide (bis) in 4% wf, the gelatin in 5% wf, and double-distilled deionized water in 85% wf. VIPET gel was also manufactured in normoxic conditions, using the custom-made construction described above. The monomer components of *VIPET* gel, as well as their concentrations are presented in *Table 4*.

Table 4. Monomer Components and Concentrations of VIPET

VIPET	
Monomer Components	**Concentration range**
Gelatin	5 % w/w
Vinyl	6 % w/v
Bis	4 % w/v
Distilled water	85 % w/v
THPC	**7 mM**

The manufacturing procedure was performed as follows: the gelatin was added to the double-distilled deionized water at room temperature (25 ◦C) and allowed to dissolve. The solution was then heated to *50 ◦C* and once the temperature was stabilized the bis was added. Heating was achieved through a hot-plate and stirring unit. When the solution became transparent and obtained a champagne color, about 30 min later, the mixture was cooled down to approximately *35◦C* and then vinyl was added. Once the constituents were completely dissolved after about 5 min, the oxygen scavenger THPC was added in the solution.

THPC constituent is a clear colorless solution at 80% in water. Care was taken to keep the temperature above 32 ◦C and avoid solidification of the solution. Three minutes after the addition of THPC the gel was transferred to the glass vial.

After manufacture, all the phantoms (vials) were refrigerated, in the absence of light, to cool down and coagulate at approximately 10 °C, 48h before irradiation. The phantoms were positioned upright, to minimize possible air bubbles.

Therefore, two additional batches of *the VIPET gel solution*, **VIPET(1)** and **VIPET(2)**, were manufactured, following an identical procedure to investigate the inter-batch variability.

Each batch consisted of:

- **VIPET(1)**: This batch of VIPET gel, consisted of one big cylindrical plexiglass vial (100 ml) and six small cylindrical plexiglass vials (20 ml).
- **VIPET(2)**: In this batch, only 1 *big* vial of the same composition was filled.

The *VIPET(1)* batch was manufactured along with *VIPASCU* gel *batch A*, using it as a reference gel) for making a comparison between them. Likewise, *VIPET(2)* was manufactured along with VIPASCU gel *batch B*, using it as a reference gel) for making a comparison between them.

8.2 Irradiation of Polymer gel dosimeters

The phantoms were irradiated in a 6 MV medical linear accelerator (LINAC) at the University Hospital of Heraklion (PAGNI), under the guidance of Prof. Mazonakis. The irradiation was carried out in a specific way in order to save time due to the big number of the vials, by irradiating the VIPASCU gel (Batch (A), Batch (B) and Batch (C)) and the VIPET gel (VIPET(1), VIPET(2)) batches.

The irradiation was performed in three different batches in three subsections (*Figure 8.3*):

- The *first irradiation setup* was used for information on the range of the linear dose response and calibration of the big and small vials of *VIPASCU gel Batch A* and the first *VIPET gel batch, VIPET(1),* (see section 8.2.1) for a standard dose range from D˙ = 0 Gy to D=32 Gy.
- The *second irradiation setup* was aiming on the quantitative dependence of the dose response on dose rate and in addition, as a second parameter, the influence of the oxygen scavenger concentration (section 8.2.2) of *VIPASCU gel: Batch B* and *VIPET(2) batch*, while increasing the dose range from D = 0 Gy to D = 64 Gy.
- The *third irradiation setup* represented mainly a reproducibility check of results, using the same procedure and manufacturing ingredients, but this time, as a third parameter, the influence of the oxygen scavenger's cosolvent (*Copper(II) sulfate pentahydrate*) concentration was tested, using concentrations from *0mM to 5mM (VIPASCU gel: Batch C)*. The concentration of the oxygen scavenger (*Ascorbic Acid*) was selected based on the two previous setups, while having a dose range from D = 0 Gy to D = 64 Gy.

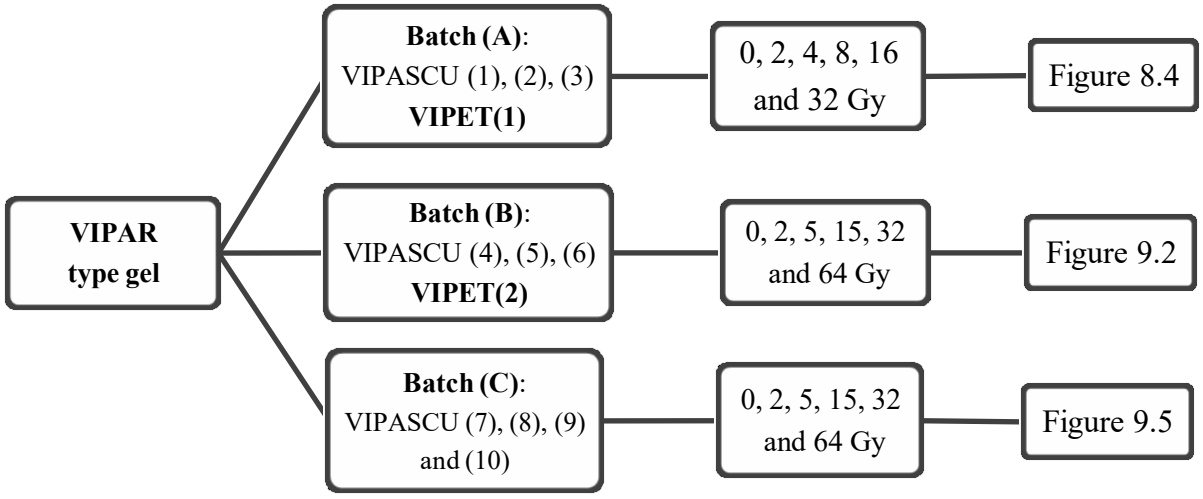

Figure 8.3 Scheme of irradiation procedure for calibration and evaluation of the dose-rate effect, while testing the concentration of *Ascorbic Acid* and its cosolvent *Copper (II) sulfate pentahydrate*.

8.2.1 Calibration of gels

A set of three different gel compositions (VIPASCU(1), VIPASCU(2) and VIPASCU(3)) from Batch A, along with a *VIPET(1) gel* batch, were irradiated 1 d after manufacturing with various dose levels (0, 2, 4, 8, 16 and 32 Gy) (28 gels). The vials were properly positioned within a $20x20\ cm^2$ radiation field at a distance of 100 cm (*SSD*) from the source and received doses from 0 Gy to 32 Gy, after MU calculations, to obtain the dose response as calibration curve for each type of gel (*Figures 8.3 and 8.4*).

The *big* vials were administered a different dose along their axis. Each time a dose was administered the radiation field was kept stable and the radiation bed was moved in order to create a different dose range along the axis of the big vials. As for the small vials, each time a different dose was administered, a small vial was removed. This procedure was repeated five times, for 2, 4, 8, 16 Gy, when finally only one small vial was left at 32 Gy.

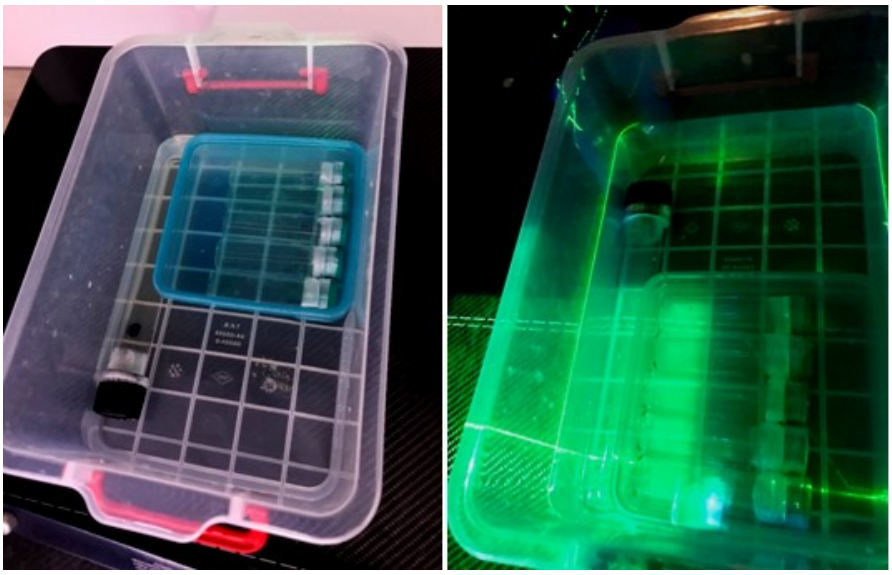

Figure 8.4 Irradiation and placement method of batches: *Batch A* (*VIPASCU*) and *VIPET(1).*

A *scatter diagram*, including a *regression line* for all big and small vials of batches VIPASCU (1), VIPIASCU (2), VIPASCU (3) and VIPET (1) was made and is presented in *Figure 8.5*. The R2 values of the small vials of the same chemistry of each batch were compared with the R2 values of the big vials of the same chemistry of each batch. Two curves are drawn next to the regression line. These curves represent a *95% confidence interval* for the regression line. This interval includes the *true regression line with 95% probability.* Also a *Heat map* is displayed, where background color coding indicates density of points, suggesting clusters of observations.

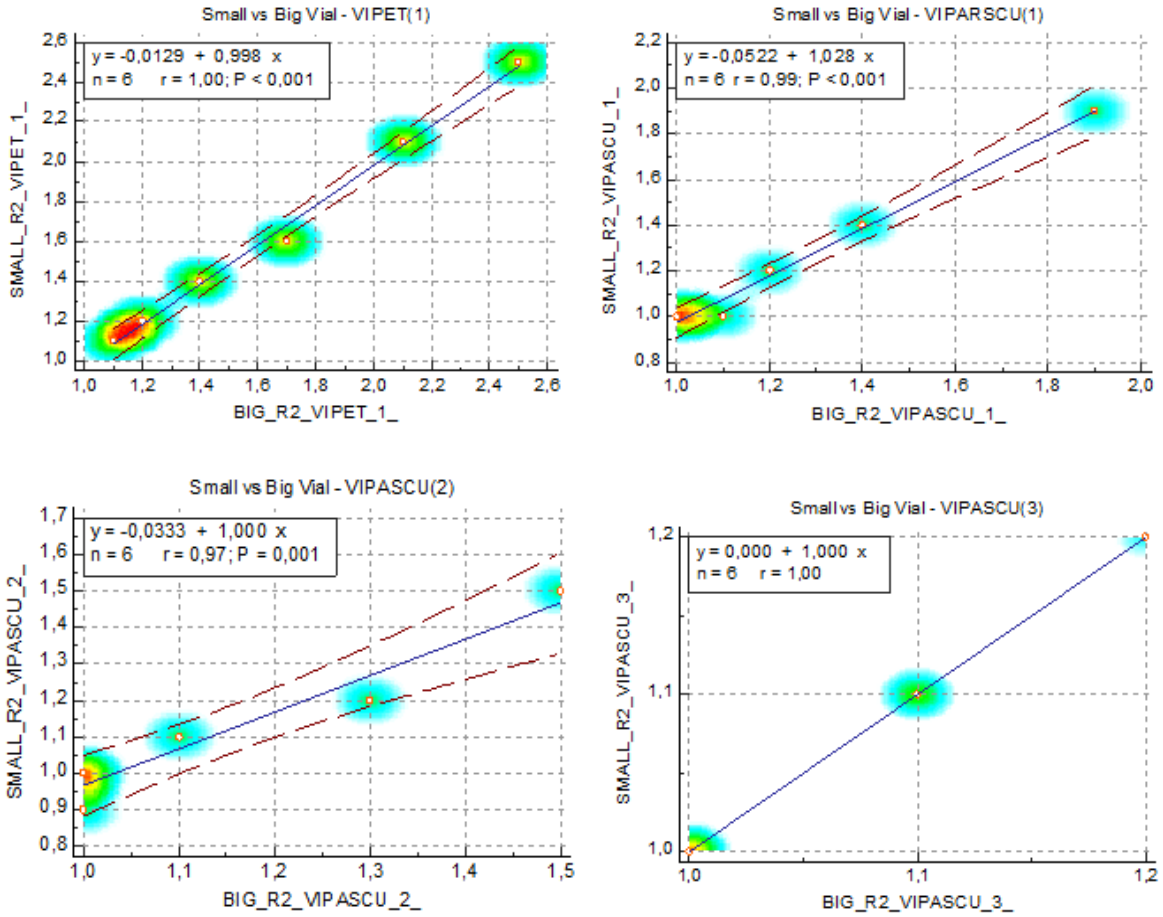

Figure 8.5 Scatter diagram & regression line for R2 value comparison of the big and small vials of Batch A of VIPASCU gel and VIPET (1) batch of VIPET gel.

After irradiation, it was observed that the mean R2 values of the big vials are slightly higher (*smaller T2 value*) than the R2 values of the small vials, so for convenience reasons, in the next experiments *only big vials will be used* from now on.

The dose response curve for the calibration of big vials of *Batch A* of *VIPASCU* gel and batch *VIPET(1)* of *VIPET* gel is presented in *Figure 8.6* below.

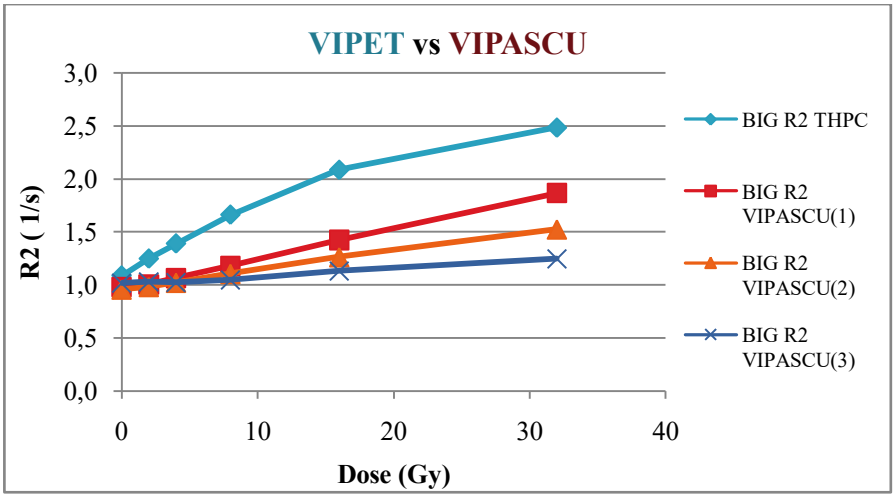

Figure 8.6 **(Batch A)** Dose response for the reference polymer gels (big vials) for calibration with different concentrations of oxygen scavenger. VIPASCU(1) featured minimum ($Casc.acid = 0.2\,mM$) and VIPASCU(3) ($Casc.acid = 5\,mM$) maximum concentration of ascorbic acid, while keeping a standard Copper (II) sulfate pentahydrate concentration ($C_{copper} = 0.01\,mM$).

8.2.2 Dose rate effect

The results from the first irradiation setup of *Batch A* were taken into account for slightly modifying the protocol for *Batch B,* for a more detailed investigation in the high dose rate range and the oxygen scavenger concentration, this time using *only big vials*. The high dose rate range was investigated more densely and the maximum dose rate was extended ($D_{min} = 0\,Gy\,min^{-1} = 0, D_{max} = 64\,Gy\,min^{-1}$). We investigated three different dose levels: low, medium and high, with a maximum dose of 32 and 64 Gy.

Then, Batch (B) of VIPASCU gel, along with the *second* VIPET gel composition, VIPET (2), and finally Batch (C) of VIPASCU gel, were irradiated. The phantoms received doses from 0 Gy to 64 Gy this time, since it was observed that VIPASCU gel had high dose sensitivity with a linear dose response up to 32 Gy and a greater dynamic range. The vials were properly positioned within a $20x20\ cm^2$ radiation field at a distance of 100 cm (*SSD*) from the source, as seen in *Figure 8.7a*, and were administered a different dose along their axis. Each time a dose was administered the radiation field was kept stable and the radiation bed was moved in order to create a different dose range along the axis of the big vials. This procedure was repeated five times, for 2, 5, 15, 32 and finally 64 Gy.

Also, all the vials were covered with a water equivalent material, 3 cm thick (bolus) to achieve electronic balance and to avoid plexiglass inhomogeneities (plexiglass vial density: $2.3\,{}^{gr}/_{cm^3}$), which where took into account. All irradiated gels exhibited an increase in optical turbidity with dose. Exposure of a polymer gel onto ionizing radiation causes polymerization and crosslinking of its ingredients only in the irradiated part. This effect is naked eye visible since the irradiated part becomes opaque after absorbing a threshold dose, as seen in *Figure 8.7b*.

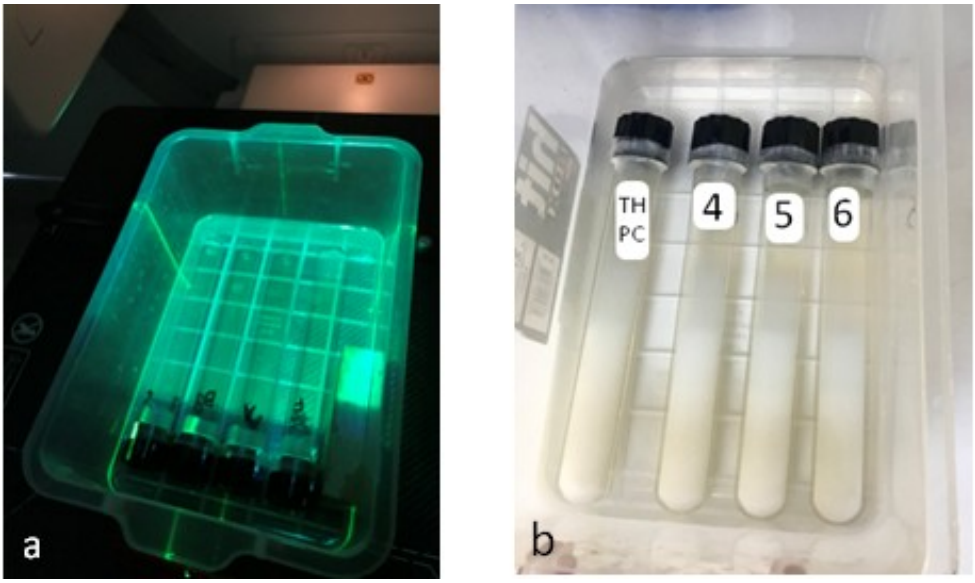

Figure 8.7 Irradiation placement method and post irradiation picture of the batches.

After irradiation, the phantoms were kept in a room temperature area, in the absence of light, 24 hours before MR Imaging.

8.3 MRI measurements

The irradiated phantoms were measured using the Magnetic Resonance Imaging system of PAGNI Hospital (Vision / Sonata, Siemens, Germany), of *1.5 T intensity*, using the head coil for signal reception, about 24h after irradiation.

All phantoms were placed in the center of the head coil, as seen in *Figure 8.8*, and were measured one day (1d), one week (7d), two weeks (15d) and one month (30d) after irradiation. Coronal sections of the phantoms were obtained, in which the smallest anatomical axis was considered to be the phase coding axis. The gel containers were stored in the MR scanner room for at least 2h before measurements to reduce temperature variation with impact on T2. The reference (non-irradiated) polymer gels ($D = 0$ *Gy*) were treated in the same way as the irradiated ones (from manufacturing—including storage in the radiation room— till measurement).

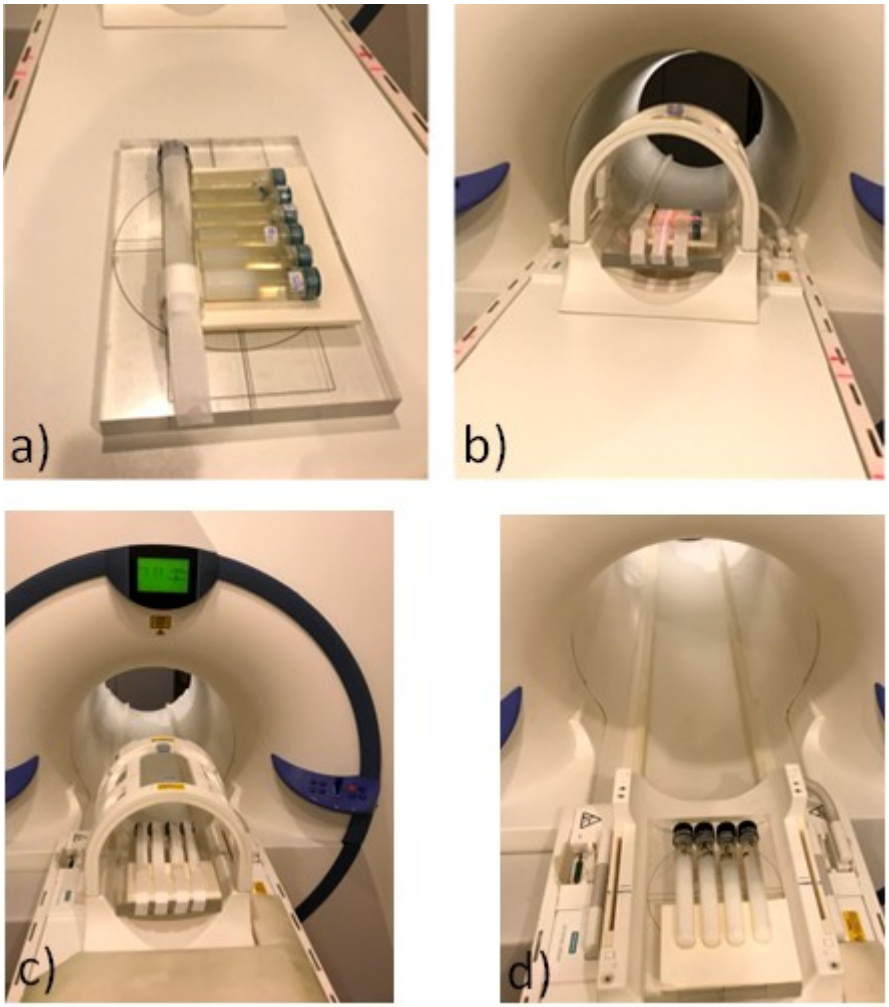

Figure 8.8 MR Imaging of the phantoms using the Head Coil of Batch A (a, b) and Batch B (c, d).

The scanning time, for the applied MR sequences performed, was 40 min. The main sequences were *Multiple Echo Spin Echo (MESE)* and *Half Fourier Acquisition Single shot TSE (HASTE),* as parameter selective T2 imaging was performed at the same time.

The *MESE* sequence included *32 echoes* with echo time spacing *TE = 35 ms – 1120ms*, allowed for differently T2-weighted imaging (repetition time *TR = 2000 ms*, field of view (FOV) = 17.5 x 35 mm^2, matrix size = 256 × 128, slice thickness = 2mm, number of slices = 8, flip angle (FA) = 180°). Before image processing the first echo was removed.

As for the *HASTE* sequence, with 4 echoes (all included), the echo spacing time is *TE = TE1/TE16/TE31/TE46/ = 36 ms/436 ms/835ms/1250 ms,* allowed for differently T2-weighted imaging (repetition time *TR = 2000 ms*, field of view (FOV) = 17.5 x 35 mm^2, matrix size = 256 × 128, slice thickness = 2mm, number of slices = 15, flip angle (FA) = 180°).

For quantitative T2-evaluation, the images generated from the MRI system were transferred to a *PACS workstation* (*EvoRad*, Athens, Greece) for post-processing. *Regions of interest (ROI)* of specific dimensions (52 pixels – 0.97 cm^2) were then selected in the reconstructed *T2* tables, to estimate the *mean T2* values and their respective standard errors for each region (*Figure 8.9*).

Regions of interest were placed in every differently irradiated area of all seven phantoms of each batch.

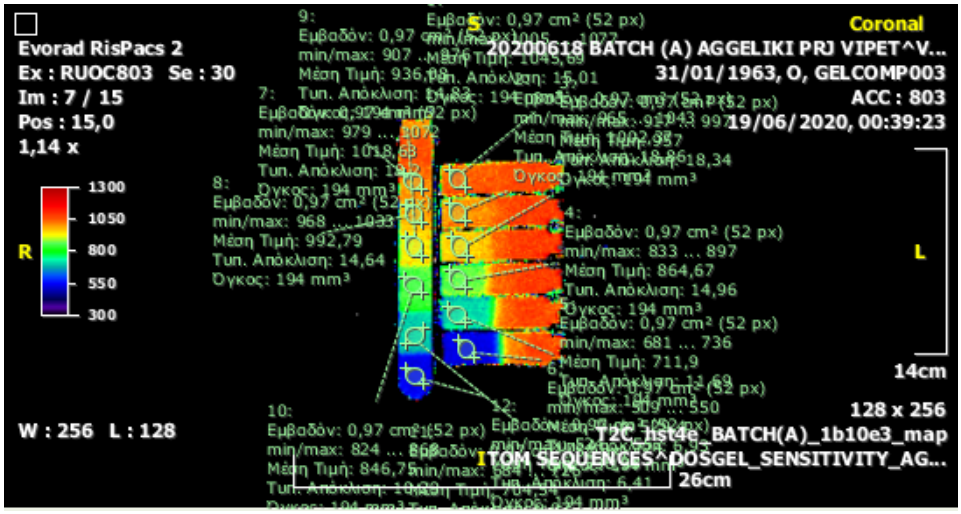

Figure 8.9 MRI processing data- Region Of Interest of each phantom, in different dose areas.

References

1. Maryanski, M. J., Gore, J. C., Kennan, R. P., & Schulz, R. J. (1993). NMR relaxation enhancement in gels polymerized and cross-linked by ionizing radiation: a new approach to 3D dosimetry by MRI. *Magnetic resonance imaging*, *11*(2), 253–258. https://doi.org/10.1016/0730-725x(93)90030-hBaldock et al 1998
2. Hepworth, S. J., Leach, M. O., & Doran, S. J. (1999). Dynamics of polymerization in polyacrylamide gel (PAG) dosimeters: (II) modeling oxygen diffusion. *Physics in medicine and biology,* 44(8), 1875–1884. https://doi.org/10.1088/0031-9155/44/8/302
3. *Pap*adakis, A. E., Maris, T. G., Zacharopoulou, F., Pappas, E., Zacharakis, G., & Damilakis, J. (2007). An evaluation of the dosimetric performance characteristics of N-vinylpyrrolidone-based polymer gels. Physics in medicine and biology, 52(16), 5069–5083. https://doi.org/10.1088/0031-9155/52/16/024
4. Pappas, E., Maris, T., Angelopoulos, A., Paparigopoulou, M., Sakelliou, L., Sandilos, P., Voyiatzi, S., & Vlachos, L. (1999). A new polymer gel for magnetic resonance imaging (MRI) radiation dosimetry. Physics in medicine and biology, 44(10), 2677–2684. https://doi.org/10.1088/0031-9155/44/10/320

9. Results

9.1 Polymer gel calibration

The irradiation of gel containing low oxygen scavenger concentrations, *VIPASCU(1),* yielded an R2 value of 1.9/s in the high dose region at 32 Gy, reflecting high sensitivity. Increasing the oxygen scavenger concentrations resulted in lower MRI relaxation rates at 32 Gy (R2_VIPASCU(2) = 1.5/s and R2_VIPASCU(3) = 1.2/s) (*Figure 9.1*).

9.2 Impact of oxygen scavenger concentration on dose-rate and dose-sensitivity effect

Batch A

For *Batch A* the dose range administered varied from 0 to 32 Gy. The results of Batch A on dose response are shown in *Figures 9.1(a)–(d)* (as previously mentioned, only *big* vials will be taken into account). Calculated dose sensitivities (evaluated as slope α = ΔR2/ΔD) obtained for the different dose rates are summarized in Table 2. Also, absolute values and sensitivities α, normalized to the sensitivity of the lowest dose rate of the specific polymer gel, are indicated including corresponding errors, evaluated from the linear fitting routine.

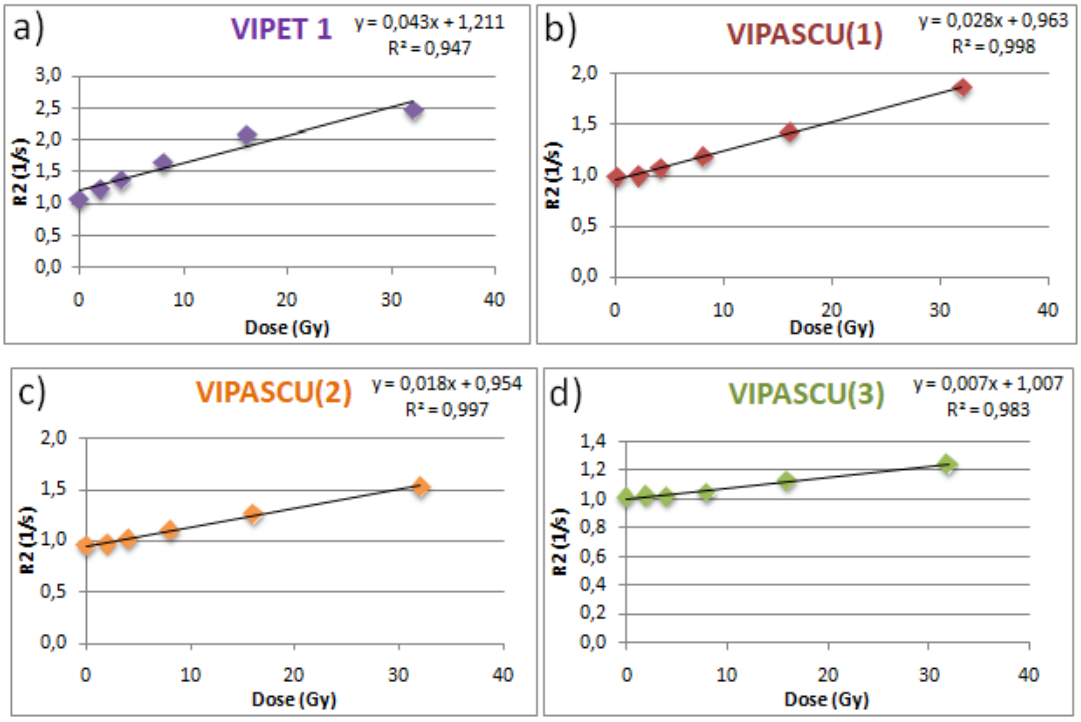

Figure 9.1 Dose response curves of the six different irradiated areas of VIPET and VIPASCU gel of Batch A. (a) VIPET gel, dose response R2 to different dose ranges, up to $Dmax = 32\ Gy$ (b) Batch A, dose response R2 to different dose rates ranging up to $Dmax = 32\ Gy$ for VIPASCU(1) gel (lowest concentration

of oxygen scavenger). (c) Batch A, VIPASCU(2) dose response for different dose ranges. (d) Batch A, dose response for VIPASCU(3) with the highest concentration of ascorbic acid.

The effects of R2 relaxation enhancement by any combination of the different chemicals that are used in the VIPASCU gel formulation were investigated. R2 values ($R2 = 1 / T2$) were used for the assessment of Dose Resolution (D_{Δ}^{P}). The dose calibration curve was adjusted linearly according to the linear equation: $R2\ (D)=\alpha D+R2_0$. Sensitivity (α) and initial value R2 ($R2_0$) were determined by the slope and the point of intersection with the y axis of the calibration curve respectively.

VIPASCU gels (1), (2) and (3), using Ascorbic acid and copper sulfate as an oxygen scavenger, have a more linear behavior than the VIPET gel, using THCP (Tetrakis). Comparing to the results, it was assumed that *VIPASCU (1)* (with *0.2 mM Ascorbic Acid concentration*) had the best results concerning dose sensitivity and dose resolution. So, after this first attempt (Batch A), by comparing the new polymer *VIPASCU* gels to the *VIPET* gel, the results showed prospects for improvement.

Batch B

Considering the differences in dose sensitivity in the low and high dose range region for *VIPET(1)* gel compared to *VIPASCU (1), (2) and (3)*, the experimental set-up for *Batch B* was slightly changed:

- The dose range was varied from *0 to 64 Gy*, since it was observed that VIPASCU gel has a greater dynamic range than VIPET gel.
- The concentration of Ascorbic Acid varied from 0.*1 mM to 0.3 mM*, by reducing the concentration of *Copper(II) sulfate pentahydrate* down to *0.00016 mM*.

The graphs presented in *Figure 8.2* below, represent the *relaxation rate R2* versus the d*ose calibration* data of the four phantoms of *Batch B* of *VIPASCU* gel and *VIPET(2)* batch of *VIPET* gel, up to $Dmax = 32\ Gy$. The graphs presented in *Figure 9.2,* represent the *relaxation rate R2* versus the d*ose calibration* data of the four phantoms of *Batch B* and *VIPET(2)* batch up to $Dmax = 64\ Gy$.

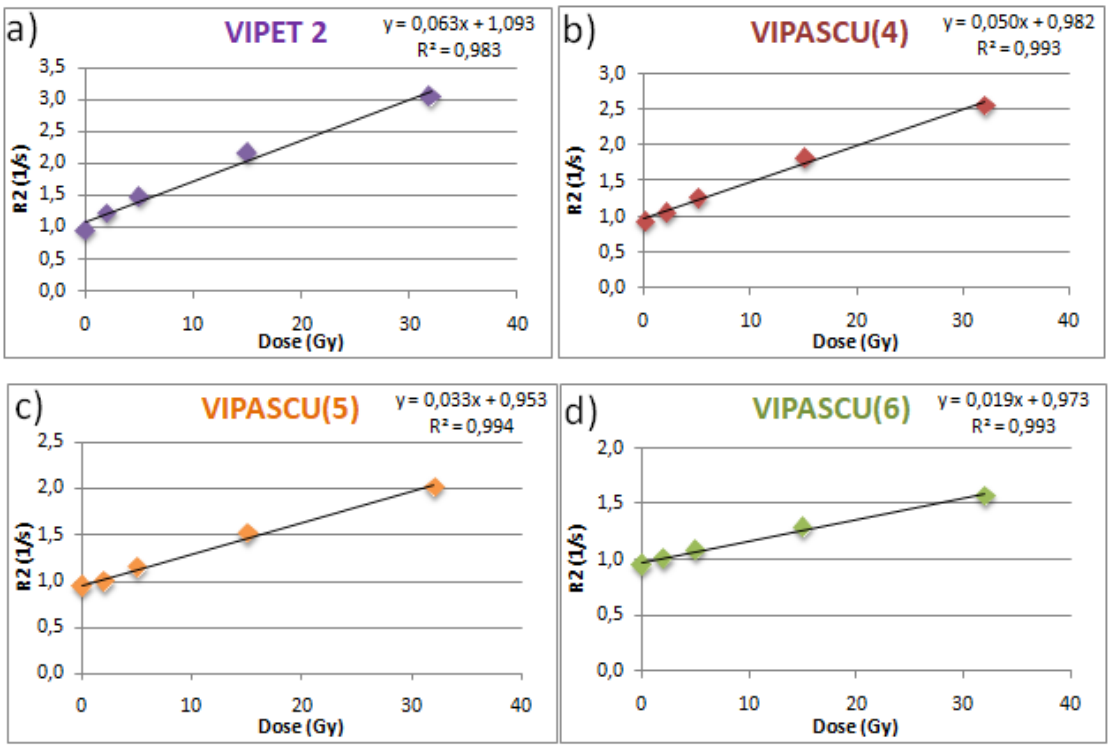

Figure 9.2 Dose response curves of the six different irradiated areas of VIPET and VIPASCU gel of Batch B. (a) VIPET(2) gel batch, dose response R2 to different dose ranges, up to $Dmax = 32\,Gy$ (b) Batch B, dose response R2 to different dose rates ranging up to $Dmax = 32\,Gy$ for VIPASCU(4) gel (lowest concentration of oxygen scavenger). (c) Batch B, dose response for VIPASCU(5) gel for different dose ranges. (d) Batch B, dose response for VIPASCU(6) with the highest concentration of ascorbic acid.

From the graphs, it was assumed that the *VIPASCU* gel compositions (4), (5) and (6), using Ascorbic acid and Copper Sulfate as an oxygen scavenger, have a more linear behavior than the *VIPET* gel composition, using THCP (Tetrakis). In addition, the lower concentration of *Copper (II) sulfate pentahydrate* used in the *VIPASCU* gels of *Batch B,* as compared to the *VIPASCU* gels of *Batch A* where a higher concentration was used, doesn't seem to affect the dose response or the gel's sensitivity.

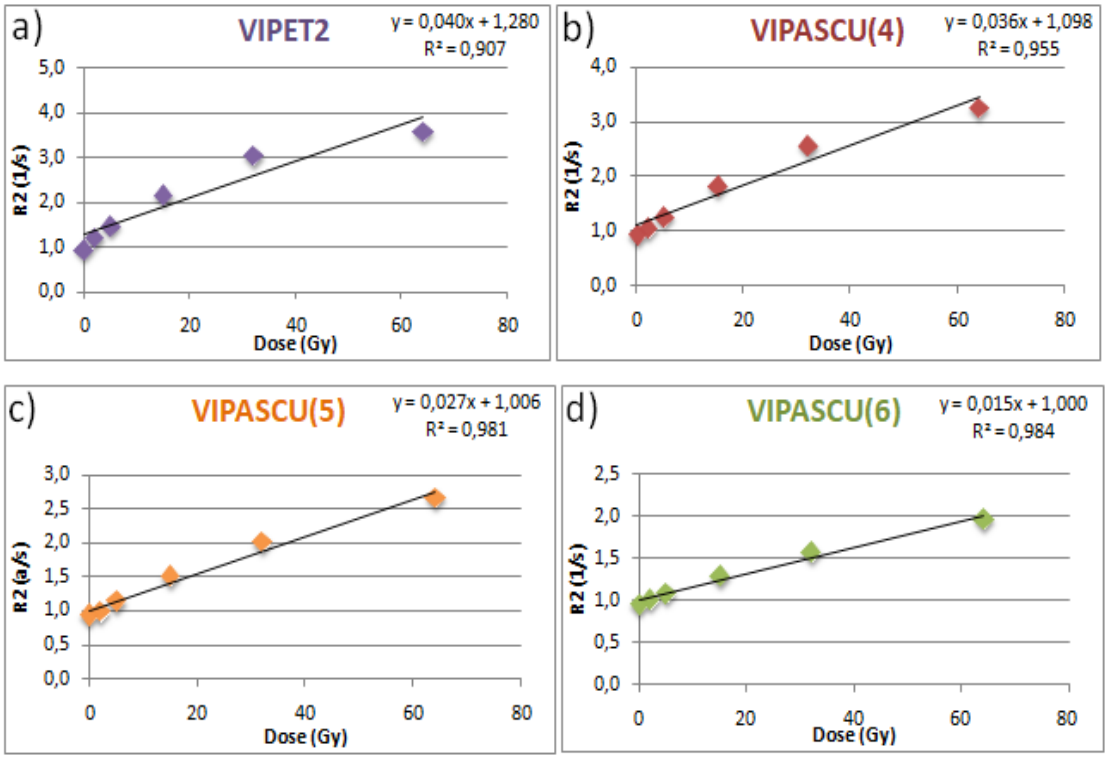

Figure 9.3 Dose response curves of the six different irradiated areas of VIPET and VIPASCU gel of Batch B. (a) VIPET gel, dose response R2 to different dose ranges, up to $Dmax = 64\,Gy$ (b) Batch B, dose response R2 to different dose rates ranging up to $Dmax = 64\,Gy$ for VIPASCU(4) gel (lowest concentration of oxygen scavenger). (c) Batch B, VIPASCU(5) dose response for different dose ranges. (d) Batch B, dose response for VIPASCU(6) with the highest concentration of ascorbic acid.

The graphs presented in *Figure 9.3,* represent the *relaxation rate R2* versus the d*ose calibration* data of the four phantoms up to 64 Gy. It is known that the maximum dose for the clinical part of radiotherapy is up to 32 Gy, but at this point it is emphasized that *VIPASCU* gel can be used clinically and in higher doses with the necessary improvements.

Batch C

Considering the differences in dose sensitivity in the low and high dose range region for *VIPET* gel compared to *VIPASCU (4), (5) and (6)*, the experimental set-up for *Batch C* was slightly changed, in order to investigate how the concentration of *Copper(II) sulfate pentahydrate* influences the dose response and the dose sensitivity.

So the concentration of Ascorbic Acid was stable at *0.2mM*, while the concentration of *Copper (II) sulfate pentahydrate* was varied from *0mM (absence of the monomer) to 5 mM*. The dose range was varied from *0 to 64 Gy*, since it was observed that *VIPASCU* gel has a greater dynamic range than VIPET gel.

As it is shown in *Figure 9.4*, from left to right, only the first vial, VIPASCU (7) (with $C_{copper} = 0\ mM$) has an escalation in dose range, while the others don't, since polymerization didn't occur during irradiation due to the high concentration of *Copper(II) sulfate pentahydrate*. There is no point in doing a further analysis for VIPASCU (8), VIPASCU (9) and VIPASCU (10), since they didn't polymerize.

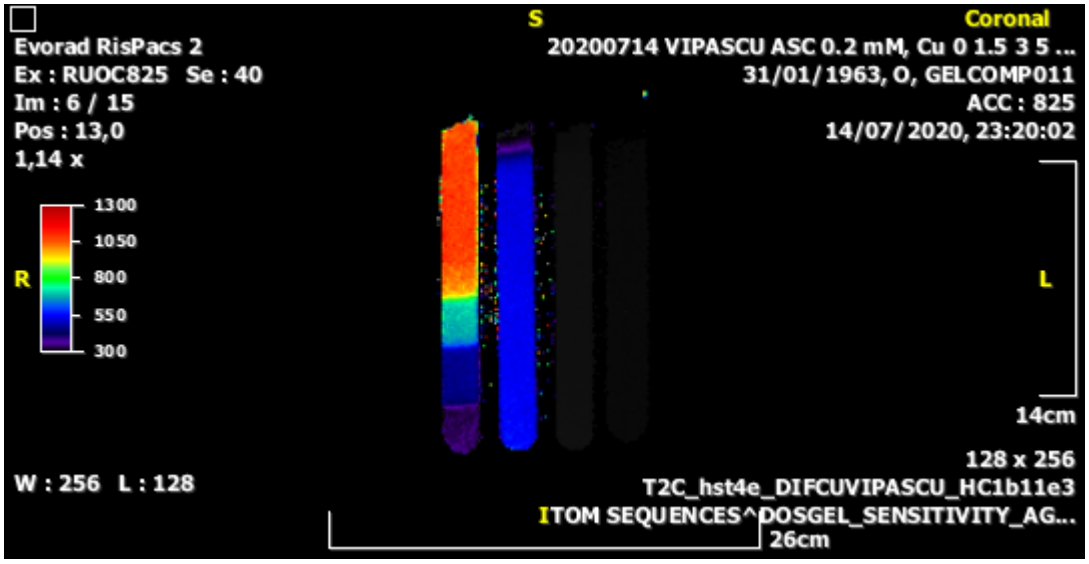

Figure 9.4 MRI processing data- Selecting a Region Of Interest of Batch C, in different dose range areas.

The graph presented in *Figure 9.5* below, represents the *relaxation rate R2* versus the d*ose calibration* data of *VIPASCU (7)* gel. From the graph it is assumed that the *VIPASCU (7)* gel has a more linear behavior after the administration of *10 Gy.* Consequently, this polymer gel dosimeter isn't able to measure ionizing radiation in lower doses *(under 10 Gy)*, since it can't be absorbed.

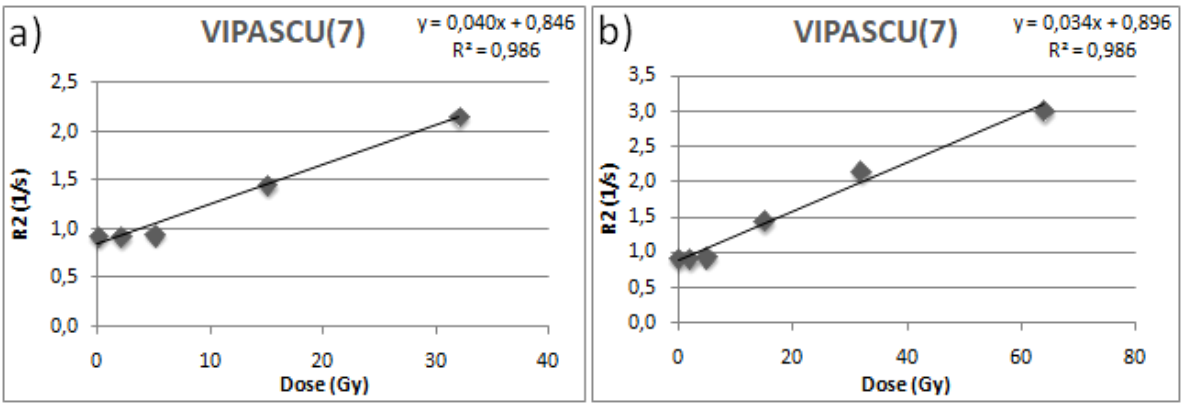

Figure 9.5 Dose response curves of the six different irradiated areas of VIPASCU (7) gel of Batch C. (a) Batch B, dose response R2 to different dose ranges, up to $Dmax = 32\ Gy$ for VIPASCU(7) gel (0mM concentration of *Copper(II) sulfate pentahydrate*). (b) Batch B, dose response R2 to different dose ranges, up to $Dmax = 64\ Gy$ for VIPASCU(7) gel (0mM concentration of *Copper(II) sulfate pentahydrate*).

A comparison between the VIPASCU (1), VIPASCU (5) and VIPASCU(7) gels was made, as seen in *Figure 9.6*. The gels referred, have the same concentration of *Ascorbic Acid* ($C_{aa} = 0.2\ mM$) and different concentrations of *Copper (II) sulfate pentahydrate* ($C_{copper} = 0.01\ mM$, $C_{copper} = 0.00016\ mM$ and $C_{copper} = 0\ mM$ respectively).

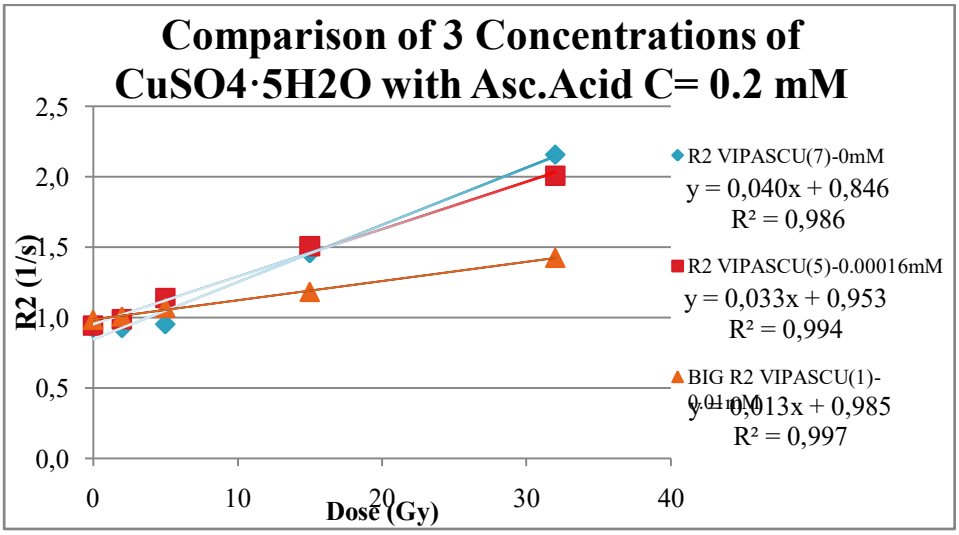

Figure 9.6 Dose response comparison between the VIPASCU(1), VIPASCU(5) and VIPASCU(7) gels.

From the comparison above (*Figure 9.6*), it is clear that the presence of *Copper (II) sulfate pentahydrate* is necessary, especially for low dose ranges below 10 Gy. In other words, VIPASCU (7) gel can be excluded. Furthermore, by comparing the *VIPASCU (1)* and *(5)* gels, it is clear that these *VIPASCU* gel compositions are the closest to the *VIPET's* gel dosimetric characteristics, concerning their dose response and their dose sensitivity. The *VIPASCU* gels have a steeper slope (lower sensitivity), but are more linear than *VIPET* gel and they appear to have a larger dynamic range. Although, *VIPASCU (5)* is the best chemistry composition, since it has a higher sensitivity than *VIPASCU(1)* gel and it's comparable to the *VIPET* gel.

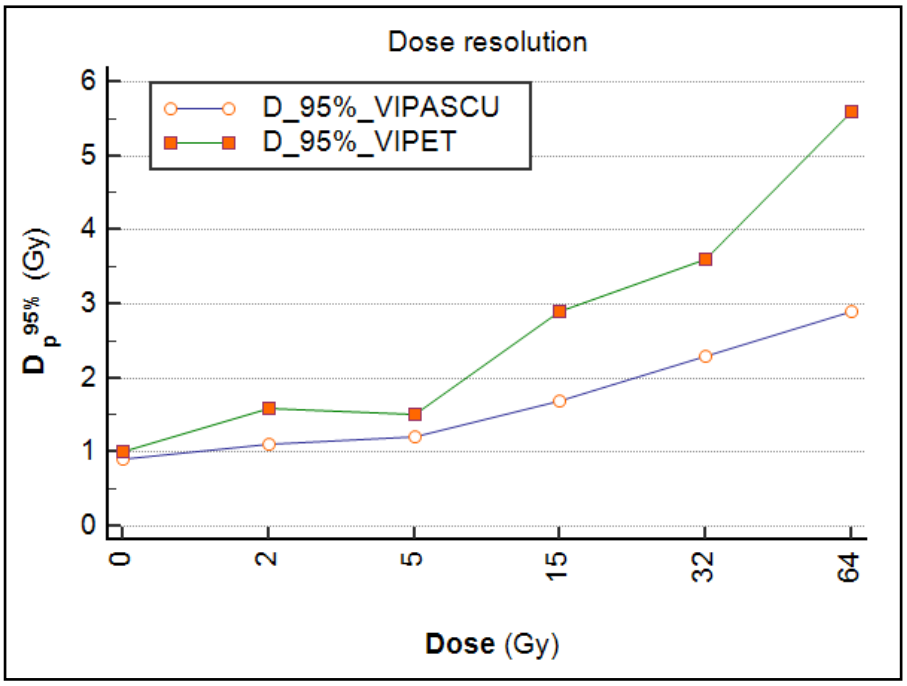

Figure 9.7 Dose resolution comparison of VIPET and VIPASCU polymer gel dosimeters evaluated at 24 hours, post-irradiation.

It is well known that the performance of a polymer gel dosimeter cannot be assessed based on the R2-dose sensitivity alone (*Baldock et al 1999a, 1999b, 2001, Lepage et al 2001a, De Deene 2004a, 2004b*). Numerous parameters need to be considered such as spatial and temporal stability, edge response and dose resolution, which requires the properties of the dosimeter to be coupled with the ability of the measurement technique to provide low uncertainties (*Baldock et al 2001, Lepage et al 2001a*).

In *Figure 9.7*, $D_p^{95\%}$ has been plotted as a function of absorbed dose for the different doses that were delivered to the gels. The use of $D_p^{95\%}$ has significance when making comparison between gel dosimetry dose maps and radiotherapy treatment plans and, further, with the introduction of alternative gel formulations to those currently published (*Baldock et al 2001*). The concepts outlined in this communication are applicable to different methodologies for evaluating polymer gel dosimeters such as optical techniques including optical density scanning (*Gore et al 1996*) and X-ray computed tomography (*Hilts et al 2000*). It is assumed in clinical radiotherapy that the dose delivered to the patient should be within 5% of the prescribed value (*Brahme 1984*). As one contributing factor to the delivery of the dose, it is necessary for the dosimetry to have an uncertainty significantly less than 5%.

So, from the total delivered dose (64 Gy), *VIPASCU* gel has a better (lower) dose resolution than *VIPET* gel, since it has a dose difference equal to ± *3 Gy*. On the other hand, the VIPET gel has a higher dose resolution, resulting to a bigger dose difference equal to ± *6 Gy*.

9.3 Comparison of the MR Imaging sequences

Two pulse sequences, *MESE* and *HASTE*, were used as reading methods to evaluate the dosimetric characteristics of *VIPET* and *VIPASCU* gels. The *MESE* technique is the given technique used to read dosimeters, while *HASTE* is a new sequence that reduces the scan time from *45min to 15min*.

As mentioned, R2 values remain lower with the *HASTE* sequence compared to *MESE*. This underestimation of the R2 values or the overestimation of the T2 values is due to the existence of the 180^0pulses that exist in the fast sequence. This phenomenon is more pronounced at high doses, where R2 values are high. Furthermore, with the rapid sequence, a degradation in resolution was observed for the whole dose range.

A big difference between the two techniques is the number of *TE intervals* used as well as the values of the TE intervals. In the usual sequence, *32 TEs* were used and the *first measurement* was removed in the reconstructed table, due to the imbalance. In contrast to the rapid *HASTE* technique *4 TEeffs* were used and the first measurement was not subtracted. Thus receiving less signals leads to an underestimation of the measurements, for this reason the resolution is reduced.

In general, HASTE sequences are faster than standard MESE sequences, due to the high *ETL index* they are designed to have. In these sequences, the benefit in scanning time is enhanced by the existence of a *pre-pulse (or restoring pulse)* used before the 180^0pulses, which further reduces the TR time. Therefore, the overall reduction in scanning time achieved with these fast sequences, provides a great advantage for reading gel dosimeters in clinical practice. Also the ability to take 25 minute sections (2mm thick) without a gap between them (gap = 0) within 15 min, gives the user the ability to produce *3D images* of large scan volumes in a tolerable time.

In the following figure, *Figure 9.9, the Polynomial* regression graphs between *MESE* and *HASTE* sequences for the *VIPET(2)* batch and *VIPASCU (5)* batches are presented.

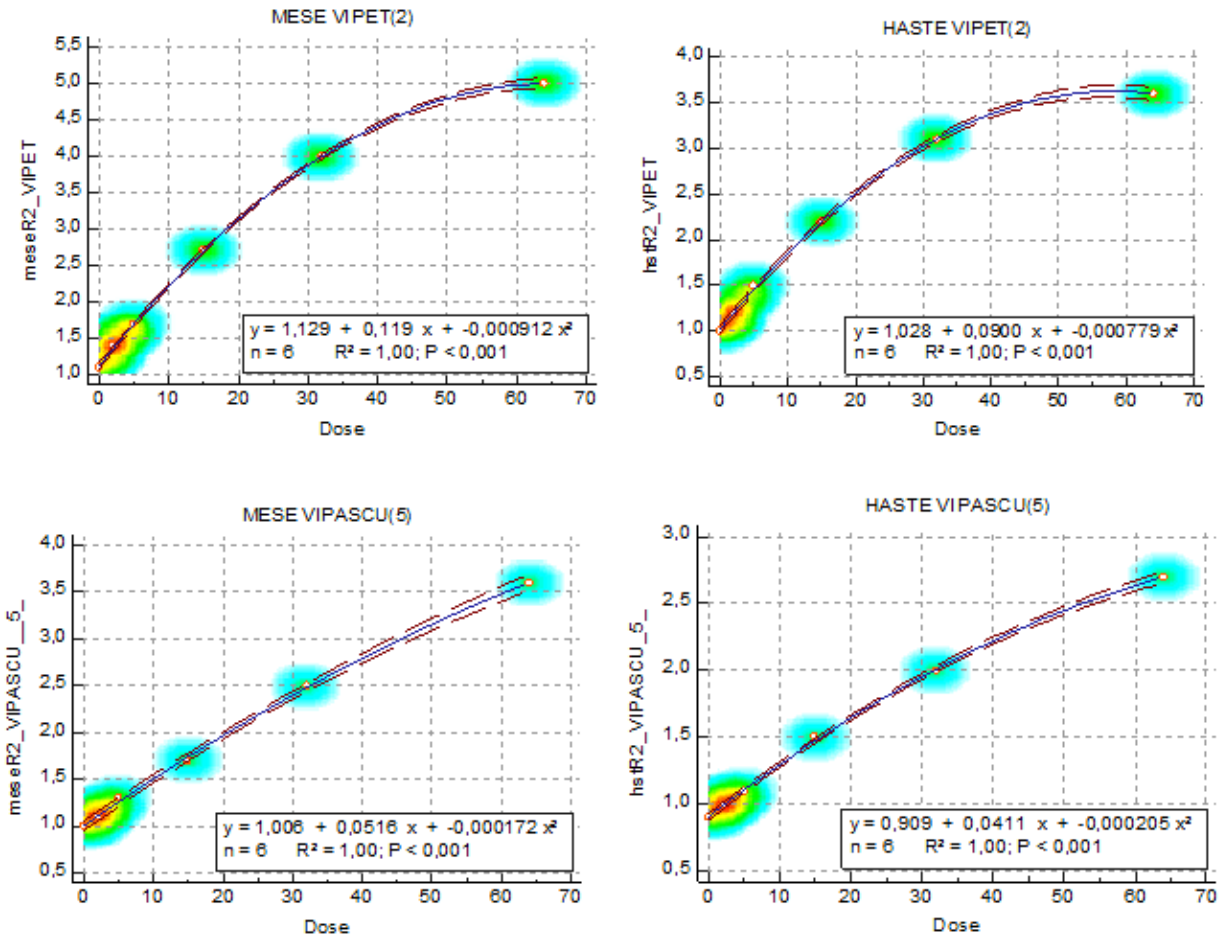

Figure 9.9 Polynomial regression graphs between MESE and HASTE sequences of the VIPET(2) batch and VIPASCU (5) gel of Batch B.

By comparing the graphs in *Figure 9.9, it seems that the VIPET(2)* gel has a higher dose sensitivity, but the nonlinear term has a large effect on the curve, since in the larger dose range (above 32 Gy) it has become flat. In addition, *VIPASCU(5)* gel has a lower dose sensitivity, but it is clear that the non-linear term has a small effect on the curve. Consequently, it has a larger dynamic dose range and it can actually be irradiated in a higher dose range, above 64 Gy. Moreover, it can be assumed that HASTE technique is definitely a better choice, as it has a better behavior and more advantages than MESE technique.

The potential benefits of ultrafast sequences have stimulated research in the development of MR sequences that reduce acquisition time without sacrificing image quality. A half-Fourier acquisition single-shot turbo spin-echo (HASTE) sequence can provide all image information after a single excitation pulse. Because of its very short acquisition times, the sequence isn't appreciably affected by patients' movement or respiratory artifacts. So, the HASTE sequences afford substantial time reduction and also decrease motion artifacts and thus have potential advantages. Its T2 weighting allows impressive imaging of fluid and obstructed systems.

10. Conclusions

In this work a new polymer gel dosimeter called *VIPASCU* was presented, which is less toxic, cost effective than the known *VIPET* gel and has high dose sensitivity. After data and statistical analysis, the quality of the dosimetric results of the radiotherapy experiments that took place was ensured. Moreover, two MR Imaging sequences of the polymer gel dosimeters manufactured were presented, along with the data for the post-processing of the initial measurements and for the optimization of the results.

From this study, we came to the following conclusions:

1. A new polymer gel dosimeter, VIPASCU, was introduced and compared to the VIPET gel dosimeter. The role of the different constituent chemicals was investigated, as well as the response of the gel upon irradiation.

2. It is shown that other chemicals may also be used to scavenge oxygen with different reaction rates for the various anti-oxidants observed. The VIPASCU gel dosimeter consisted of the same monomers as the VIPET gel, except from its oxygen scavenger, by using Ascorbic Acid and Copper (II) sulfate pentahydrate as its cosolvent instead of "Tetrakis" (THPC) that is used in VIPET gel. In contrast with the VIPET gel (using THPC to scavenge oxygen), this oxygen scavenger option makes the VIPASCU gel a *less-toxic* gel composition, which is *affordable* and *easy* to manufacture.

3. The proposed polymer gel dosimeter *VIPASCU* can be used to estimate doses from 0.5Gy up to 64 Gy, with a much greater linearity that the *VIPET* gel dosimeter, thus a greater dynamic range.

4. This system shows a linear response in the *2-35 Gy* dose range and in this range can be used to produce relative dosimetry measurements without the calibration process.

5. *Sensitivity* and *uncertainty* are significantly degraded when the solution is irradiated for more than one week after manufacture.

6. Although VIPASCU gel has a greater dynamic range than VIPET gel, it has a lower dose sensitivity compared to VIPET.

7. The time interval between irradiation – MR Imaging, proved to not affect the dosimetric characteristics. The system can be read reliably using MRI even 3 weeks after irradiation.

8. The *VIPASCU* gel, with absence of *Copper (II) sulfate pentahydrate* in its composition shows a linear response in the 10-35Gy dose range, but doesn't show a linear response in lower doses (below 10 Gy).

9. The *VIPASCU* gel has a lower dose resolution than *VIPET* gel in a 95% confidence level.

10. The use of a new and fast sequence, *HASTE*, for reading gel dosimeters enables the creation of three-dimensional maps in a very *short* time, compared to the usual sequence, *MESE*.

11. At the suggested intervals between preparation - irradiation and irradiation - reading, the *VIPASCU* gel presented reliable and important results. Thus, the proposed dosimetric system can play an important role in assessing and confirming dose distributions of treatment plans of modern radiotherapy techniques.

11. Discussion

Radiation therapy is a treatment that relies on the use of ionizing radiation. Its purpose is to give as much dose as possible to the target tumor and at the same time to maximize the protection of healthy tissues. Modern radiotherapy techniques (*conformal / stereotactic*) presuppose the existence of specialized dosimetric methods for the audit of dose distributions in *three physical dimensions* and for *very small physical tumors*. Today, reliable dosimetric techniques that can satisfy the requirements of modern radiotherapy, providing *three-dimensional* dose distributions are the techniques of *polymer gel dosimetry*.

The first polymer gel dosimeters [1,2] were made in normoxic conditions, in a cage of argon or nitrogen. Although the existence of the cage made their production difficult, its use was necessary because the presence of oxygen terminated the polymerization reactions. An important development [3] in the process of preparing these solutions was the addition of an "*oxygen-scavenger*" substance to the solution, which allowed the construction of dosimeters under atmospheric conditions.

The research team of the University of Crete presented in 2007 the first antioxidant dosimeter of polymer gel with *vinylpyrrolidone* (normoxic N-vinylpyrrolidone based polymer gel), VIPET. The oxygen-scavenger substance used was "*Tetrakis*" (TetrakisHydroxymethylPhosphonium Chloride THPC) and the new dosimeter was prepared under atmospheric conditions. In this study an introductory study of the dosimetric characteristics of this solution was presented [4].

Today, the continuous development of radiotherapy techniques requires the existence of reliable dosimeters that provide three-dimensional (3D) confirmation of dose distributions. In the last twenty years, different polymer gel dosimeters have been introduced. Each of them is characterized by specific dosimetric characteristics. Recently, efforts have been made to optimize their dosimetric characteristics (sensitivity, optical dose response): (a) either by adding co-solvents to the solution [5, 6], (b) or by increasing the concentration of the monomer molecules in the solution [7].

In recent years, studies have been conducted to accurately identify the sources of uncertainty throughout the process of polymer gel dosimetry [8-11]. According to these researches, sources of errors during *(a) preparation*, *(b) storage*, *(c) radiation* and *(d) reading*, degrade the dosimetric characteristics and reliability of these dosimeters. In 2006 [8], the importance of storage conditions before irradiation and before reading was emphasized, so that the dosimeter presents a uniform temperature distribution throughout its extent.

According to a 2011 study [10], the accuracy and repeatability of the dosimetric characteristics of these dosimeters are affected by possible sources of oxygen contamination when manufactured under atmospheric conditions. A possible oxygen contamination during preparation, filling, storage or irradiation can either lead to overestimation or underestimation of the dose response.

Different gel dosimeters of various compositions and ingredients have been studied (*Baldock et al 1998, Fong et al 2001, Senden et al 2006, Baldock 2009)*. The polymerization due to irradiation is very sensitive to oxygen exposure in the gel (*De Deene et al 2001, 2002, 2006, Fong et al 2001, Bayreder et al 2006, Senden et al 2006*). Oxygen scavenging is therefore considered to be one of the most important developments in polymer gel dosimetry due to the possibility to have the gels manufactured in a minimally-equipped laboratory at atmospheric conditions. Various studies are

available on different compositions and formulations of normoxic polymer gel dosimeters (*De Deene et al 2006, Senden et al 2006, Luci et al 2007, Baldock 2009*).

The Magnetic Resonance measurement parameter R2 = 1/T2 is sensitive to the polymerization level dependent on the initial radical production by ionizing radiation and allows for 3D-dose imaging after performing a calibration procedure. (Maryanski et al 1994, Courbon et al 2006). In many different gel compositions, the calibration curve exhibits a rather linear dose response relationship at least in the low dose range (Maryanski et al 1993, Baldock 2009, Crescenti et al 2009, Sedaghat et al 2009).Methacrylic acid-based polymer gels have been proposed for their high sensitivity and less toxicity, but it has been reported that there is a strong dose-rate dependence of the dose response (Bayreder et al 2006, De Deene et al 2006, Karlsson et al 2007).

In this study the dosimetric characteristics of two types of antioxidant polymer gel dosimeters with *vinylpyrrolidone* as the basic monomer, *VIPET* and *VIPASCU* (a new polymer gel) were evaluated and compared. *VIPET* gel was used as a comparison measure, since its chemical structure and dosimetric characteristics are familiar, from other studies, as mentioned previously. The two gels consist of the same monomers. The only difference in their composition is that *VIPASCU* gel is made with a different *oxygen-scavenger* substance, seeking to extend the dose response of the original *VIPET* formulation in the low dose region, as well as its sensitivity as a gel phantom. The influence of the oxygen scavenger concentrations was clear, when reflecting to a different dose range area, although there were limitations in the measurements taken, since the gels were only irradiated in six different doses (limited sample).

Another limitation is that no comparison was made with an actual dose measurement. For instance, an ion chamber could be used for the proper detection and measurement of the delivered dose in the polymer gel dosimeters. In a future work, a phantom that responds to an actual patient (personalized phantom) could be used to make a dose verification.

However, the proposed polymer gel dosimeter *VIPASCU* can be used to estimate doses from 0.5Gy up to 64 Gy, with a much greater linearity that the *VIPET* gel dosimeter. Furthermore, it is a non-toxic composition, which is easy to manufacture. It was observed that the *VIPASCU* gel, with absence of *Copper (II) sulfate pentahydrate* in its composition shows a linear response in the 10-35Gy dose range, but doesn't have a linear response in lower doses. Furthermore, *VIPASCU* gel has a lower (better) dose resolution than *VIPET* gel. Furthermore, the concentration of *Copper (II) sulfate pentahydrate* could be further examined, in order to improve VIPASCU gel's dose sensitivity in the dose range of 0 to 32 Gy.

The outcomes of the radiotherapy experiments that took place were optimized with the support of Magnetic Resonance Imaging Techniques in phantoms and with the use of two main sequences (MESE and HASTE). The new and fast sequence, *HASTE*, was used for reading gel dosimeters and the creation of three-dimensional maps in a very short time was enabled.

The results of this study, can be used to improve quantitative dosimetric characteristics in polymer gel dosimetry based on *VIPAR-type* polymer gels and also offer recommendations for polymer gels with similar dose rate dependence, while being less toxic and more sensitive to dose. The comparison of *VIPET* and *VIPASCU* gels at the suggested intervals between preparation - irradiation and irradiation – reading time, presented reliable and important results. Thus, the proposed dosimetric system can play an important role in assessing and confirming dose distributions of treatment plans of modern radiotherapy techniques.

References

1. Maryanski, M. J., Gore, J. C., Kennan, R. P., & Schulz, R. J. (1993). NMR relaxation enhancement in gels polymerized and cross-linked by ionizing radiation: a new approach to 3D dosimetry by MRI. *Magnetic resonance imaging*, *11*(2), 253–258. https://doi.org/10.1016/0730-725x(93)90030-h
2. Pappas, E., Maris, T., Angelopoulos, A., Paparigopoulou, M., Sakelliou, L., Sandilos, P., Voyiatzi, S., & Vlachos, L. (1999). A new polymer gel for magnetic resonance imaging (MRI) radiation dosimetry. Physics in medicine and biology, 44(10), 2677–2684. https://doi.org/10.1088/0031-9155/44/10/320
3. Fong, P. M., Keil, D. C., Does, M. D., & Gore, J. C. (2001). Polymer gels for magnetic resonance imaging of radiation dose distributions at normal room atmosphere. Physics in medicine and biology, 46(12), 3105–3113. https://doi.org/10.1088/0031-9155/46/12/303
4. Papadakis, A. E., Maris, T. G., Zacharopoulou, F., Pappas, E., Zacharakis, G., & Damilakis, J. (2007). An evaluation of the dosimetric performance characteristics of N-vinylpyrrolidone-based polymer gels. Physics in medicine and biology, 52(16), 5069–5083. https://doi.org/10.1088/0031-9155/52/16/0245)
5. Koeva, V.I., Csaszar, E.S., Senden, R.J., McAuley, K.B. and Schreiner, L.J. (2008), Polymer Gel Dosimeters with Increased Solubility: A Preliminary Investigation of the NMR and Optical Dose-Response Using Different Crosslinkers and Co-Solvents. Macromol. Symp., 261: 157-166. doi:10.1002/masy.2008501216)
6. Jirasek, A., Hilts, M., Berman, A., & McAuley, K. B. (2009). Effects of glycerol co-solvent on the rate and form of polymer gel dose response. Physics in medicine and biology, 54(4), 907–918. https://doi.org/10.1088/0031-9155/54/4/0067
7. Chain, J. N., Jirasek, A., Schreiner, L. J., & McAuley, K. B. (2011). Cosolvent-free polymer gel dosimeters with improved dose sensitivity and resolution for x-ray CT dose response. Physics in medicine and biology, 56(7), 2091–2102. https://doi.org/10.1088/0031-9155/56/7/012
8. De Deene, Y., Vergote, K., Claeys, C., & De Wagter, C. (2006). The fundamental radiation properties of normoxic polymer gel dosimeters: a comparison between a methacrylic acid based gel and acrylamide based gels. Physics in medicine and biology, 51(3), 653–673. https://doi.org/10.1088/0031-9155/51/3/012)
9. De Deene, Y., Pittomvils, G., & Visalatchi, S. (2007). The influence of cooling rate on the accuracy of normoxic polymer gel dosimeters. Physics in medicine and biology, 52(10), 2719–2728. https://doi.org/10.1088/0031-9155/52/10/00610)
10. Sedaghat, M., Bujold, R., & Lepage, M. (2011). Severe dose inaccuracies caused by an oxygen-antioxidant imbalance in normoxic polymer gel dosimeters. Physics in medicine and biology, 56(3), 601–625. https://doi.org/10.1088/0031-9155/56/3/00611)
11. Sedaghat, M., Bujold, R., & Lepage, M. (2011). Investigating potential physicochemical errors in polymer gel dosimeters. Physics in medicine and biology, 56(18), 6083–6107. https://doi.org/10.1088/0031-9155/56/18/019